Growth and characterisation of organic semiconductors at metal surfaces

by

Simon W. Smalley

A THESIS SUBMITTED IN PARTIAL FULFILMENT
OF THE REQUIREMENTS FOR THE DEGREE OF
DOCTOR OF PHILOSOPHY

Jeremiah Horrocks Institute for Mathematics, Physics and Astronomy

University of Central Lancashire

January 2020

Declaration

The work presented in this thesis was carried out at the Jeremiah Horrocks Institute for Mathematics, Physics and Astronomy, University of Central Lancashire.

I declare that while registered as a candidate for the research degree, I have not been a registered candidate or enrolled student for another award of the University or other academic or professional institution. I declare that no material contained in the thesis has been used in any other submission for an academic award. Data and models used in this thesis that are not my own are clearly cited in the text.

Abstract

This thesis is a report of work carried out at the Jeremiah Horrocks Institute at the University of Central Lancashire, the Stephenson Institute For Renewable Energy at the University of Liverpool and the Center for Nanoscale Materials at Argonne National Lab. The focus of study are systems of interest to developing molecular electronics and systems that facilitate the synthesis of graphene patterned with ordered defects. The approach taken to developing the latter is via the deposition of precursor molecules atop symmetry conflicting substrates.

In the first study we present new structural information obtained through low energy electron diffraction (LEED) of the coronene (Cn)/Ag(100) system, identifying a secondary, temperature dependent structure rotated 45° to the primary Cn structure.

The structure and orientation of dibromobianthryl (DBBA) atop Ag(100) is determined through scanning tunnelling microscopy and supported by density functional theory. DBBA is prochiral following adsorption on Ag(100), forming racemic domains with molecular rows aligned with the substrate nearest-neighbour directions. Deposition of DBBA atop the heated Ag(100) surface and seen to form disordered graphene nanoribbons.

Perfluoropentacene (PFP) an n-type semiconductor, is deposited at monolayer and bilayer coverage on Cu(111). Scanning tunnelling microscopy is used to investigate the geometric and electronic structure of the layer. The first layer experiences charge transfer with the Cu(111) surface. The second layer electronic structure

appears to be unperturbed by the substrate as has been previously observed for pentacene (Pn), a p-type semiconductor. PFP has been reported as being structurally similar to Pn in the bulk and as a result is of interest in mixed crystal studies. This structural similarity is seen to be diminished in the case of monolayer and bilayer films atop Cu(111).

Symmetry conflicts arising from FCC single crystals are range limited by the size of their unit cell. To extend this, complex metallic alloys are also considered as a substrate in this work. These provide large unit cell surfaces, imparting order to adsorbed species across nanometre length-scales. In light of refinements to the structural model of $Al_4(Cr,Fe)(100)$ we present the high resolution scanning tunnelling microscopy (STM) data of this surface. Both the STM and accompanying LEED data collected support the new structural model. Crucially this data confirms that the bulk observed symmetry conflicts are manifested at the surface. Using this new information we also identify the terminating planes of the system, vital for understanding molecular adsorption.

Contents

List of Figures

x

xiv

xxiii

Acknowledgements

Preparing this thesis has been a mixture of challenging and incredibly rewarding moments. It's been emotional. I don't think I would have without the help of many friends, family and colleagues over the years.

The supervisory team has been a pleasure to work with, but I owe particular thanks to Joe. You've walked a fine line between friend, therapist and taskmaster at times and your support and advice has been formative.

Thanks for everything mum and dad, I love you guys, obviously. You've always been there when I needed you and I know you've always been proud of me. Hopefully this makes justifying those feelings a little easier.

I was lucky to have found a place in the JHI, they're a good bunch. I'll walk away with friendships and memories I'll always treasure. Also a thesis. A final shout out to everyone else in the maudland basement, those who kept The Variety in business, and those I rolled dice with.

1

Introduction

"One man cannot summon the future,

but one man can change the present."

– Mr Spock, *Star Trek: TOS*

1.1 Introduction and motivation

The main advances in computing power stem from packing more components into a smaller space. One of the greatest achievements in this pursuit was the shift from vacuum tube technology in the late 1940s to the transistor. These devices act as switches in electronic circuitry, when a sufficient gate voltage is applied then current is permitted to flow across them. In the case of vacuum tubes this voltage is required to excite electrons across a vacuum gap and in solid state transistors this is the corresponds to the voltage required to facilitate the transport of electrons or holes across the bandgap. A conventional array of tubes comparable in size to small light bulbs is seen in figure 1.1(a) and a modern pair of transistors approximately 50 nm in size are shown in figure 1.1(b).

The advent of this technological breakthrough reduced the size, inefficiency and
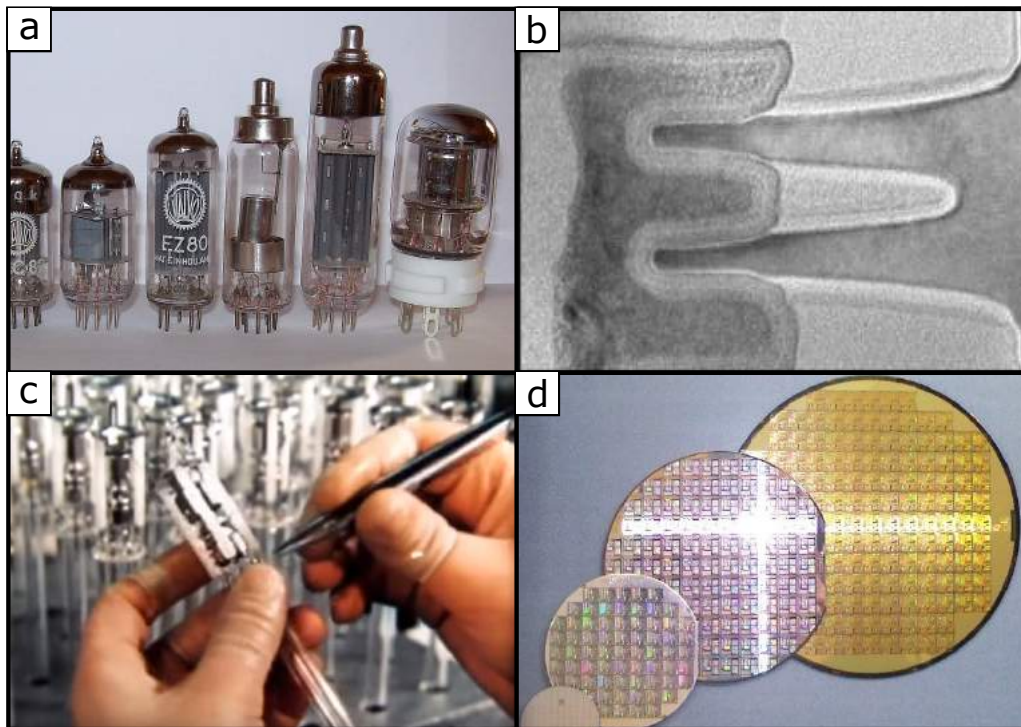
Figure 1.1: a) A collection of vacuum tubes produced in the 20th century. B) SEM image of fins comprising a modern Intel transistor approximately 40 nm apart [1]. c) Vacuum tube assembly on a production line in the 70s d) Si wafer patterned with chips covered in transistors and circuitry. All chip components are manufactured simultaneously via lithographic processes.

power requirements of electronic computers in a short space of years making vacuum tubes in this role obsolete by the late 50's. The transistor turned computers from industrial machines into a commodity modern society relies upon. Transistors have continued to shrink over the years going from palm sized devices to being sub 100 nm^2. These number 2 bn within smart phones alone. Quoting single dimensions can be misleading and so transistor density is typically used an approximation of computing power. In 1965 the observation was made that the number of transistors that could fit in a given area doubles every two years [25] and computing power with it. Known as Moore's law, this has held true for the best part of 50 years, but in the past decade it has been recognised that we have approached the limit of what can be achieved with current technology [26, 27]. The ultimate barrier to reducing component sizes is the quantised nature of matter. Whilst devices are still two orders of magnitude larger than the fundamental building block of the atom (approximately 10 nm and 0.1 nm respectively) this limit prematurely arises in how small devices can be produced *reliably*.

To achieve this not only did new designs and architecture require development, but also scalable methods of mass production to keep pace with the increasing number of devices. A great deal is owed to the development of efficient manufacturing techniques to make computing affordable. The mass production of vacuum tubes occurred on an assembly line as shown in figure 1.1(c). This sequential approach could not scale with doubling output every two years. To achieve this serial production had to give way to parallel systems such as lithography that can create whole circuits simultaneously such as those on the Si wafers pictured in figure 1.1(d).

In the pursuit of miniaturisation a natural development was to attempt the implementation of 2D materials such as graphene in device construction, following its isolation in 2004 [28]. Graphene is a single layer of carbon atoms that is highly conductive and in a pristine state has no bandgap. The two dimensionality of graphene

means that the electronic properties are dependent on its structure and it has been demonstrated that a bandgap can be induced through lattice strain and deformation [29, 30, 31]. This is in contrast to the chemical doping techniques typically used for bandgap engineering in conventional semiconductor designs. In traditional semiconductors such as Si or Ge doping is carried out by the introduction of an impurity atom of a different element. If the impurity is electron rich, having more electrons than the bulk element then it is considered a donor and the resultant semiconductor incorporating it is n-type. If the impurity atoms has fewer electrons it is an acceptor and the resultant semiconductor is p-type. these impurities introduce additional energy levels just beneath the conduction band for n-type doping and just above the valence band for$p$-type doping respectively. n-type and p-type refers to the charge of the majority carriers responsible for conduction n-type for electrons which are negative and p-type for electron holes which are positive. This act of doping tailors the electronic structure of the material, with even small changes having potentially dramatic impact: 1 part per billion of a donor impurity in germanium can increase its conductivity by a factor of 1000 [32].

Graphene has yet to live up to its full potential, most of which is locked behind the difficulties of developing scalable production techniques. Whilst the technology for manufacturing pristine sheets of graphene has been developed, efficient methods of patterning it and imparting a bandgap for use in devices remains elusive. Attention has thus turned in recent years towards how to better pattern graphene and assemble structures *in situ*, an approach broadly called the "bottom up" method of fabrication. An exciting avenue of research in this regard has been in the usage of small molecules, typically polyaromatic hydrocarbons (PAH), as building blocks. PAHs are to some extent small graphene flakes. Through careful selection of suitable substrates and design of functional groups these can be "programmed" to self assemble into complex supramolecular arrays and covalently bonded networks.

4

Self assembly of PAHs is a viable method of producing nanostructured graphene in various forms, nanoribbons [9, 15, 33] and porous graphene sheets [34] being most relevant to this thesis. Tailoring the structure of graphene at this scale tailors its electronics properties and self assembly from PAHs can pattern graphene at molecular length scales with precision beyond what is achievable through top down approaches. Whilst we can characterise the novel materials and structures formed through self assembly of PAHs, self assembly is still some way from being of use in practical device production. The principles of self assembly have been applied effectively to larger molecules, i.e. carbon nanotubes, for on–chip transistor fabrication [35].

Whilst graphene has struggled to reach the commercial market, electronics built using organic molecules and small PAHs have been available for several years now, seeing use in thin film transistors, photovoltaics and flexible displays [36]. Developing these device to where they can compete with inorganic semiconductors has been difficult due to the complexity of molecule–molecule and molecule–substrate interactions. Even for relatively simple systems such as nonreactive PAHs weakly adsorbed atop a substrate, the interactions that govern the system are complicated. Molecule–substrate and molecule–molecule interactions compete to dictate the ordering of the system. The magnitude of these interactions are dynamic and dependent on a large range of variables such as molecular coverage, temperature and the molecule and substrate structures themselves. By studying these interactions improvements have been made in organic devices, OTFT carrier mobilities surpassing those of amorphous silicon is a recent milestone. This has been achieved by only slight improvements to the electronic coupling between neighbouring molecules via their quality of ordering leaving room for advancement [37, 36]. Introducing substituent groups and atoms to PAHs is an area of active interest, this influences the

packing structure but also the electronic structure of individual molecules simultaneously [38, 39]. Optimising these interconnected parameters is a major challenge facing molecular electronics, one that can only be surmounted by improving our understanding of interactions between molecules at the surface.

2

Solids and surfaces

"God made the bulk; surfaces were invented by the devil."

– Attributed to Wolfgang Pauli

2.1   Crystal structure

Any material is a crystal providing it has a discrete diffraction pattern [40]. The criteria for a diffraction is that the system must possess a systematic and long range order to their structure. This definition succeeds an earlier, that mandates a crystal must be a periodic structure. A change in this understanding was brought about by the discovery of quasicrystals which are highly ordered systems that possess "forbidden" orders of symmetry (5,8,10,12) resulting in an aperiodic yet ordered structure [41, 42]. Quasicrystals fall outside the works presented in this thesis and so discussion in the following sections is limited to periodic systems. The structure of a crystal is describable by a repeating arrangment of one or more atoms, the basis, repeated across an array of lattice points, **R**. **R** is described by a set of basis vectors $\boldsymbol{a}, \boldsymbol{b}, \boldsymbol{c}$ that can repeat to fill all space and so:

$$\mathbf{R} = x\boldsymbol{a} + y\boldsymbol{b} + z\boldsymbol{c}$$

Simple cubic   **Tetragonal**   **Orthorhombic**

a=b=c   a=b≠c   a≠b≠c

α=β=γ=90°   α=β=γ=90°   α=β=γ=90°

a=b=c   a=b=c   a≠b≠c   a=b≠c

α=β=γ≠90°   α=γ=90°, β≠90°   α≠β≠γ=90°   α=β=90°, γ=120°

Rhombohedral   **Monoclinic**   **Triclinic**   **Hexagonal**
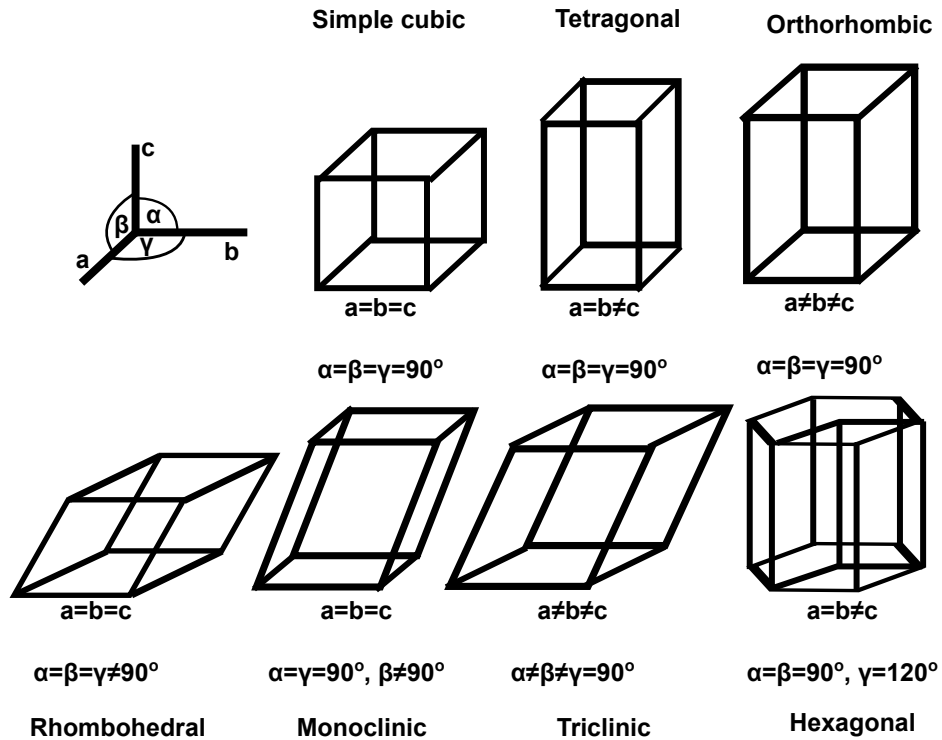
Figure 2.1: The 7 primitive crystal systems and their basis vector relations

,where x y and z are incremental integers [43]. Lattices are typically described by the smallest repeating structure within them, known as the unit cell [44]. These unit cells are unique to each system but their periodic nature means they are symmetry restricted. The simplest 3D structure to describe is the cube. Through deformation of this single unit we can form 7 distinct systems through reduction in their total symmetry. These are shown in figure 2.1 and expressed as a function of their edge lengths and angles.

From these primitive descriptions we can create a further 7 distinct lattices by distributing additional symmetry constrained points within the lattice. These arrangements are primitive, body-centred, face-centred and base-centred. [45]. These 14 unique lattices in total are known as Bravais lattices. For each Bravais lattice there are several distinct arrangements for which atoms can be arranged within the

lattice, preserving the Bravais symmetry. Each arrangement is known as the point group of which 32 are unique. The point group of a Bravais lattice provides a full site description of the, symmetry independent, atomic basis comprising the crystal [43]. The point group neglects translational symmetry operations which when considered means a crystal must conform to one of 230 space groups.

To describe periodic properties of crystals we often define them in reciprocal space as it aids description of periodic features. The reciprocal lattice of a system $\mathbf{G}$ is defined so that

$$\mathbf{R} \cdot \mathbf{G} = 2\pi l,$$

where l is any integer [43]. The relationship between the primitive lattice vectors and the reciprocal lattice vectors are as follows, where $*$ denotes reciprocal vectors:

$$\boldsymbol{a}^* = 2\pi \frac{\boldsymbol{b} \times \boldsymbol{c}}{\boldsymbol{a} \cdot (\boldsymbol{b} \times \boldsymbol{c})} \quad \boldsymbol{b}^* = 2\pi \frac{\boldsymbol{c} \times \boldsymbol{a}}{\boldsymbol{a} \cdot (\boldsymbol{b} \times \boldsymbol{c})} \quad \boldsymbol{c}^* = 2\pi \frac{\boldsymbol{a} \times \boldsymbol{b}}{\boldsymbol{a} \cdot (\boldsymbol{b} \times \boldsymbol{c})}$$

2.2 Surfaces

At some point a crystal will terminate, creating a surface. This results in the truncation of chemical bonds and an absence of neighbouring atoms. Compared to atoms within the bulk, surface atoms experience different forces and potentials and are often left with dangling bonds. The uneven potentials at a surface can result in a new equilibrium structure being more favourable than the bulk arrangement. This can be expressed through reconstructions of the surface structure such as the herringbone motif observed on the Au(111) surface [46] or just relaxation of the bond lengths [3]. Relaxation for single metal crystals typically means contraction of the interlayer spacings for the first few layers. This is known as normal relaxation [2]. Uniform, parallel displacement of atomic layers near the surface is another form relaxation can take but is only usually seen for surfaces cut so as to produce a low
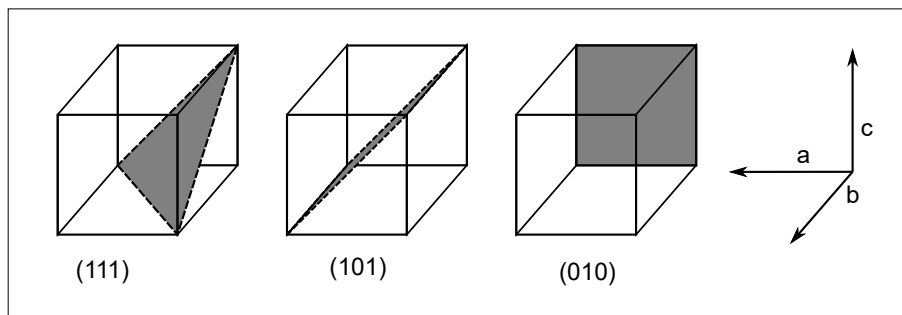
Figure 2.2: The miller indices describing surface planes through crystals are shown. The basis vectors of the crystals are shown on the right. The miller indices of a plane are always reduced to a set of integers with the lowest matching ratio.

atomic density in surface layers, this is parallel relaxation [2]. For many interactions the surface chemistry and its variable structure greatly influences processes such as catalysis, corrosion and epitaxy [47].

2.2.1 Surface notation

There are many ways a bulk crystal can terminate or be cut and the surface structure is determined by the angle of the cut. The plane of this cut can be described in terms of the unit cell vectors known as the Miller indices which take the form (abc). These indices correspond to where the surface plane intercepts the crystal axes given in units of the lattice vectors of the crystal [2, 32]. This is demonstrated in the examples provided in figure 2.2.

Reconstruction and overlayer notation

Wood's notation is used for describing one 2D unit cell as a function of another. This is a practical means to describe most surface reconstructions in relation to the bulk as well as well as adsorbed overlayers providing they share rotational symmetry. It defines the transformation required to obtain the overlayer vectors from the substrate vectors.
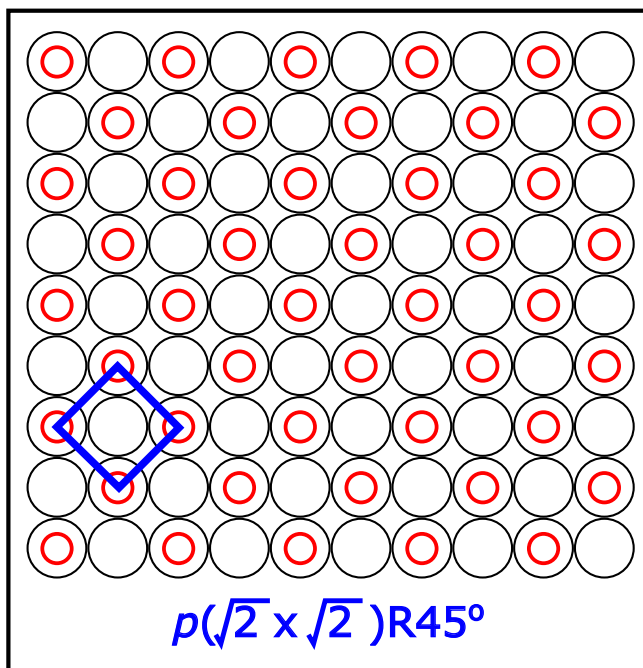
Figure 2.3: The red structure is a $p(\sqrt{2} \times \sqrt{2})\text{R}45°$ overlayer of the primitive surface lattice shown in black.

The structure $p(\sqrt{2} \times \sqrt{2})\text{R}45°$, applies to the reconstruction in figure 2.3 where the lattice parameters of the overlayer are a factor of $\sqrt{2}$ larger and rotated $45°$ in relation to the surface, resting upon the next nearest neighbours. Wood's notation is only applicable for systems where the reconstruction or overlayer is both commensurate and symmetrical to the substrate. Systems with conflicting symmetry that sit either coincident or are incommensurate with the substrate are better described using matrix notation. Matrix notation defines the overlayer in terms of the basis vectors of the substrate.

In the examples presented the adsorbate is situated atop atoms within the substrate. This is conventionally known as an "atop" adsorption site but other common sites exist as pictured in figure 2.4. Preference of an adsorption site is dependent on the chemistry and structure of both the adsorbate and substrate. In cases where an overlayer is commensurate with a surface the system will typically have a single favoured adsorption site. Long range commensurate and incommensurate structures
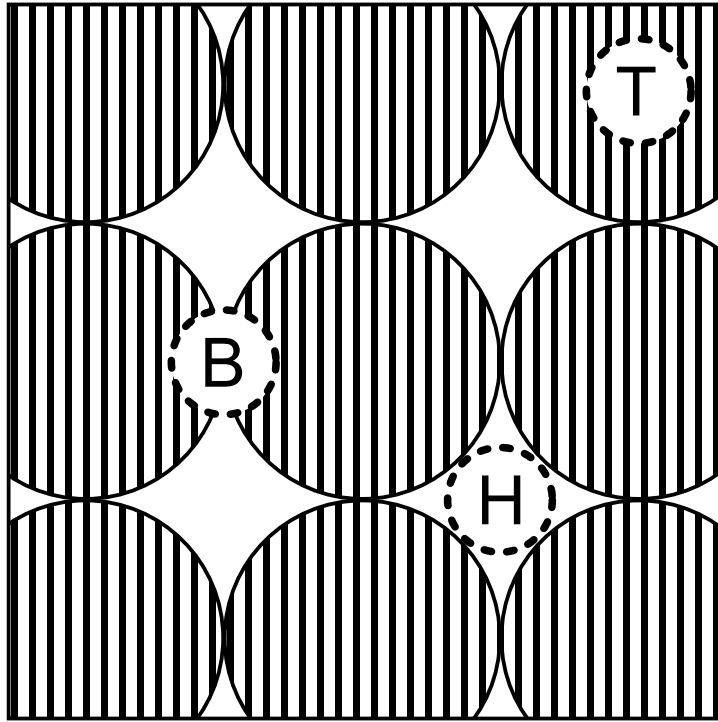
Figure 2.4: Common feature at the surface that form adsorption sites are the H (hollow), T (top) and B (bridge) sites.

are characterised by multiple or no preferred adsorption site respectively.

2.2.2 Commensurate and incommensurate structures

A commensurate system is one where the overlayer structure is quantised by periodic features of the substrate, I.e the overlayer spacing can be described using a multiple of the substrates lattice parameters. An overlayer that adsorbs commensurately will have each adparticle adsorb on a single type of adsorption site. Commensurate structures tend to arise when substrate–adsorbate interactions are dominant over lateral adsorbate–adsorbate interactions. In the case where adsorbate–adsorbate interactions play a more significant role, coincident or incommensurate structures can result. Coincident overlayer structures are characterised by adopting a periodic relationship with the substrate but occupying more than one adsorption site. In this case the overlayer is described by an non integer multiple of the substrate lattice.
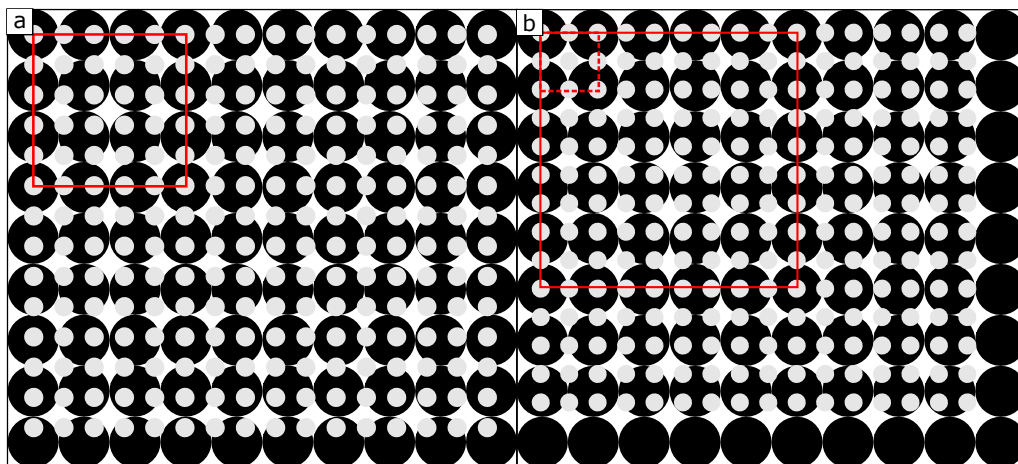
Figure 2.5: a) A periodic array of rings overlaid atop large circles illustrates a coincident structure, producing a periodic moiré pattern. b) Long range moiré patterns are unlikely for non rigid systems as with slight relaxation a smaller short range structure is possible.

In these instances either the variation in adsorption energy between different types of adsorption sites at the surface (see figure 2.4) is small, or the strength of the lateral adsorbate-adsorbate interaction is much larger than the adsorbate–substrate interaction. An incommensurate structure is one that shares an irrational relationship of lattice parameters to the substrate and is non-repeating. Molecular layers are compressible and so encountering a truly incommensurate adsorption system is unlikely, as are long range commensurate structures the greater their period across the surface. This is explored in figure 2.5.

2.3 Substrates

2.3.1 Coinage metals

The substrates in this study have been chosen based on their structure, surface symmetry and availability. The single crystals considered are coinage metals which are readily available and easy to prepare. Discovering an interesting system on rare expensive or difficult to prepare substrate is inherently of less practical use. For the purpose of this work "coinage metals" refers to the group 11 elements Ag, Au and Cu explicitly. These all share a face centred cubic unit cell with Cu having a significantly smaller lattice parameter compared to the others. The Cu(111) is a common system for studying PAH adsorption on due, with the unique property that its primitive lattice is close to that of the aromatic rings that form PAHs [48, 49]. Also of interest are the (100) faces of these metals. The square lattice of the (100) surface for these systems provides conflicting symmetry to the internal symmetry of PAH molecules and graphitic structures formed from them. In the case of Coronene, a PAH with 3-fold symmetry, this puts molecule–molecule interactions in conflict with the molecule-substrate interactions with regards to ordering. By varying the strength of the substrate–molecule interaction via the proxy of substrate element, it is possible to more thoroughly investigate the balance of molecule–molecule and substrate–molecule interactions.

2.3.2 $Al_4(Cr,Fe)(100)$

Complex metallic alloys (CMAs) are characterised as large unit celled, multi-element, (commonly ternary) alloys. We consider only one in the body of this work, $Al_4(Cr,Fe)$ a quasicrystal approximant. $Al_4(Cr,Fe)$ features a large, mostly Al unit cell with icosahedral clusters throughout but an overall orthorhombic unit cell. Quasicrystals and their approximants terminate in a manner so that their surface free energy
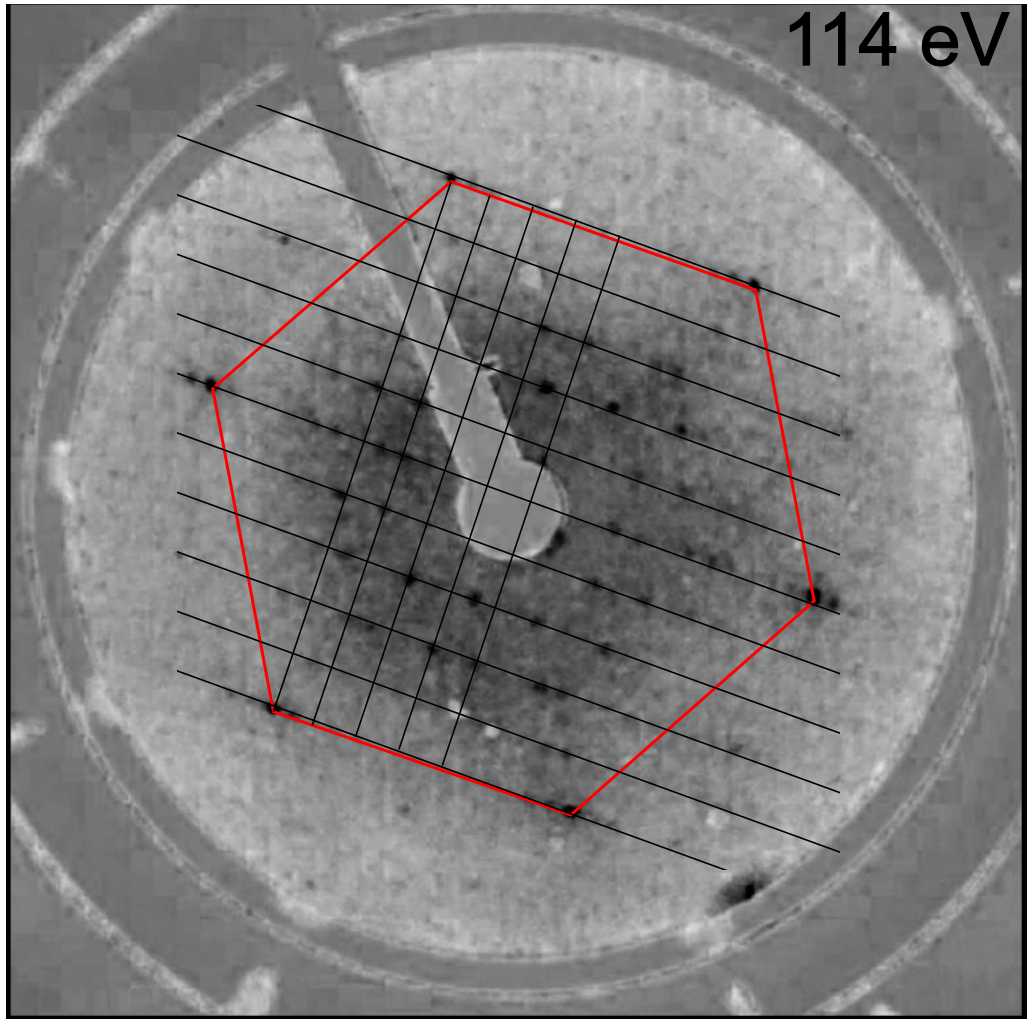
Figure 2.6: LEED pattern of the $Al_4(Cr,Fe)(100)$ surface illustrating the 3-fold localised symmetry arising from atomic clusters (red hexagon) and the overall 2-fold periodicity of the unit cell symmetry present at the surface.

is minimised, for Al-TM-TM systems this coincides with Al rich layers [50, 51]. These crystals terminate without reconstruction i.e their surface structure is a direct truncation of the bulk. Studying the $Al_4(Cr,Fe)(100)$ surface we see the short range 3-fold periodicity of the icosahedral clusters preserved along side the 2-fold symmetry of the unit cell as in figure 2.6.

Atomic adsorption studies on CMAs have shown that Pb and Bi form mono-element pseudomorphic thin films [51]. Studies using molecules have demonstrated templated adsorption of aromatic molecules on Al based CMAs using C_{60} molecules

[52, 53] and pentacene atop a Ag based quasicrystal [52]. In the case of approximants this templated adsorption tends to create localised disorder of interest to nanostructured thin films [53, 54]. $Al_4(Cr,Fe)$ provides a unique environment for studying the effects of symmetry conflicts in molecular ordering over extended and periodic distances as molecules adsorbed atop 3–fold surface features will encounter periodic symmetry conflicts at the 2–fold boundary to neighbouring unit cells.

3

Molecules at surfaces

3.1 Adsorption

The process of adsorption is split into the categories of chemisorption and physisorp-
tion. Making a distinction between these can be difficult in practice, being depen-
dent on the definition of what constitutes a chemical bond during molecule–surface
interactions [55]. In general these relate to strongly and weakly bound adsorbates
respectively, with older literature making this distinction often with just the adsorp-
tion energy as the discriminator between the two [56]. Another definition considers
the mechanism of adsorption directly, the weaker physisorption is predominantly
mediated by purely van der Waals interactions between the molecules and the sub-
strate. Whilst charge redistribution occurs in this process, it is confined to the
adsorbate and substrate separately [3] i.e. there is no *charge transfer* between the
two. In general the weak molecule–substrate interaction means that physisorbed
molecules more readily diffuse across a surface and often have translational, rota-
tional or oscillatory degrees of freedom [3].

Chemisorption refers to a molecule–substrate interaction, typically characterised
by an exchange of electrons or valence bond formation [57, 3]. This produces a
corresponding greater adsorption energy and as a result the adsorbate and substrate

are typically in much closer proximity to one another. Compared to physisorption the process may not be reversible and may require an activation energy to trigger.

In 1972 IUPAC addressed the chemisorption and physisorption distinction, asserting that no sharp line can be drawn between the two processes in terms of strength. They point out that edge cases overlap such as with strong hydrogen bonding or the occurrence of weak charge transfer [57]. The following section expands upon the forces underpinning physisorption and the mechanisms of charge transfer which mediate chemisorption.

3.1.1 Physisorption forces

The van der Waals forces are comprised of 3 components, dipole–dipole interactions, the London dispersion forces and the Pauli exclusion principle.

Dipole–dipole interactions

Dipole–dipole forces occur in polar molecules. This polarity arises from an uneven electron distribution between constituent groups or atoms and the imbalance results in alignment and attraction with neighbouring molecules. Strongly electronegative or electropositive atoms within a molecule make it polar. Electronegativity is a measure that relates the power of an atom to attract electrons to it within a molecule. There are different ways to measure this property, the Pauling and Mulliken scales being most common but in general looking at a periodic table along the top and to the right and along the bottom and to the left are where the most electronegative and electropositive elements reside respectively [58].

The strongest variant of the dipole–dipole interaction is hydrogen bonding as illustrated in figure 3.1(c). This occurs for molecules with a highly electronegative constituent; either oxygen, fluorine, or nitrogen, bonded with hydrogen. This arrangement produces an extremely strong dipole across the molecule and is the

strongest of the van der Waals forces. The classic example of this is the highly polar behaviour of water that results in alignments resulting in a low density structure when freezing. Hydrogen bonding in the context of adsorption has been observed to play a significant role for ethanol adsorption on alumina and silica surfaces [59].

A weaker dipole system known as the induced dipole interaction occurs between a polar molecule and a non polar or charge neutral neighbour. In this case, close proximity to the electrostatics of the polar molecule induces charge separation in its neutral neighbour. This is illustrated in figure 3.1(b).

Dispersion forces

For non-polar molecules, temporary charge imbalances across the molecule can create momentary dipoles. In close proximity these can interact with the dipoles of neighbouring molecules and manifest as an attractive force between them. Larger molecules with higher energy valence electrons are more susceptible to these imbalances, a property known as polarizability.

Repulsive interactions

The Pauli exclusion principle prevents the collapse of molecules. This can be approximated as falling off at $\frac{1}{r^{12}}$. This is not the only form of repulsive interaction however, direct Coulombic interactions between similarly charged molecules are significant over much longer distances which we can see by application of Coulomb's law fall off at $\frac{1}{r^2}$

3.1.2 Charge transfer and chemisorption

Chemisorption is generally defined by charge transfer between constituents. This is the basis for chemical bond formation [3]. Any adsorption process physical or chemical will exist on a overlapping spectrum of interactions driven by competing
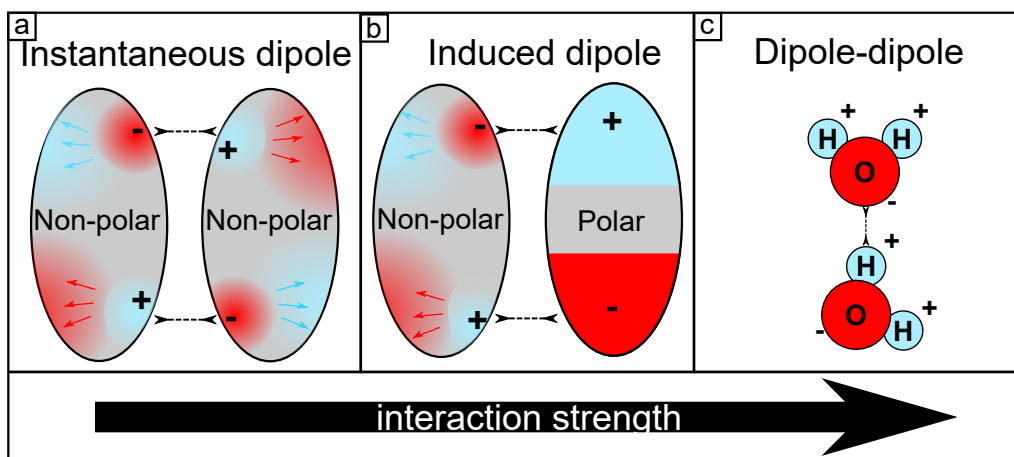
Figure 3.1: Illustration and summary of dipole interactions a)An example of an instantaneous dipole A.K.A the London dispersion force: a random charge imbalance within non-polar molecule induces a dipole imbalance in a non-polar neighbour b) an induced dipole where a polar molecule interacts and induces charge separation across a charge neutral neighbour. c)dipole dipole / hydrogen bonding.

electrostatic forces and energy minimisation. As with van der Waals interactions, we can classify chemisorption based on its dominant mechanism. Chemisorption and chemical bonding comes in three forms, covalent, metallic and ionic [60] but every bond is always a combination of some or all these interaction types [61].

Covalent bonding

In covalent bonding an electron is shared between atoms to complete their valence shells via orbital overlap and hybridisation. Bonding under this heading can be varied and accounts for the chemical properties of a molecule as much as the constituent atom elements. The classic example of this being the sp^2 and sp^3 bonding forms of carbon that change the structure from graphite to diamond respectively. Covalent bonding comes in the form of σ, π and δ bonds, the former two are most relevant for the systems considered with δ bonds being a rare case. σ bonds are symmetrical about the bond axis and are the strongest covalent bonds through the direct overlap of orbitals in this axis. π bonds overlap perpendicular to the axis with a node of

zero electron density in the axes of the parent nuclei.

Metallic bonding

Metallic bonding results from the electrostatic force exerted between a delocalised sea of electrons shared between positive atomic nuclei. The latter are structured as a lattice of cations separate to the valence electrons [58]. Metallic bonds are comparable to non directional covalent bonds on some level. A pathway between the two can be found by increasing the coordination number of a covalently bonded atom. This increases the delocalisation of valence electrons till they effectively enter the conduction band [61].

Ionic bonding

In ionic bonding one atom donates an electron to another, ionising both to form a bond. This process is similar to covalent bonding but occurs between elements with large differences in electronegativity where as covalent bonding applies to atoms with comparable values.

3.2 Adsorption

3.2.1 Isotherms

Isotherms attempt to model adsorption by relating the fractional coverage of a surface θ, to the adsorbate gas pressure, P, in a state of thermal equilibrium. When $\theta = 1$ the adsorbate has achieved monolayer coverage. The Langmuir isotherm is amongst the simplest adsorption models and based on several assumptions: Firstly that adsorption is limited to monolayer coverage, secondly that all adsorption sites are equivalent energetically and finally, that adsorbed molecules do not affect the ability of other molecules to adsorb at neighbouring sites [62].
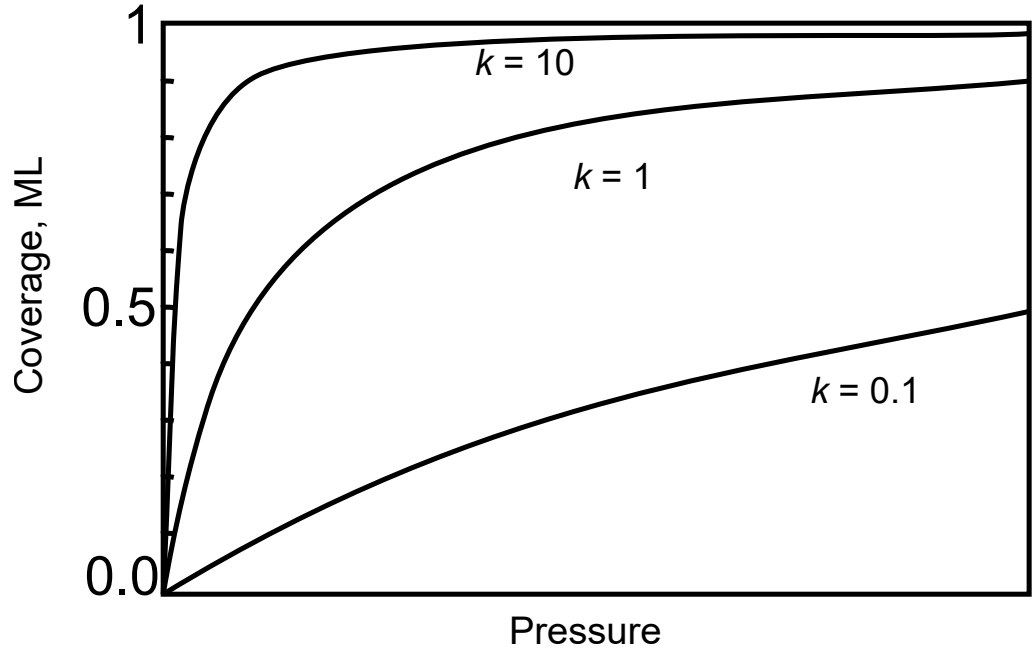
Figure 3.2: Langmuir isotherms for monolayer adsorption for various value of K, adapted from [2].

under these assumption the rate of adsorption, r_{ads} of adparticles can be expressed as

$$r_{ads} = k_{ads}P(1 - \theta)$$

and similarly the rate of desorption, r_{des} as

$$r_{des} = k_{des}\theta$$

where k_{ads} and k_{des} are the rate constants for adsorption and desorption for the system. In a state of thermodynamic equilibrium, $r_{des} = r_{ads}$ [2] and by substitution and rearranging for θ, we obtain the Langmuir adsorption isotherm for associative adsorption:

$$\theta = \frac{KP}{1 + KP} \quad \text{where} \quad K = \frac{k_{ads}}{k_{des}} \quad [3]$$

Langmuir isotherms for different values of K are presented in figure 3.2. For a greater values of K we see a steeper dependence on $\theta(P)$. For the same adsorbate

substrate system larger values of K correspond to lower substrate temperatures. For different systems at a fixed T, K corresponds to a greater adsorption energy [2].

For systems that fall within the limits of their assumptions isotherms are useful for comparing adsorption behaviours between systems. However a system of gas phase molecules in thermodynamic equilibrium with those adsorbed to a surface, is an atypical system in the context of experiments carried out in UHV. Adsorption and characterisation are normally separate stages so only relatively stable systems with low desorption rates are normally considered. It can be more useful to instead consider adsorption in terms of the adsorption potential energy.

3.2.2   Adsorption potential

Adsorption is ultimately an act of energy minimisation. The adsorption potential is a result of the van der Waals forces and chemisorption forces between substrate and adsorbate, in the case of non-activated chemisorption and physisorption, the adsorption potential is akin to the Lennard-Jones potential as shown in figure 3.3. The short and long attractive and repulsive forces seen in this model create a potential well about a minimum where an atom or molecule of sufficiently low energy can become trapped. The thermal energy of an adatom at RT 300 K is 25.8 meV (k_bT) whereas the binding energy, E_{ads} for a chemisorbed atom apart of the surface is typically 2-5 eV.

Chemisorption can take several forms, activated or non activated. In the case of activated adsorption a potential barrier exists to chemisorption, represented by E_{act} in figure 3.4. An exmaple of E_{act} might be the energy required to break chemical bonds in the presence of the surface for associative adsorption.

E_{ads} is the binding energy in the adsorbed state, E_{des} the barrier for desorption from the adsorbed state. For non activated chemisorption and physisorption the desorption energy is simply the binding energy in the chemisorbed state, $E_{des} =$
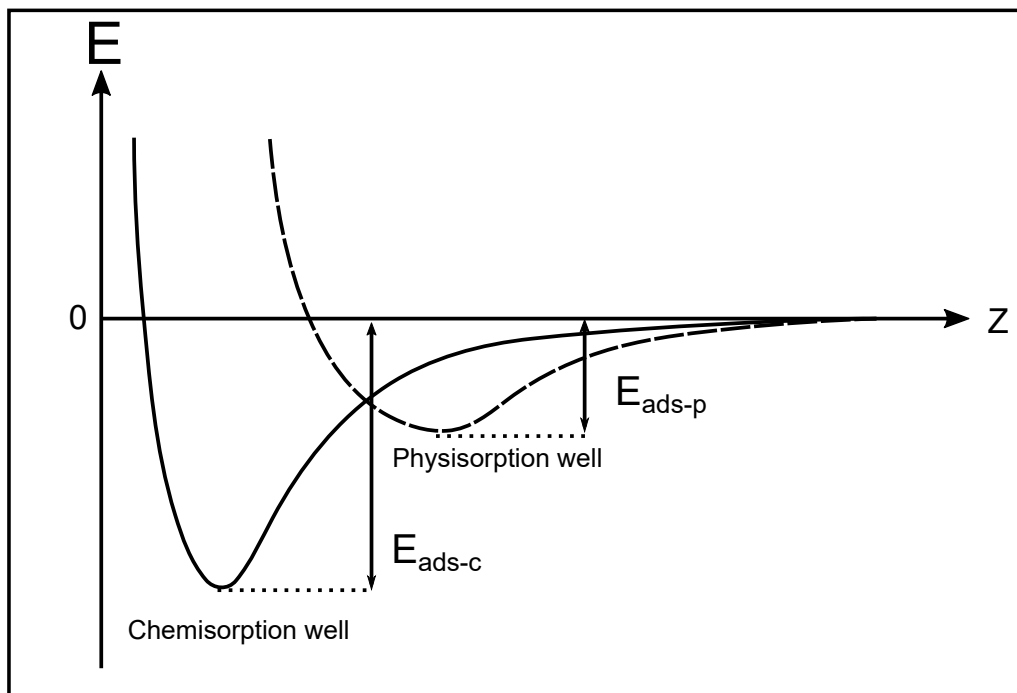
Figure 3.3: Possible adsorption potentials for physisorbed and chemisorbed molecules as functions of their distance from the surface. Chemisorption in this case is non-activated.

E_{ads} [2]. For activated chemisorption the desorption energy, $E_{des} = E_{ads} + E_{act}$. For a fixed substrate, larger homologous molecules experience stronger adsorption in general when compared to their smaller counterparts, an examples of E_{ads} for increasing length acenes adsorbed atop Cu(111) is presented in table 3.1.

Another feature evident in this work is the influence of surface defects, in this case terrace step edges, on E_{ads}. Adsorption sites along step edges and defects typically increase the coordination of adparticles adsorbed at neighbouring sites

Molecule	Cu(111) E_{ads} (eV)	Step edge E_{ads} (eV)
C_2H_4	0.33	0.45
C_6H_6	0.58	0.62
$C_{10}H_8$	0.92	1.07
$C_{14}H_{10}$	1.21	1.37

Table 3.1: E_{ads} of acenes adsorbed atop Cu(111), adapted from data presented in [63]
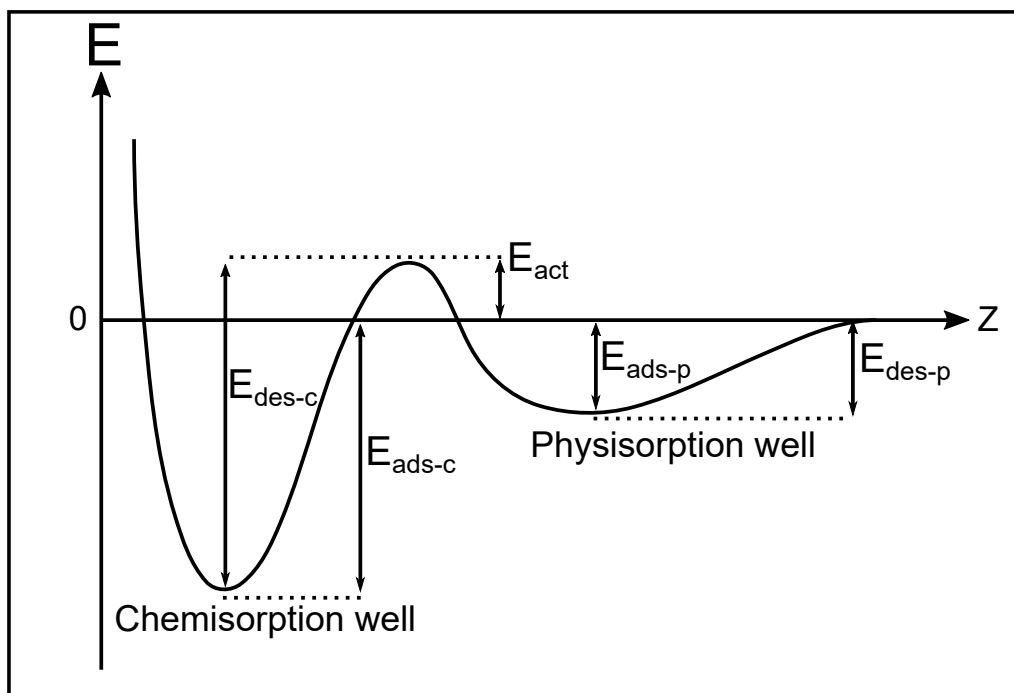
Figure 3.4: A potential energy plot for a molecule as a function of its distance to the surface. Two wells representing physisorption and activated chemisorption are illustrated. E_{ads-c} and E_{ads-p} represents the chemisorption and physisorption adsorption energies respectively. E_{des-c} and E_{des-p} represent the desorption energy barrier for chemisorption and physisorption resepctively. E_{act} represents the activation barrier to the chemisorbed state.

and so increases E_{ads} at theses locations. In the case of the acenes in table 3.1, this adsorption increase is equivalent to approximately 0.15 eV.

3.2.3 Surface diffusion

Surface diffusion describes the motion of adsorbed atoms or molecules across the surface of a substrate, made mobile through thermal activation. Surface diffusion is often necessary for surface atoms and adsorbed molecules to arrange in their minimum free energy configuration.

The motion of these adparticles can be described by the diffusion coefficient, D (cm^2 s^{-1}) which is the time-independent, ratio of the mean square displacement to time [2]. We can generally describe D as following Arrhenius-like behaviour and so

$$D = D_0 \exp\left(\frac{-E_{act}}{RT}\right) \quad [3],$$

where D_0 is a pre-exponential factor (cm^2 s^{-1}) unique to each system and related to the entropy change between the equilibrium adsortion site and the activated complex. T is the absolute temperature (K) and E_{act} is the activation energy barrier (kJ mol^{-1}) for diffusion [3].

The diffusion coefficient can be used to calculate the average distance travelled, $\langle x \rangle$ over time, t as follows: $\langle x \rangle = (Dt)^{1/2}$ [3] This assumes that all diffusion steps are of equal probability. Observing the motion of adparticles directly, via techniques such as scanning tunneling microscopy, it is possible to record $\langle x \rangle$ and so calculate D for a system experimentally [62].

The diffusion barrier for an adparticle is on average larger for atomically rough surfaces and this results in a larger values for D. Roughness in the context of surfaces refers to those with looser atomic packing or those cut so as to induce regular terrace steps (vicinal surfaces). As previously mentioned, E_{ads} for adparticles can be lower at surface step edges and in these situations the diffusion barrier to adjacent step sites
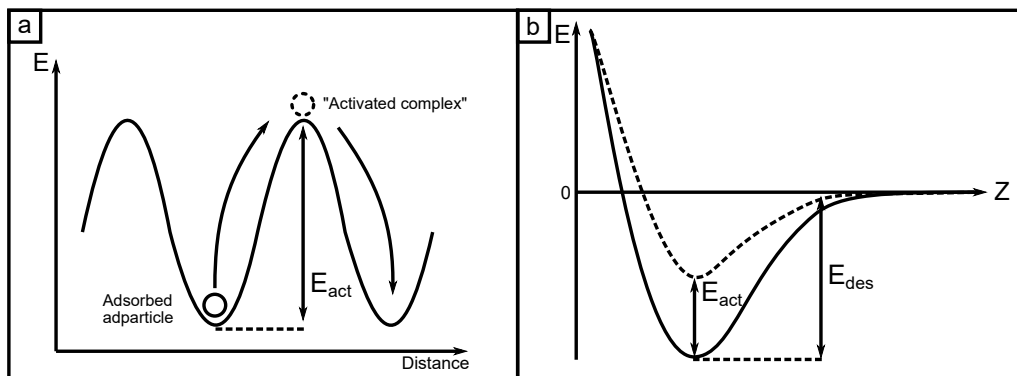
Figure 3.5: a) Plot of adparticle potential energy with respect to adjacent adsorption sites at the surface. The wells representing the adsorption sites are separated by a potential barrier to diffusion equal to E_{act} in height. Adapted from [3]. b) The potential energy diagram of the adsorbed adparticle in (a) as a function of distance to the surface. The dotted line denotes potential energy, raised by E_{act} of the activated complex in (a). The desorption energy of the adparticle is shown for comparison. Adapted from [2].

is less than to a neighbouring sites on the terrace. A natural extension of this is the nucleation of diffusing adparticles atop defect or step sites where they can become trapped. Whilst larger molecules can in general be said to have a larger E_{ads}, larger molecules relative to the substrate unit cell often occlude multiple adsorption sites, which can reduce adsorption site selectivity and E_{act} for diffusion [64].

3.2.4   Adsorptions effect on the work function

The minimum energy required to liberate an electron from a solid by raising it from the Fermi level to the vacuum level is known as the work function ϕ. This varies depending on the elemental composition of the solid but also on the surface termination. The work function is a result of the electronic structure of a surface but also dependent on a phenomenon known as the surface dipole.

Electrons are bound to the solid but their wave functions extend into the vacuum with an attenuating amplitude. This is known as electron overspill. To conserve charge, an excess of positive charge manifests in kind at the solid surface forming

27

a dipole layer across these regions. Close packed surfaces have a greater atomic concentration and so have a greater density of electrons and electron overspill and a correspondingly stronger surface dipole [3]. A larger surface dipole means a larger work function as has been shown experimentally for varying Cu surfaces: $\phi_{\text{Cu}(111)} = 4.94$ eV $\phi_{\text{Cu}(100)} = 4.59$ eV and $\phi_{\text{Cu}(110)} = 4.48$ eV [3].

Adsorption of molecules or atoms adsorbed to the surface can similarly change the surface dipole and influence the local work function of the surface as a result. This can manifest in several ways, firstly the "pushback" effect, where the electron overspill from the surface is repelled by the electron density of the adsorbed molecule, this effect is always present [65]. Secondly any permanent or adsorption induced molecular dipole must be added or subtracted to the surface dipole, depending on its orientation. Finally charge transfer during adsorption will inherently alter the surface dipole by changing the electron density within the surface and adsorbed molecules [65]. The surface dipole is important because of its effect on the energy levels of adsorbed molecules and the substrate, which ultimately dictates the electron and hole injection barriers between the molecule-substrate interface and so the electronic properties of the junction [65].

3.2.5 Molecule–molecule interactions

Assuming neutral molecules, a pair of molecules will experience attractive van der Waals forces and a potential between them similar to the Lennard-Jones like potential discussed with reference to adsorption. This attractive interaction often has a role in the formation of islands and ordered molecule structures atop surfaces. The manifestation of molecular structures and ordering at the surface is a function of both the adsorbate–adsorbate interactions and adsorbate–substrate interactions [66]. Additionally substrate–molecule and molecule–molecule interactions are not isolated from one another, substrate mediated interactions (SMIs) are ones induced

between molecules by their relationship through the substrate [67]. This interplay of interaction mechanisms makes the ultimate behaviour and structure of adsorbing molecules difficult to predict. In this section we discuss some important factors to intermolecular interactions for PAHs and behaviours that can be observed following adsorption.

Multilayer growth

The growth behaviour of thin films is dependent on the relationship of adsorbate and the surface. In figure 3.6 the three main growth modes are illustrated. Where adsorbate-surface attraction is stronger than the attractive adsorbate-adsorbate interactions layer-by-layer growth, AKA Frank-van der Merwe growth, takes place where each adsorbate layer is completed before subsequent layer growth begins [2]. In the case where attractive adsorbate-adsorbate interactions are greater than adsorbate-substrate interactions then island growth, AKA Vollmer-Weber growth, takes place where 3D islands nucleate and grow from the surface prior to full surface coverage [2]. A hybrid of these systems occurs in the case of Layer-plus-island growth, AKA Stranski-Krastanov growth takes place where a full layer, or multilayers, form after which 3D island growth proceeds [2]. This arises from the changing structure or strain experienced by the adsorbate in layers removed from the surface. An adsorbate initially templated the surface structure might relax into a different structure in subsequent layers, a structure disposed to 3D island growth. This is a situation commonly encountered in physisorbed molecular systems [68].

Chemisorption of molecules in general precludes the formation of multilayers due to the close proximity required for charge transfer and bond formation [57]. Chemisorbed monolayers are in effect self passivating but this does not preclude further layer growth through physical processes. As molecules adsorb on a surface, even for physisorption the electron distribution within them and the substrate is
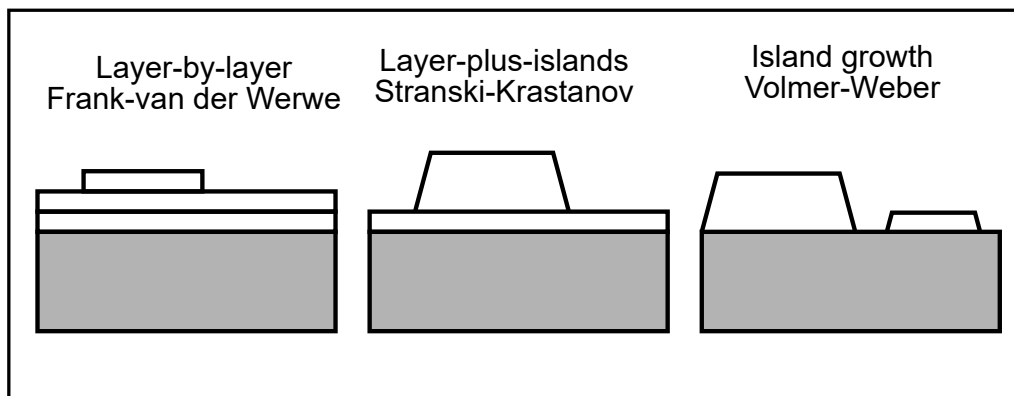
Figure 3.6: Schematic illustration of the three main thin film growth modes.

altered meaning a unique chemical environment is created in the presence of an adsorbed molecule.

$\pi - \pi$ interactions

A C atom has the electron configuration $1s^2$ $2s^2$ $2p^2$ and within PAHs, graphene and graphite these form 3 planar $2p^2$ hybridised orbitals comprising the 2s $2p_x$ and $2p_y$ electrons, forming σ bonds. H terminated, these systems contribute weakly to intermolecular interactions in their plane beyond Pauli repulsion and weak hydrogen bonding [64] (C being slightly more electronegative than H). Perpendicular to the plane of the molecule, from each C atom extends π orbitals corresponding to the $2p_z$ electrons [69]. The π orbitals effectively form a plane of delocalised electrons either side of the aromatic molecule in question, illustrated in figure 3.7. Interaction between π systems is a particular case of dispersion force but one with a strong impact on the electronic properties of molecular systems. The charge carrier mobilities across PAH systems is largely dependent on electronic coupling via the overlap of π systems of neighbouring molecules [70].

In general stronger coupling of π–π systems results in a much shorter charge transfer time from molecules to the substrate [71]. Stacking between smaller PAHs is varied, figure 3.8 shows a small range of observed arrangements. These arrangements

30

σ bond   π bond
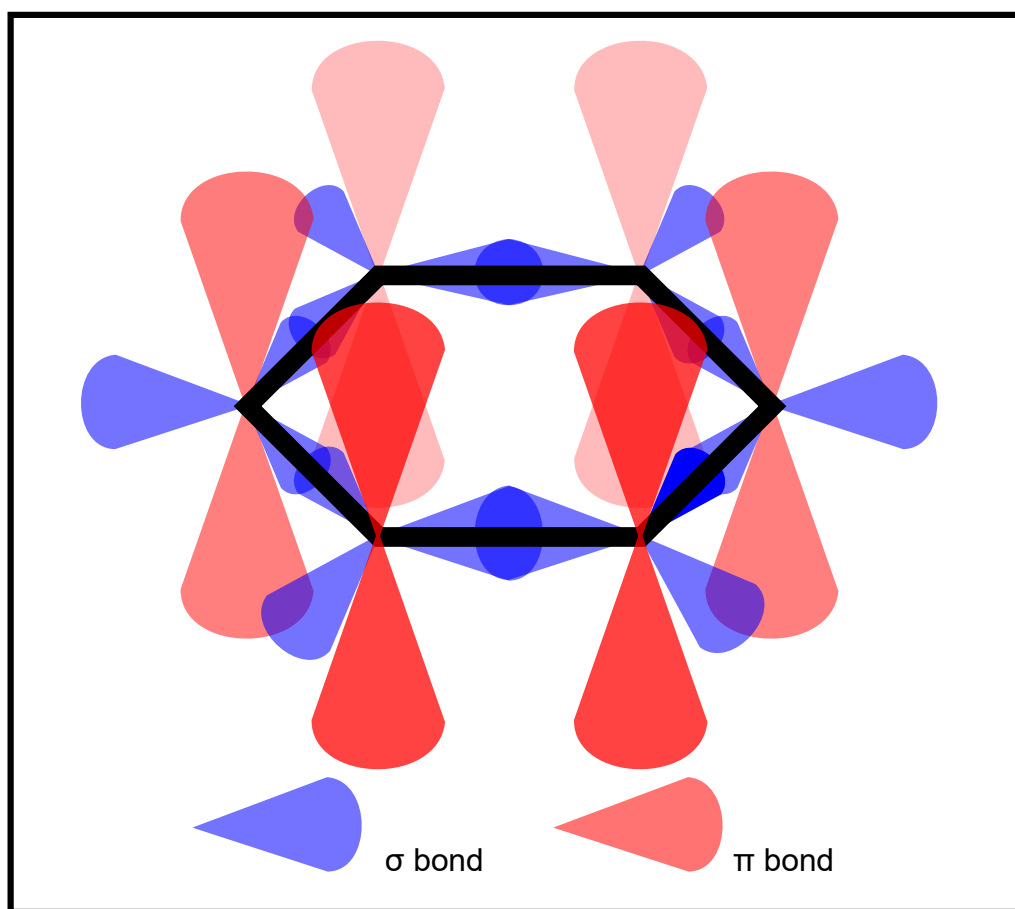
Figure 3.7: A bond diagram of a H terminated benzene ring, this structure forms the backbone of any PAH.
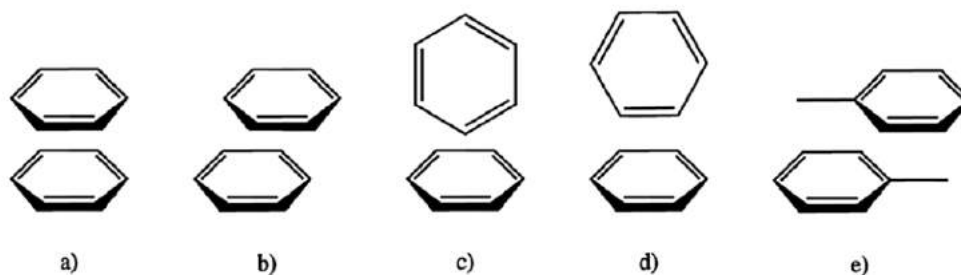
Figure 3.8: Possible aromatic stacking arrangements. (a) Parallel face-centred. (b) Parallel offset as seen in graphite layer stacking. (c) Perpendicular t-shaped. (d) Perpendicular y-shaped. (e) Parallel offset for toluene Reproduced from [4].

can be understood as arising from molecular quadrupole moments. The delocalised π system creates a region of negative potential either side of the ring plane and a positive potential along periphery [72]. The arrangements shown in figure 3.8(b-e) are typically more favourable maximising the contact between the negative centre and positive edges of aromatics molecules. The parallel arrangement in figure 3.8(a) represents a higher energy saddle point [73]. The most commonly observed structure for larger planar PAH crystals, such as pentacene or coronene, is a herringbone type structure, which maximises the quadrupole interaction between neighbouring molecules as in figure 3.8(c) and (d).

2D gas behaviours

Molecules at the surface can exist in the solid and gas counterparts expected of 3D systems but simply confined to the plane of a surface and under specific conditions can exhibit behaviour analogous to liquids [74]. In the solid phase molecules adopt close packing ordered structures but in the 2D gas phase molecules diffuse freely across the surface. The 2D liquid state whilst discussed in earlier literature [74] is poorly defined but in more recent literature 2D liquids are seen as diffusion inhibited 2D gases. Barriers to diffusion can arise through the dense packing of a 2D gas [66] but liquids typically still exhibit rotational degrees of freedom. The different
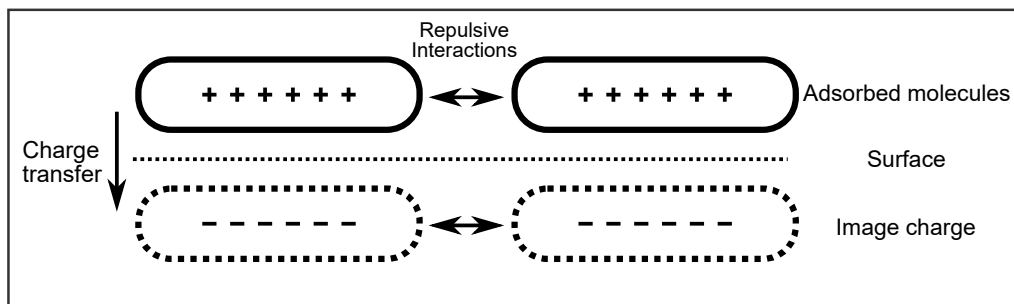
Figure 3.9: In the adsorption case where significant charge transfer occurs between the adsorbate and substrate, its possible for a significant dipole to form between the adsorbed molecule and a corresponding surface image charge. This can create a repulsive interaction between the electrostatic potentials of neighbouring molecules and their image charges as illustrated.

adsorption potentials of step edges and surface defects can act as nucleation points for 2D liquid behaviour [74]. Following adsorption of a molecule, charge transfer or the perturbation of the electron density of the surface can increase the binding energy for molecules at neighbouring adsorption sites [67, 74], giving the appearance of attractive intermolecular forces. Repulsive substrate mediated interactions can also occur, as has been observed in the space maximising 2D gas behaviour for coronene and perylene [75]. In this latter case the localised π orbitals are the dominant factor influencing adsorption, facilitating charge transfer resulting in a charged molecule sat above a surface mirror charge fuelling adsorbate–adsorbate repulsion. This behaviour has also been reported for Pn atop Cu/AlPdMn [76]. A diagram illustrating the repulsive interactions that can arise from image charges at the surface are presented in figure 3.9.

3.2.6 Chirality

Chirality is a geometric property of molecules that arises when a mirror transformation results a loss of translation symmetry for the structure [77]. If a molecule is chiral it has two enantiomers sharing mirror symmetry, being left or right handed versions of the same structure. There can be no translation or rotation of a "left

hand" molecule so that it will superimpose upon the "right handed" version. Chirality plays a huge role in all chemical science, the classic example being singular enantiomeric form of amino acid used by all life forms on earth. Isolating enantiomeric pure compounds for pharmaceutical purposes has driven research into chiral catalysis [78].

In the context of surfaces, chirality is easier to discuss as a result of the reduced degrees of freedom. There are three main instances where chirality can be expressed by molecules adsorbed on a surface. The innate chirality of the molecule in question, the chirality of the molecule once adsorbed (point chirality) and chirality expressed through the arrangement of adsorbed molecules (group chirality). It is possible for a surface to possess localised chirality where an overall racemic system is observed. Conversely a surface can be globally chiral with only one enantiomer present [5]. An example of this might be a surface where only one enantiomer can react in the necessary manner to adsorb to the surface.

The nature of surfaces restrict what possible arrangements can exist for group chiral arrangements significantly. Of the 230 possible 3D space groups, only 17 exist at the surface and only 5 after removing mirror and glide symmetry elements [5, 78]. These are illustrated in figure 3.11. The process of adsorption and confinement to a 2D surface can make previously achiral molecules adopt a chiral footprint [79, 5]. Molecules that adsorb in this fashion are known as prochiral and can be expressed as a form of point chirality or may manifest in group chiral arrangements. A prochiral molecule might react with the surface or otherwise structurally relax in a way that breaks the mirror symmetry of the molecule in an axis. An example of this is illustrated in figure 3.12.

Prochirality is not confined to point chirality within a single molecule. Chiral group assembles are valid expressions of this phenomena [5]. Studies have also found molecular systems where chiral phase transitions occur [80]. In these examples the

Non-chiral molecules

Adsorption induced chiral motifs.

-alignment of molecule breaks the reflection symmetry axes of surface:
local point chirality
(i.e. belongs to a chiral point group).
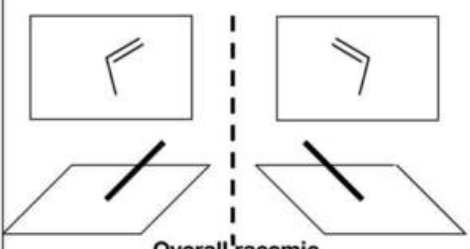
Overall racemic

Adsorption induced chiral arrangements (or domains).

-the ordered domains possess a chiral space group:
local organisational chirality.
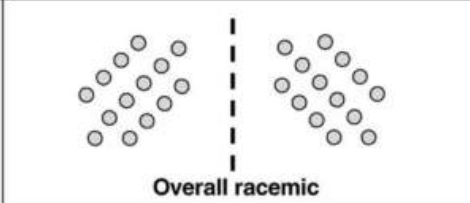
Overall racemic

Chiral molecules

Molecule induced chiral motifs.

-intact preservation of chiral centre upon adsorption I.e. creates local chiral point group:
global point chirality.
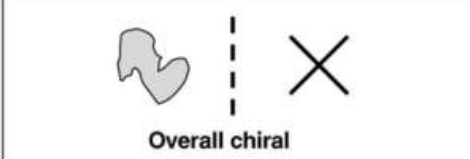
Overall chiral

Adsorption induced chiral arrangements.

(i) asymmetric lateral interactions
e.g. mediated by groups that are non-chiral
- reflectional domains allowed:
global point
and
local organisational chirality.
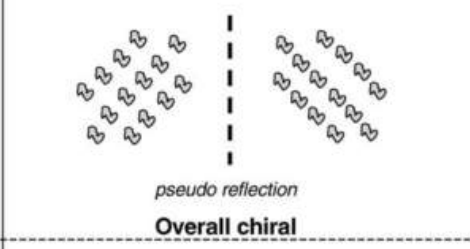
pseudo reflection
Overall chiral

(ii) chiral lateral interactions- no reflectional domains allowed:
global point
and
global organisational chirality
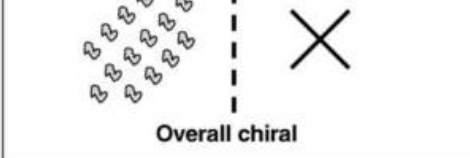
Overall chiral

Figure 3.10: Illustration of the differing chiral systems possible between molecules and surfaces [5].

35
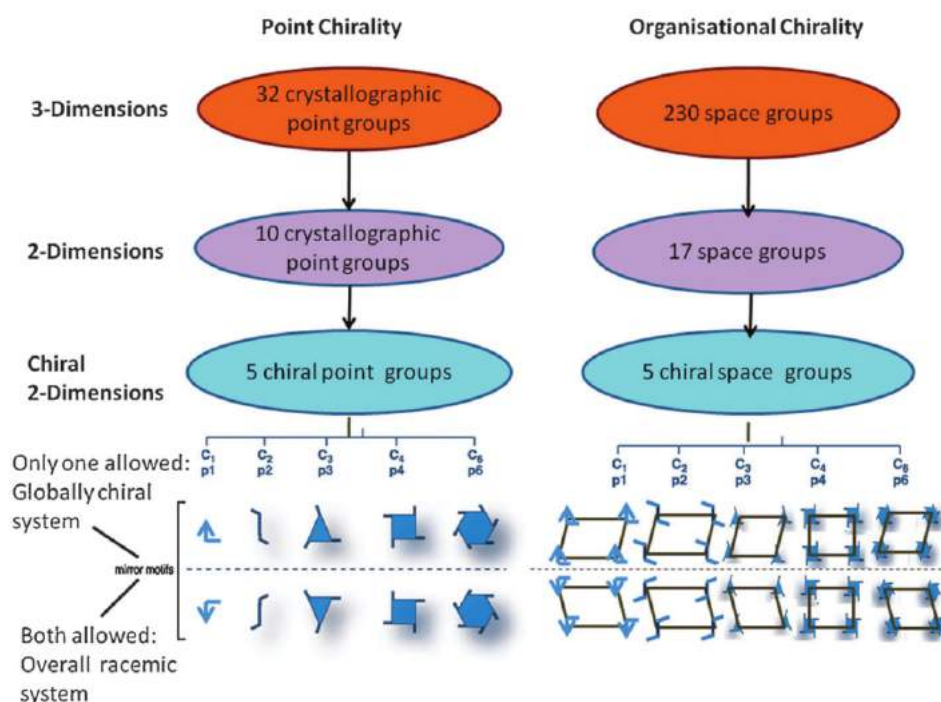
Figure 3.11: Space group restrictions when constrained by the surface and chiral conditions [6].
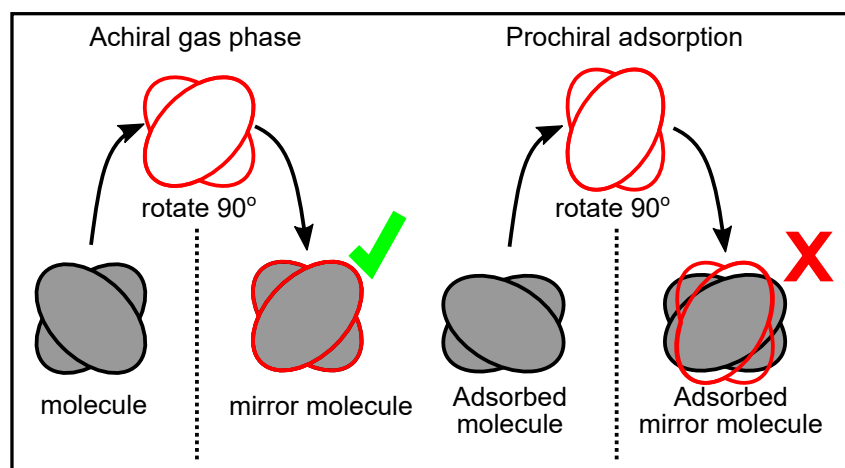
Figure 3.12: Achiral molecules in the gas phase are shown above on the left, the mirror image can be achieved through a 90° rotation. During adsorption the same molecules relaxes, its structure flattening. This molecule is prochiral upon adsorption, no rotation of the adsorbed molecule replicates its mirror image. The adsorbed molecule and its mirror image are separate enantiomers.

competing molecule–molecule interactions that govern enantiomeric ordering can result in dramatic structural changes at different surface coverages.

3.3 Molecular electronics

3.3.1 The case for using molecules

In using molecules over conventional inorganics for semiconductor devices we encounter an apparent contradiction to our end goal. Molecules are a much larger building block than individual atoms. The smallest structure we can build is now limited to the smallest dimension of a molecule but ultimately the limiting factor in device creation has never been the size of the building block but in the precision of the tools used to create it. Additionally a single atom is of limited use but a molecule can serve as a self contained device such as a diode or transistor [81, 82]. Modern device fabrication has been lithographically focused. This process typically functions by patterning a substrate with an etch resist and removing the exposed material. Electron beam etching (e-beam etching) has been prominent in achieving the precision for manufacturing small scale devices. It is a time intensive process limiting its suitability for mass production. The etch technique and the granular resolution of the resist material are both limiters to the ultimate resolution of the device. Etch quality is mostly limited by the line edge roughness of features etched (LER) [7].

Working with molecules as opposed to atoms is akin to building a house from bricks as opposed to sculpting one from cob/mud/daub (whichever is regionally appropriate) as in figure 3.13(a) and 3.13(b). In this analogy the bricks represent our molecules and in assembling our house or device from them it might seem that we have sacrificed flexibility for uniformity, but the reality is that the burden of design is shifted from assembling and sculpting the house to the brick firing stage. By designing bricks appropriately we can in replicate the patterning of cob sculpting
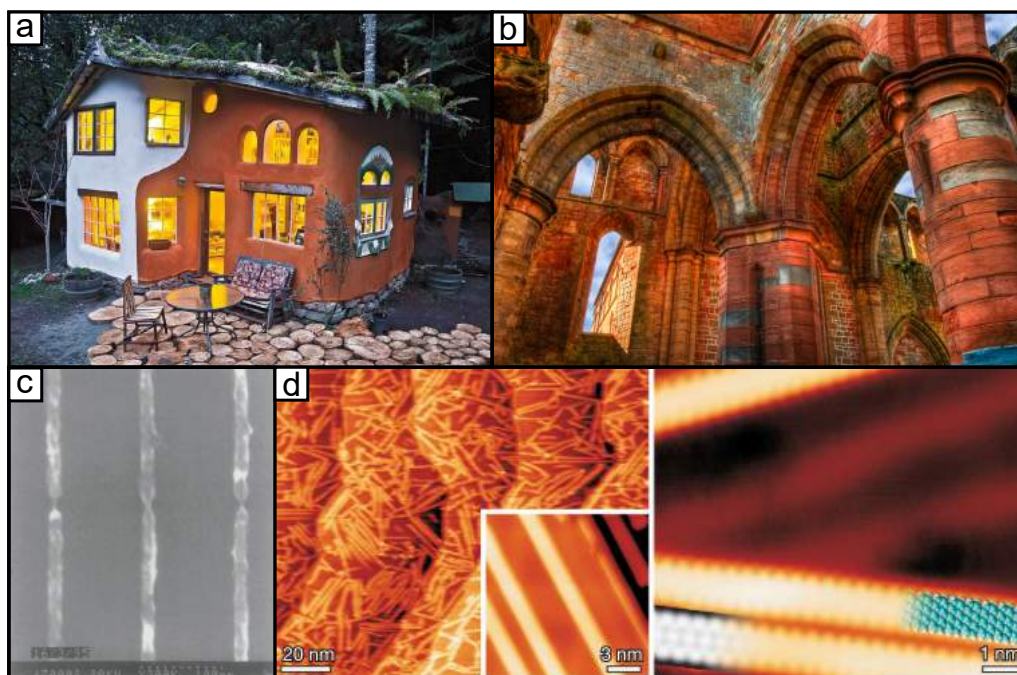
Figure 3.13: a) A house of cob walls that are sculpted after construction. b)Ornate brick work made possible by custom fired bricks. c) Nanowires patterned through electron beam lithography [7, 8] d) Nanowires formed through molecular self assembly atop Au(111) [9]. The right hand close up has an atomic model overlain.

analogous to lithography, and in practicality exceed it. As stated previously the barrier to atomic resolution in patterning inorganic devices are the processes and tools used. In contrast, we can tailor the precise atomic structure of molecules relatively easily. If we design molecules with self assembly in mind we can, in principle, achieve atomic precision in nanoscale structures providing we have full understanding of the reaction processes. The self assembly processes are akin to the stacking techniques and mortar used in bricklaying, in this now straining comparison to building materials. Cob walls typically vary significantly along their length and this is similarly seen in lithography of inorganics, a property which is measured as the line edge roughness (LER), typically the standard deviation of the etched line thickness [7]. By using molecules/bricks our walls/wires should always be one molecule/brick wide, but this understates the complexity of self assembly at surfaces where multiple reaction pathways can exist. As we will see in chapter 6, the self assembly process can vary dramatically from surface to surface for a given molecule and so attempting to exploit interactions to create nano–structured materials by design or with regularity, is a non trivial task. A comparison of wires formed through lithography and molecular self assembly are presented in figure 3.13(c) and 3.13(d) where the LER problem encountered with the former is contrasted against the atomic precision of molecular self assembly achieved by Cai *et al.* [9].

3.3.2   Organic semiconductors

The field of organics semiconductors covers the use of π bonded molecules, amongst them polyaromatic hydrocarbons, PAHs, in the forms of molecular crystals or as thin films. Work has also branched into the study of single molecule electronics SMEs which is readily facilitated readily by STM techniques where the tip and substrate form the connecting electrodes [83]. Within this body of work our attention is focused on using STM to study thin films and the molecules within them and so

this section is written with this context in mind.

The idea of assembling electronics or devices *in situ* through "bottom up" approach has the potential to surpass the resolution limits of the top down approach of conventional techniques such as e–beam lithography. Furthermore the viability of roll-to-roll processing techniques on flexible substrates and solution based applications makes development of organic systems attractive for industrial scale production. [84]. The benefits of tailoring electronics through the bottom up development can only be realised through studying the interactions of such systems [65]. The electronic properties of organic molecules are readily tailored through functional groups and their crystal structure. These in turn can be controlled through growth conditions and substrate chemistry. These competing forces afford a great deal of control of molecular systems but introduce extreme complexity from a design perspective. One additional barrier to organic electronics design is the ordering forces, those within molecular electronics are mostly mediated by van der Waals interactions which fall off at $1/R^6$ compared to typically covalently bound inorganics which have a $1/R^2$ dependence [68] which means the quality of order within molecular structures, particularly in the case of organic polymers can be low. Maximising the strength of ordering interactions is an area of active interest in regards to optimising device efficiency as strong electronic coupling, mediated by the overlap of π systems on adjacent molecules, is a necessary criterion for ensuring high charge carrier mobilities [85].

3.3.3 Molecular rectifiers

Conjugated and aromatic molecules feature sp^2 bonding that creates delocalised electrons. Each π bond has a bonding and antibonding orbital, the latter being at a higher energy and typically unoccupied for a molecule in the ground state [60].
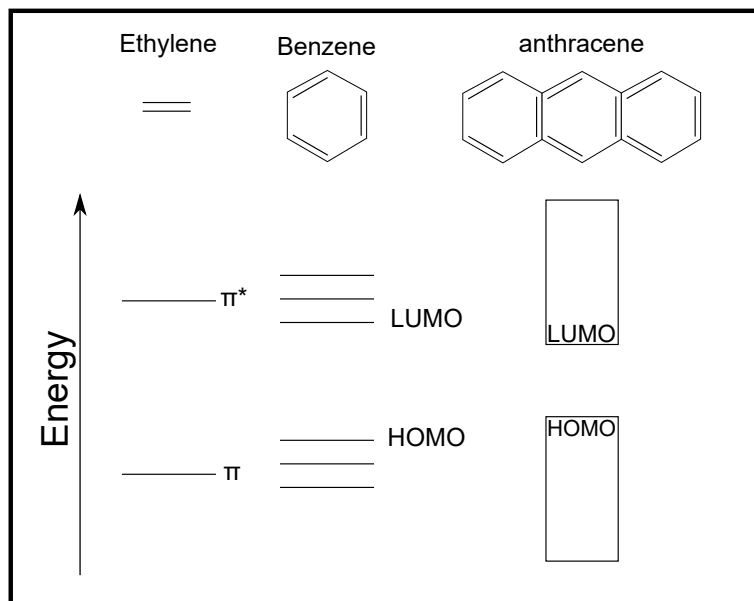
Figure 3.14: The energy levels corresponding to the bond and anti-bond splitting of each orbital in sp^2 bonded hyrdocarbons is shown. As the number of atoms within the hydrocarbon increases so does the number of orbital energy levels, the energy level splitting forming a band structure.

Each additional π bond within a molecule contributes an additional bonding and antibonding energy level to the bands of occupied and unoccupied orbitals within the molecule. The lowest unoccupied molecular orbital is akin to the conduction band and the highest occupied molecular orbital the valence band in inorganic semiconductors. Separating these is a band gap as in inorganic semiconductors as shown in figure 3.14.

We can create an inorganic p–n junction by use of n–doped and p–doped Si. In this junction, the majority carriers in the n–doped side are electron and the majority carriers for the p–type side are holes. At the junction of these materials is the depletion region, where electrons from the n–type material recombine with the holes in the p type material, creating a region of positive charge on the n–type side and a region of negative charge on the p–type side. The charge separation across the depletion region creates a potential barrier that must be over come to permit the flow of current. In forward bias, additional electrons are injected into the n–type

region and holes into the p–type region until this applied potential is greater than that across the depletion zone, dramatically increasing transport across the junction. In the reverse bias electrons are drawn away from the n–type region via an applied positive bias, increasing the depletion zone barrier and only a small leakage current flows as a result of minority carriers. This process is illustrated in the energy band diagram of a doped Si p–n junction is presented in figure 3.15. In this, we see the effects of applying a forward and reverse bias, V which shifts the energy levels of the p–type and n–type regions with respect to one another. At thermal equilibrium the potential barrier across the depletion region is equivalent to qV_b in height where,

$$Vb = \frac{k_b T}{q} \log \left(\frac{N_d N_A}{n_i^2} \right)$$

and where T is the absolute temperature, k_b is the Boltzmann constant, q is the elementary charge, N_d is donor impurity concentration, N_A is the acceptor impurity concentration and n_i^2 is the intrinsic carrier concentration, of Si in this instance. Application of a bias V shifts the energy levels of the p–type region with respect to those in the n–type and in doing so increases or decreases, dependent on bias, the depletion region barrier by qV.

Single molecule rectifiers were first proposed by Aviram $et\ al.$ in 1974 [82]. They outline the concept stating that a single molecule can function as a self contained diode or p-n junction by containing electron poor (p-type) and electron rich (n-type) sub-units connected by a spacer to prevent the formation of a single donor level between these, fulfilling a the role of the depletion region in a conventional p–n junction. [86, 82]. The properties of these subunits can be tailored by increasing or decreasing the π electron density within the molecule by attaching electron donating or electron withdrawing groups or susbstituents. In general, groups with electronegative constituents such as O, F and N reduce the π electron density, making the
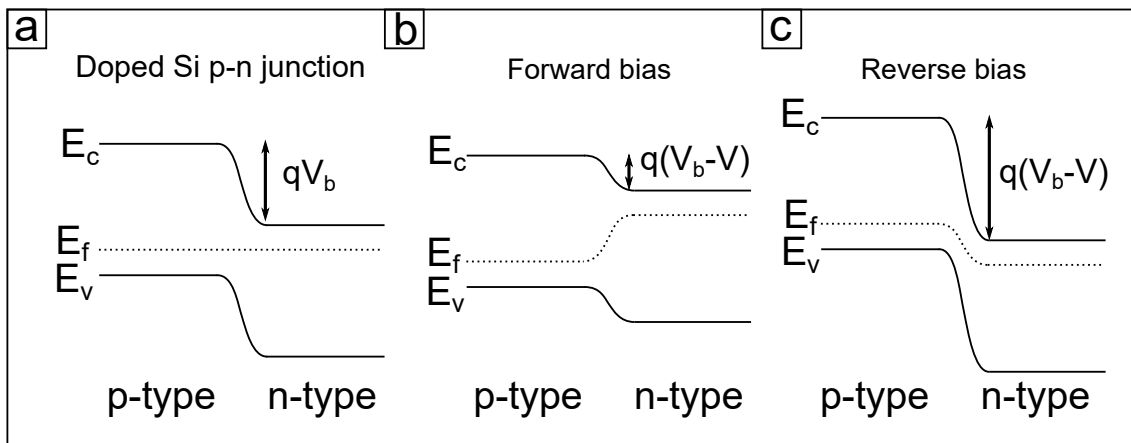
Figure 3.15: a) A doped Si, p–n junction in thermal equilibrium, the potential barrier across the depletion region is equivalent to qVb in height. b) The junction in forward bias, where a positive potential V is applied to the p–type material the potential barrier across the depletion region is reduced by qV. c) The junction in reverse bias i.e. applying a negative bias to the p–type material increases the depletion barrier by qV.

sub-unit an acceptor. The converse is true for electron donating groups, which increase the electron density of the attached sub-unit, making it an electron donor. In doing this we are effectively engineering the bandgap through the HOMO and LUMO levels. Design of molecular rectifiers typically incorporates a strong acceptor coupled to a strong donor via an unconjugated σ bridge (A–σ–D) which serves as a tunneling barrier between the two [81]. Designing molecules with only the bandgap in mind can be problematic as the chemistry of the overall molecule and its reactivity must still be considered. In a one electron picture using an overly strong acceptor can make oxidation a problem as oxidation potentials or ionisation potentials are both related to the energy of the HOMO energy level. Similarly, reduction potentials or electron affinities are related to the energy of the LUMO [85, 81]. Halogenation has been used in the past decade or two as a route to stabilise organic molecules by lowering both the highest occupied molecular orbital (HOMO) and the lowest unoccupied molecular orbital (LUMO) energy levels in the molecule [84]. Heavy fluorination of a molecule has been effectively used to change p-type molecules into

n-types as has been demonstrated for pentacene into perfluoropentacene [87, 88]. Progress has progressed rapidly in the past few decades with organic electronics now available in commercial available application such as organic light emitting diodes (OLEDs) and organic field effect transistors OFETs [65]. As a point of clarification, OTFTs operate by modulating the conduction of a channel at the interface between a dielectric and a semiconductor. Whilst OTFTs are in effect OFETs [89] not all OFETs are OTFTs. One yardstick by which organic transistors are measured is in terms of carrier mobility [90] and in this regard *p*-type organic thin-film transistors (OTFTs) have outpaced development of similarly efficient *n*-types [91, 85]. The role of molecular electronics in commercial application is currently limited to *molecular materials*, where devices exploit the macroscopic properties of molecular compounds. As such most OTFT and OFETs are schematically similar to their inorganic counter parts. In table 3.2 it is apparent that carrier mobilities in OFETs are orders of magnitude lower than what can be achieved with conventional inorganic compounds, such as Si and GaAs but not hydrogenated amorphous silicon (a-Si:H). In the past decade, a-Si:H has been the bench mark material for TFTs but has now been surpassed by OTFTs based on both small organic molecules (such as Pentacene and C_{60} in table 3.2) and conjugated polymers [36]. This development has seen the introduction of flexible OLED displays incorporating OTFTs to the market place. OTFTs fabricated using conjugated polymers have previously lagged behind small molecule systems but have seen carrier mobilities increased by a factor of 10^2 by increasing order through polymer alignment [37]. Results such as this illustrate the importance of studying ordering interactions to optimise charge transport.

Material	Mobility (cm2=Vs)
a-Si:H, hydrogenated amorphous Si (electrons) [92]	1
Si single crystal (electrons)	1500
GaAs single crystal (electrons)	1500
Region-regular polythiophene	0.47
Polyacetylene	10^{-4}
Phthalocyanine	10^{-4} to 10^{-2}
Thiophene oligomers	10^{-4} to 10^{-1}
Organometallic dmit complex	0.2
Pentacene	10^{-3} to 1
Bis[1]benzothieno[2,3-d;2' ,3'-d']naphtho[2,3-b;6,7-b']dithiophene	7
2,7-Dioctylbenzothienobenzothiophene	31
Regioregular poly[4-(4,4-dihexadecyl-4H-cyclopenta[1,2-b:5,4-b']dithiophen-2-yl)-alt -[1,2,5]thiadiazolo[3,4-c]pyridine]	24
C60	0.3
Graphene	2.5×10^5

Table 3.2: Room temperature OFET carrier mobilites in comparison to single cystal Si and GaAs adapted from [93] and based on the works of [94, 37, 95, 96, 97, 98, 99]

4

Experimental methods

4.1 Ultra high vacuum

Studying surfaces at the nanoscale often depends on the ability to obtain and maintain ultra high vacuum (UHV) conditions. UHV simplifies surface systems by isolating contaminants and other process than those of interest. Outside of UHV most surfaces will oxidise and adsorb impurities in a short time frame, preventing the investigation of anything but the most non-reactive systems. 10^{-10} mbar is considered to be the base working pressure for most UHV systems, with lower pressures preferable for more reactive samples and surfaces. Vacuum chambers are typically constructed from welded stainless steel due to its low outgassing and it doubling as a Faraday–cage, isolating beams and instruments from external fields as in figure 4.1. Modularity and access to these systems is provided by knife edge flange systems that typically use a sacrificial gasket to create a sufficiently air tight seal so that pressures below 10^{-10} mbar can be maintained. The knife edge flange system allows view ports and instruments to be fixed at regular intervals and is vital to the manipulation of samples and conducting experiments.

Figure 4.1: UHV chamber with a partially assembled bake out cage around it, situated in the nanophysics lab at UCLan.

4.1.1 Achieving UHV

As we approach UHV, gases behave differently at lower pressures. These behaviours are known as *flow regimes*. The turbulent flow regime applies to pressures higher than 10^{-2} mbar, and describes fluid motion, with each particle constantly interacting with those around it. In pressures lower than 10^{-3} mbar, the molecular flow regime begins, and the particles can be considered to travel ballistically with significantly fewer interactions. The average distance between each interaction can be quantified as the mean free path. This distance increases inversely proportional to the pressure in the chamber; a particle with a mean free path of 7 cm in 10^{-3} mbar will have a mean free path of 7 m in 10^{-5} mbar and so collisions with the chamber walls are far more significant than interactions with other particles in UHV. Different flow regimes require different pumping techniques. To obtain pressures of less than 10^{-10} mbar, two main types of pumps are used. Pumps that operate in the turbulent flow regime, in our case diaphragm pumps, reduce the pressure in the chamber down to 10^{-6} mbar with the aid of small turbo pumps. These assemblies are the roughing pump stage which removed the largest volume of gas from the chamber. Having achieved a rough vacuum, turbo-molecular pumps which operate in the molecular flow regime can be used to further reduce the pressure in the chamber and achieve UHV. Turbo molecular pumps operate as compressors, with the pump consisting of layered angled rotors and stators of increasing pitch. The rotors rotate so that the linear speed of the vanes is comparable to that of the ballistic speed of the gas molecules. Collisions with these rotors adds energy and changes the momentum of the gas molecules and the rotors are angled so as to direct molecules down through stator blades and into subsequent rotor stages of decreasing pitch angle. The compressed output of the turbo molecular pump must be backed by a roughing pump and in conjunction, a setup like this can achieve UHV pressures below 10^{-11} mbar. These pumping systems are typically complemented by non mechanical pumping systems which can sustain
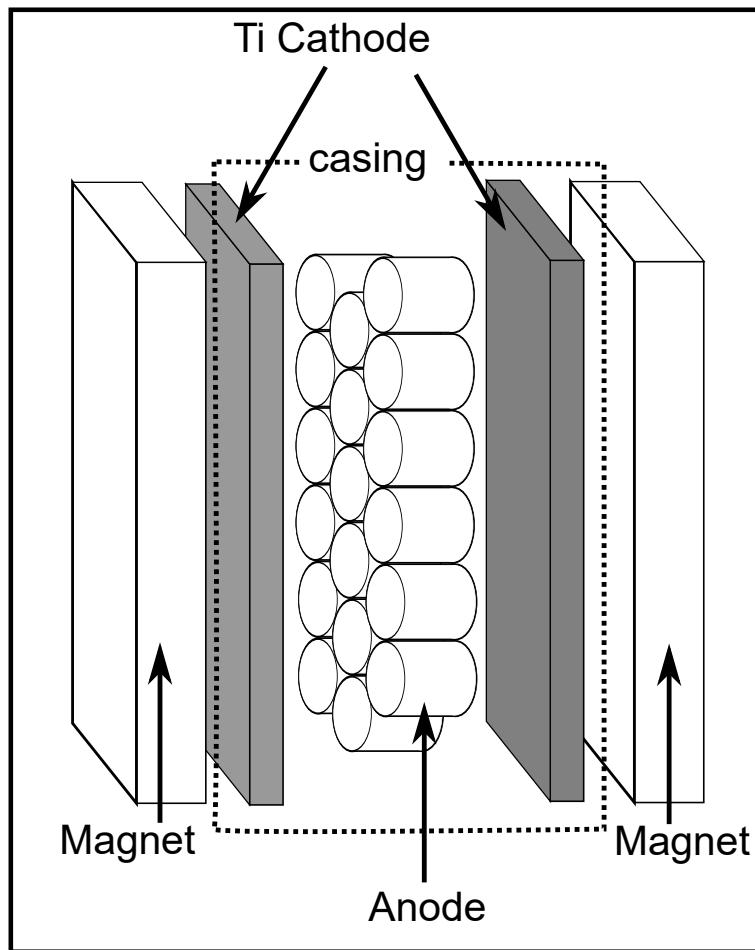
Figure 4.2: Schematic of diode ion pump where gas is ionised and trapped through sputtering in the reactive Ti cathodes

but not obtain UHV, without causing mechanical vibration. This is necessary for scanning tunnelling microscopy. These pumping techniques function through getter action, adhering gas molecules within the chamber to a binding surface. Examples are titanium sublimation and ion pumps. The latter is shown in figure 4.2 and ionises gas particles in the proximity of a high voltage anode. The anode is typically comprised of open cylinders, within which an electron cloud is contained by an externally applied magnetic field. The dense electron could contained within the anode volume ionises gas particles that are present. The ionised gas is then propelled by the strong potential field into the Ti cathode plates adjacent to the anodes. Ti is chosen as a plate material because its high reactivity traps the incident gas ions. Similarly Ti sublimation pumps sublimate a Ti filament coating the walls of the chamber of the Ti pump housing with reactive Ti vapour that binds incident gas atoms.

Bake out

To achieve UHV in a practical time frame a bakeout must be carried out. The porous surfaces within the vacuum chamber adsorbs gases and water vapour at ambient pressures and the slow out-gassing of these limits the ultimate pressure of the chamber to approximately 10^{-8} mbar. By baking the walls and contents of the chamber to 150 °C for typically 24 hours, the out-gassing rate of chamber components will be greatly reduced and upon cooling the vacuum will typically stabilise below 10^{-10} mbar.

The process of baking can be done through fibreglass heating tapes applied directly to the chamber or via erecting a bake out enclosure heating the air around the chamber to the desired temperature. Both approaches have merits and dangers, care should be taken throughout to ensure no hot spots occur and that heating is as even as possible across the chamber. In the case of heating tapes minimising

overlap and careful temperature gauging across the chamber is required. In the case of a fibre glass enclosure leaks should be patched and convection currents minimised by the inclusion of a high temperature safe fan to circulate the hot air about the vacuum chamber. Tin foil and aluminium tape are excellent patching tools for sealing awkward sections of the bake out enclosure. In both approaches a temperature regulator will be required with a thermocouple attached to the most temperature sensitive component of the chamber. The single temperature probe must be bolted securely in place for any overnight bake and the whole setup must be monitored on a first run to ensure no component of the bake fails due to heat stress for the full duration. An example of a common failure point in regards to this is Velcro adhesive if its used to seal panels. It is recommended to use mechanical clamps and fixings wherever possible to minimise this.

Due to the mixed material construction of a UHV chamber temperature gradients and rapid changes should be minimised particularly in close proximity to sensitive areas such as around view ports and ceramics. Uneven thermal expansion and contraction can cause stress fractures or otherwise compromise the vacuum. Protection of these requires draft insulation along side measures previously discussed with regards to hotspots. This is easily done by wrapping any exposed sections in tinfoil.

4.2   Sample and surface preparation

Before introduction to vacuum, single crystals must be polished and cleaned. This is normally done with increasingly fine grades of diamond paste, 6 μm, 1 μm and 0.25 μm is the progression we used. Following this the sample is preferably cleaned using methanol in a ultrasonic bath. After polishing and cleaning samples require mounting. Mounting solutions vary for different samples and UHV samples. The majority of studies carried out in this work involve samples mounted to Ta plates using Ta strapping or wire, spot welded secure, as in figure 4.3(a).
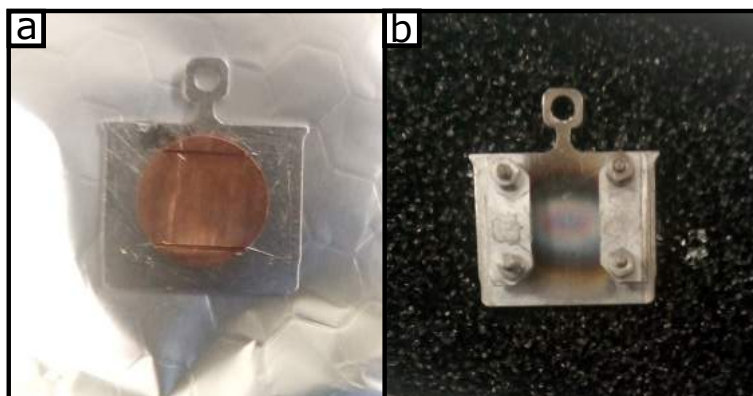
Figure 4.3: a)A Cu(111) crystal mounted on a Ta plate, mounted using spot welded Ta wire. b) Resistive heating mount, samples are held between the outer bands which serve as contacts and are insulated from the sample plate

Following introduction to vacuum, surface preparation of metal crystals to yield atomically flat terraces is sample dependent but will invariably involve a cycle of sputtering and subsequent annealing. Sputtering is a technique where by the sample is bombarded by high energy ions (approx. 1 KeV). Most typically this is done with a chemically inert source gas such as Ar^+ [100]. Atoms within the target sample are ionised and ejected from the surface by this process. The number of atoms removed per ion is the sputtering yield. This is dependent on angle of incidence, ion element and energy, and surface composition. For Cu under bombardment of Ar^+ at 1 KeV a sputter yield of approximately 3.35 [101] for a beam at normal incidence to the surface. This technique requires the substrate be conductive otherwise the target becomes charged and the technique is ineffective. During sputtering a drain current between the sample and a ground is measurable as the ionisation of surface atoms induces a current. This is typically of the order of a few μA. This technique can be used to ensure the sputter beam is incident to a sample within a chamber.

Sputtering is an effective technique for cleaning surface oxidation and contamination but leaves the surface rough and uneven. To correct this the sample is annealed by heating it to below its bulk melting point. The high temperature facilitates

energy minimisation reordering of atoms in the near surface region. This results in atomically flat surfaces often up to 1 μm in length. The methods of heating a substrate vary depending on the temperatures required and sample properties. The most common form is known as indirect heating which typically uses radiative heat from a filament mounted behind the sample plate. This can be effective for anneal temperatures up to approximately 600°C dependent on sample mounting. For extremely high temperatures, e-beam heating is used. In hot cathode techniques, electrons are generated by thermionic emission of a heated element. These are then projected onto to the sample surface via the application of a large positive bias, typically several kV. This technique is used for high temperature applications, such as when needing to heat samples beyond 1000°C.

4.3   Molecular beam epitaxy

One of the earliest and most common forms of film growth techniques is chemical vapour deposition (CVD). This is used extensively for inorganic semiconductor development and production. CVD is most simply described as introducing a gas flow into a chamber containing a heated substrate [102]. Molecular beam epitaxy (MBE) in comparison, is a low pressure process in which a molecular source is evaporated into the chamber through a tight beam focused on the sample. The amount of material made available for adsorption can be very easily controlled through this approach.

The molecular flux and rate of evaporation is controlled by the source temperature [100] and, by shuttering the beam, doses can be controlled very precisely. Monolayer deposition times can be stretched from a couple of seconds [100] to several minutes making this approach ideal for investigating variable coverage and layer growth. Multiple sources can be alternated or simultaneously used for investigation of more complex multicomponent systems. Molecular sources are typically housed in
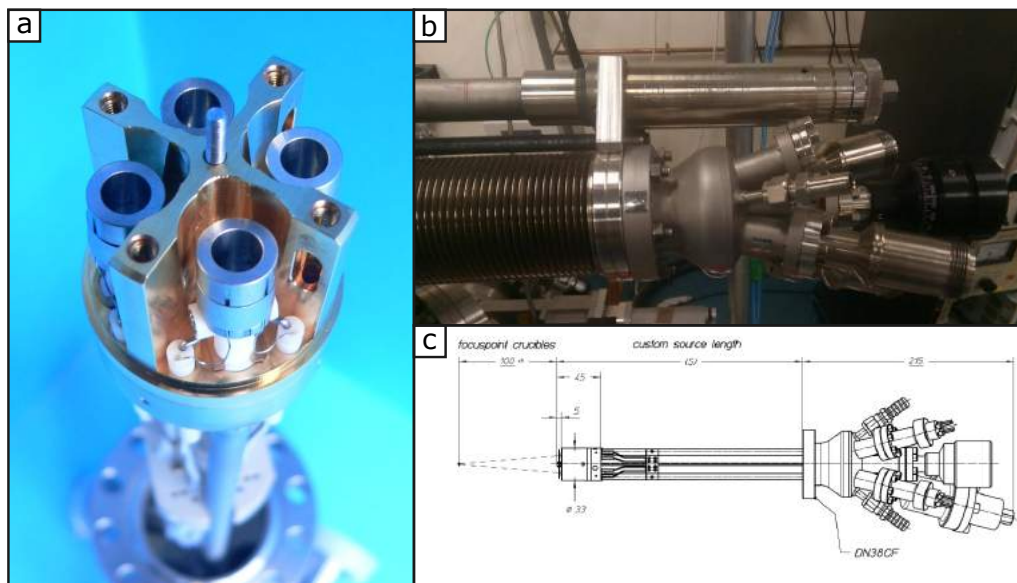
Figure 4.4: a) Dodecon 4 cell OMBE system with the collimating shroud removed to reveal the crucibles. b)The Dodecon system mounted to a chamber via bellows for sample separation control. c) Schematic view of the OMBE system in its entirety.

ceramic or alumina crucibles within electrically heated Knudsen cells shown in figure 4.4(a), prior to operation they are out-gassed by heating to deposition temperature. By monitoring chamber pressure a spike should be observed before decreasing to a new lower base pressure. The spike corresponds to the desorption and out-gassing of source contaminants where the elevated base pressure reflects the evaporation of the source material. Once the outgassing pressure spike has plateaued at the deposition pressure, the source is ready for use. Multi-cell evaporators have a focus point for their crucibles to ensure that the center axis of the molecular beams are aligned and intersect at the same point in space during deposition. In the case of the Dodecon model this focus point is located 10 cm away from the source as seen in figure 4.4(c). Positioning of the sample at this focus point can be achieved relatively easy through the use of adjustable bellows at the interface to the chamber as shown in figure 4.4(b).

4.4 Low energy electron diffraction

Waves incident on an object produce a pattern through interference of the scattered waves that is characteristic of the diffracting object [100].Diffraction is most effective when features of a target object are of a comparable size to the wavelength of the incident wave. Low energy electron diffraction (LEED) exploits this phenomenon, scattering electrons off the atomic lattice of a surface to determine its structure is the oldest technique used for this purpose [47]. Using the Bragg condition we can illustrate the suitability of electrons to this task:

$$2D \sin \theta = n\lambda$$

where: d is the plane spacing within the crystal, θ is the angle of incident from the crystal plane and n is any integer, we can see through substitution that using electron beam energies between 0 and 1000 eV will produce electrons with a wavelength between 2.74 Å and 0.388 Å making it an effective tool for studying atoms through to molecular length scales. [3].

LEED is a highly surface sensitive technique, at a typical energy of 100 eV the majority of electrons penetrate less than 1 nm before undergoing a scattering interaction [103]. The mechanism limiting and the source of most inelastic losses is plasmon excitation [47]. A large number of electrons incident upon a surface are scattered inelastically and often repeatedly, where only those that undergo a single elastic collision can convey the surface structure [3]. To this end in designing the LEED optic, special consideration is made to filtering out inelastic electrons.

The LEED optic, shown in figure 4.5 is comprised of 3 parts; an energy tunable electron gun, a phosphor screen to illuminate the diffracted electrons scattered normal to the surface and lastly an array of mesh screens to both accelerate elastically scattered electrons into the phosphor screen whilst suppressing electrons that have
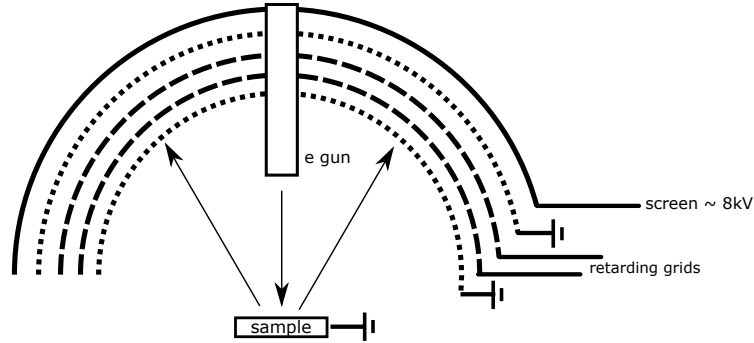
Figure 4.5: The LEED optic is comprised of 5 screens, the phosphor screen maintained at a high, accelerating voltage, two field isolating grids at ground and between these an electron filter comprised of two grids at potentials just below the emitted electron energy to repel any inelastically scattered electrons from the optic.

undergone energy loss through inelastic or multi-scattering processes [3, 2].

The criterion for constructive interference, which results in the characteristic spots in a LEED pattern, is that the path difference between scattered electrons is equal to to an integral number of wavelengths, $n\lambda$. In the case of electrons, λ is the de Broglie wavelength of the electron, which is dependent on the electrons kinetic energy (KE). For a one dimensional lattice, instances of $n\lambda$ are related to the scattering angle of $\sin \theta_a$ and to the atomic separation of the lattice, a as follows:

$$\sin \theta_a = \frac{n\lambda}{a}$$

From this we see that for electrons of a set KE, incident on a fixed lattice, diffracted beams will only exist at particular angles [3].

The magnitude of the incident electron wave vector (k_0) is defined as:

$$|\mathbf{k}_0| = \frac{2\pi}{\lambda}$$

$|\mathbf{k}_0|$ is a measure of the electron's momentum (mv), demonstrated by incorporating

the de Broglie relationship,

$$\lambda = \frac{h}{mv}$$

as follows:

$$|\mathbf{k}_0| = \frac{2\pi}{a}(mv)$$

Rearranging the definition of $|\mathbf{k}_0|$ for λ and substituting it into the criteria for constructive interference we obtain:

$$|\mathbf{k}_0| \sin \theta_a = \left(\frac{2\pi}{a}\right) n$$

The component of momentum parallel to the surface of the incident electron $|\mathbf{k}^{\parallel}| = |\mathbf{k}_0| \sin \theta_a$, (just as the perpendicular component, $|\mathbf{k}^{\perp}| = |\mathbf{k}_0| \cos \theta_a$ [2]) and so parallel momentum exchanged with the surface is quantised into units of $\frac{2\pi}{a}$, which is also the magnitude of the reciprocal lattice vector [3]. It is this relationship that demonstrates most clearly that the diffraction pattern of the surface corresponds to that of the reciprocal lattice of the system. Up to this point we have only considered a 1d lattice or chain of atoms, for diffraction off a 2d surface a second condition must be introduced for this additional dimension where a periodic lattice now extends with lattice spacing b and so it follows in this dimension that:

$$|\mathbf{k}_0| \sin \theta_b = \left(\frac{2\pi}{b}\right) m$$

where m is any integer. For diffraction spots to occur these conditions constraining the parallel momentum component of k_0 must be met simultaneously in both dimensions, i.e. spots will appear in the pattern where the "beams" produced by diffraction in each dimension, intersect. The exchange of parallel momentum is in effect restricted to the 2D reciprocal lattice vector $\mathbf{G}$ where

$$\mathbf{G} = n\frac{2\pi}{a} + m\frac{2\pi}{b} = \Delta\mathbf{k}^{\parallel}$$

58

In this $\Delta\mathbf{k}^{\parallel}$ represents the change in parallel momentum for an incident $\mathbf{k}_0$ and scattered $\mathbf{k}_s$ electron wave vectors [3]. This can be written as the Laue condition [32],

$$\Delta\mathbf{k}^{\parallel} = \mathbf{k}_0 - \mathbf{k}_s = \mathbf{G}$$

The Ewald sphere (which becomes a circle for 1 and 2 dimensional systems) is a convenient way to visualise the Laue condition, presented in figure 4.6. A sphere of radius $|\mathbf{k}_0|$ is drawn centered on the point of incidence of $\mathbf{k}_0$ on the surface. Diffraction spots coincide with locations the reciprocal lattice rods (extending out from the plane of the surface) intersect with the sphere. The points of intersection indicate the path of $\mathbf{k}_s$ with respect to the origin of the sphere, and the scattering angle θ. As such, this construct can be useful in determining the visible diffraction pattern at a given electron KE [3, 2].

The incident electron beam energy is proportional to the radius size of the Ewald sphere and inversely proportional to the scattering angle. At low energies we resolve higher order and larger periodic structures as fewer spots are incident but as we increase the energy the Ewald sphere expands and the system becomes sensitive to smaller real space structures.

LEED patterns can be analysed to determine the real space structure of the surface for a well calibrated optic. More commonly however patterns are analysed with reference to a known system. In the context of molecular adsorption studies this is normally provided by the substrate atop which the system is being characterised. Figure 4.7 shows examples of the real space structure and resulting diffraction pattern obtained for a substrate and overlayer system. To determine the real space lattice of an overlayer structure we mustfirst define its reciprocal unit cell vectors $\mathbf{a}_o^*$ and $\mathbf{b}_o^*$ in terms of the substrate reciprocal unit cell vectors, $\mathbf{a}_s^*$ and $\mathbf{b}_s^*$ as follows [2, 3]:
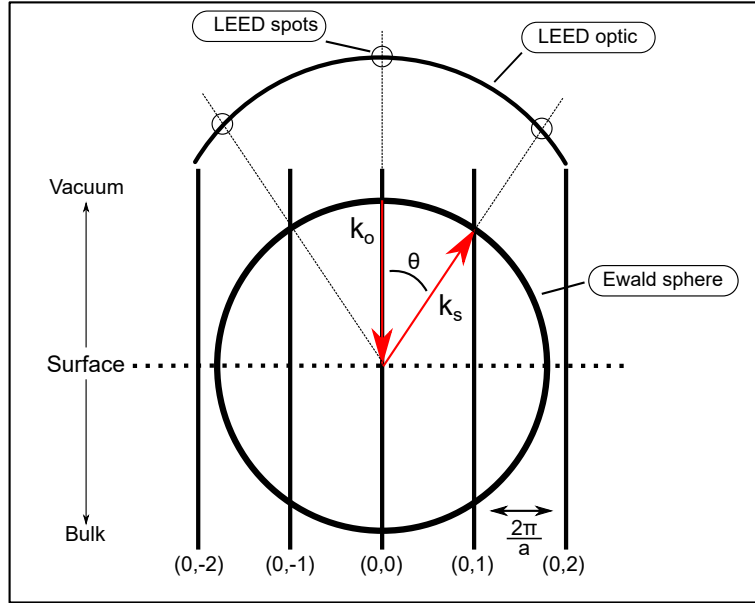
Figure 4.6: The Ewald sphere construct, shown for a specific surface direction, with electrons incident normal to the surface, illustrating the Laue condition. Diffraction spots occur for reciprocal lattice rods bisected by the sphere of radius $|\mathbf{k}_0|$. After scattering at angle θ, $\mathbf{k}_s$ passes through the sphere–rod interception and will be visible upon a LEED screen. Adapted from [3].
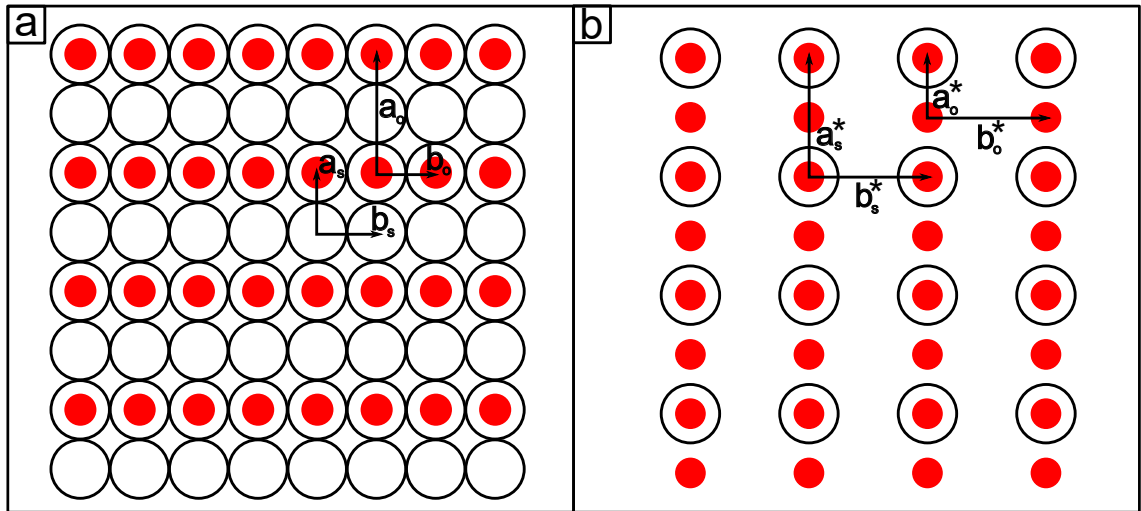
Figure 4.7: a) The real space structure of a square atomic lattice represented by white circles and described by $\mathbf{a}_s$ and $\mathbf{b}_s$, with an overlayer structure of red circles described by $\mathbf{a}_o$ and $\mathbf{b}_o$. b) The corresponding reciprocal lattices for the same system, described by $\mathbf{a}_s^*$ and $\mathbf{b}_s^*$ for the substrate and $\mathbf{a}_o^*$ and $\mathbf{b}_o^*$ for the overlayer.

$$\mathbf{a}_o^* = G_{11}\mathbf{a}_s^* + G_{12}\mathbf{b}_s^*$$

$$\mathbf{b}_o^* = G_{21}\mathbf{a}_s^* + G_{22}\mathbf{b}_s^*$$

Determining the reciprocal lattice vectors can be difficult for patterns comprising multiple overlayer structures or domains. Having done this however it is possible to assemble the reciprocal lattice matrix G,

$$\mathbf{G} = \begin{bmatrix} G_{11} & G_{12} \\ G_{21} & G_{22} \end{bmatrix}$$

which is related to the real space lattice matrix R by:

$$\mathbf{R} = \frac{1}{\det\mathbf{G}} \begin{bmatrix} G_{22} & -G_{21} \\ -G_{12} & G_{11} \end{bmatrix},$$

where

$$\det\mathbf{G} = (G_{22} \cdot G_{11}) - (G_{21} \cdot G_{11}).$$

The real space lattice vectors $\mathbf{a}_o$, and $\mathbf{b}_o$ for the overlayer are then related those of the substrate, $\mathbf{a}_s$ and $\mathbf{b}_s$ by:

$$\begin{pmatrix} \mathbf{a}_o \\ \mathbf{b}_o \end{pmatrix} = \mathbf{G} \begin{pmatrix} \mathbf{a}_s \\ \mathbf{b}_s \end{pmatrix}$$

Besides directly determining surface structures, LEED is frequently used to qualitatively compare ordering at the surface. Sharp LEED spots are indicative of a high order quality at the length scale concerned [2].

4.5 Scanning tunnelling microscopy

4.5.1 STM and its principles of operation

Scanning tunnelling microscopy was invented in 1982 by Gerd Binnig and Heinrich Rohrer [3]. The technique is non–contact and non–destructive, yielding a two–dimensional plot, a convolution of the local density of states (LDOS) of a surface and of the conducting tip used as a probe. For many samples, when using a fine enough tip, this can be considered equivalent to a topographical map of the surface. From this map, the coordinates of the atoms forming the surface can be determined. A schematic illustrating the key components of an STM is shown in figure 4.8. The tip, used to probed the surface, is normally separated from the surface by a small vacuum gap and will be the assumed state here on, but operation in atmosphere or in liquids is also possible. The method of operation relies on the principle of quantum tunnelling whereby electrons (within the sample for the case of a positive tip bias) are able to tunnel through the potential barrier imposed by the vacuum, bypassing the work function ϕ of the sample that otherwise ties them there, into the tip [44]. This flow of electrons provides a small but measurable current I_t.

In figure 4.9(a), initially the sample and tip are separated and non interacting, their vacuum level E_{vac} is the same for both. The vacuum level being the energy level beyond which an electron is liberated from the surface.

In figure 4.9(b) the tip and sample are brought to within a small separation, the tunnelling gap, d where tunnelling can occur. Both tip and sample enter a state of thermodynamic equilibrium where their Fermi levels, E_f are equal. Tunnelling is possible for small values of d as the wavefunction, ψ of an electron whilst periodic within the solid, decays exponentially as it extends out into the vacuum, with the following relationship:

$$\psi = Ae^{-2\sqrt{2m(\phi-E)}\frac{d}{\hbar}}$$
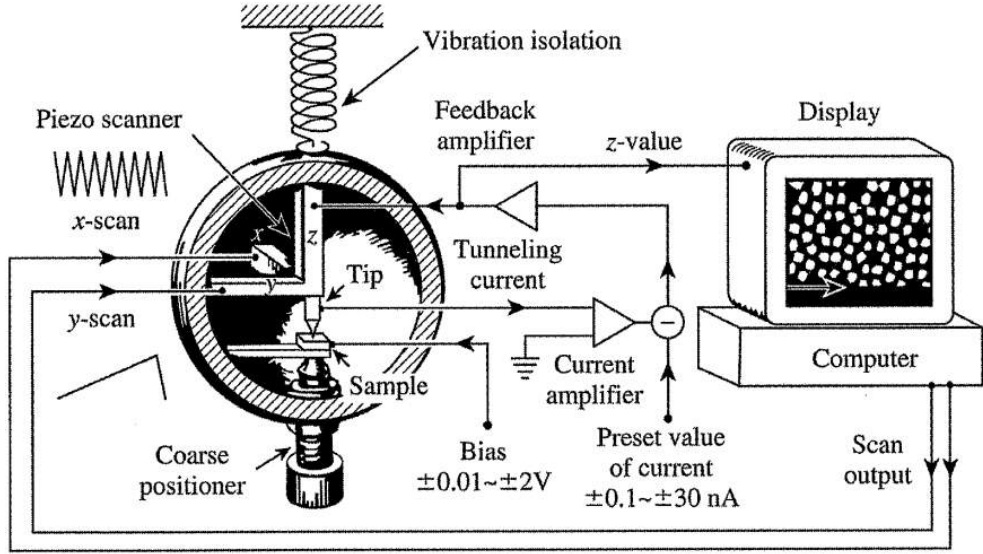
Figure 4.8: Schematic depiction of an STM reproduced from [10].

where m is the electron mass and E is the electron energy measured with respect to E_f [11]. The work function ϕ is defined as the energy taken to raise an electron in a material from E_f to the E_{vac} [104]. The work function is ϕ_S for the sample, and ϕ_T for the tip.

This is often written in terms of k, the inverse decay length, where:

$$k = \hbar^{-1}\sqrt{2m(\phi - E)}$$

and so

$$\psi = Ae^{-2kd}$$

In figure 4.9(c), we see that by applying a positive bias at V_B to the sample, we shift the energy levels in the sample by eV_B [12]. This facilitates tunnelling between the occupied states in the tip into the unoccupied states in the sample. By applying a negative bias to the sample we reverse this process, as shown in figure 4.9(d). The negative bias effectively raises the energy levels of the sample
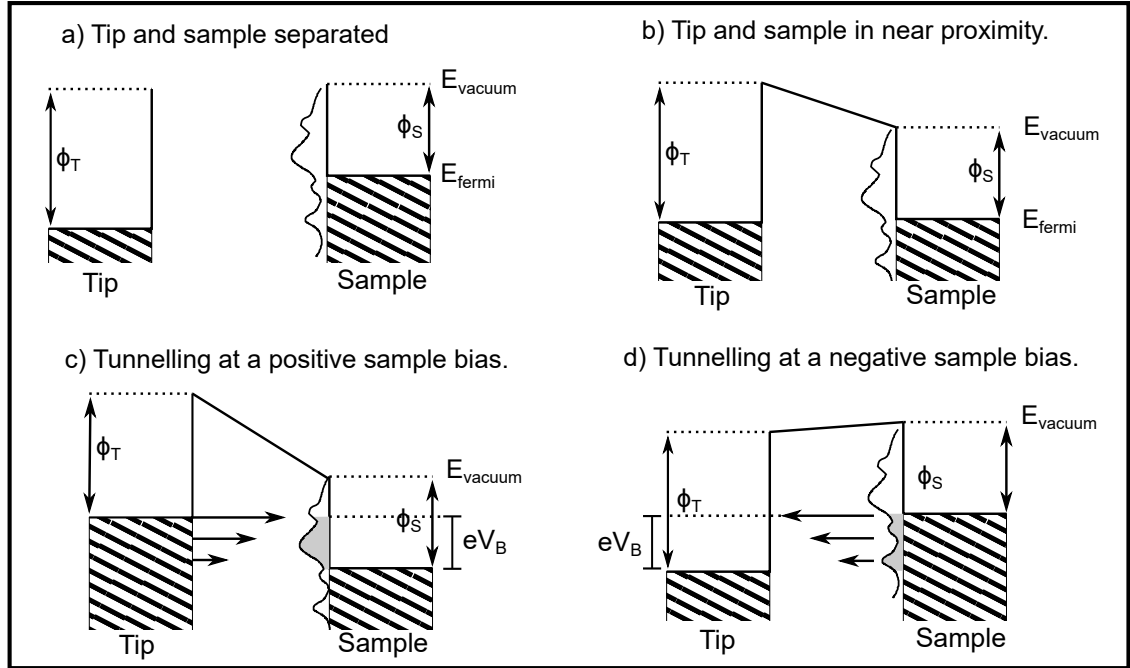
Figure 4.9: The energy landscape at a tip–sample tunnelling junction. In this schematic the tip density of states is assumed to be approximately constant but those of the sample vary as a function of E indicated by the plot to the left of the sample band diagram. a) With the tip and sample separated, b) with them separated by a small distance, the tunnelling gap d. c) With a positive sample bias applied. d) With a negative sample bias applied. Modified with reference to both [11, 12].

with respect to the E_f of the tip, and so electrons tunnel from the occupied states of the sample into the unoccupied states of the tip. By studying the equation for k, it becomes apparent that electrons with a higher energy state within the bias window, (the shaded region of the DOS spectrum in figures 4.9(c) and (d)) have a greater probability of tunneling through the vacuum barrier and so contribute more significantly to I_t under any applied V_B.

Whilst the probability of an electron tunnelling, and with it, the tunneling current I_t is dependent on d, it is also reliant on the energy dependent **density** of states, $\rho(\epsilon)$ in both the sample, ρ_s, and the tip, ρ_t for an applied V_B. In the Tersoff–Hamann approximation [105], the tip is assumed to be a spherical potential well and that the majority of tunneling occurs through the tip apex. If ρ_t is assumed to be

flat and continuous (as is true at low temperatures and biases (a few hundred mV) for W and PtIr tips), then I_t can be expressed in terms of the LDOS as follows [12]:

$$I_t \propto e^{-2kd} \int_0^{V_B} \rho_s(E_f + \epsilon)d\epsilon.$$

This approximation of I_t demonstrates its exponential dependence on d which affords STM its sensitivity when mapping surfaces.

Precise tip control and movement is achieved through the expansion / contraction of piezoceramics. This can facilitate surface mapping in the x, y and z axis of the surface to sub atomic precision with a sensitivity on the order of 2 Å/V [106]. Scanning is typically carried out across the surface through a raster pattern as illustrated in figure 4.10.

STM operates in one of two modes, constant d or constant I_t [3]. Constant d is the lesser used of the two modes and is only suitable for the flattest of substrates such as HOPG which are unlikely to have terraces or other significant features in the z-axis. For surface of any significant corrugation this mode of operation introduces the risk of crashing the tip. for small d values a large I_t response can result in strong substrate–tip interactions, disturbing and potentially resulting in material exchange between the two. For large d values I_t drops off exponentially restricting the surface detection window to within a few Å.

In constant I_t mode the tip height is changed during the scan so that I_t tracks a fixed value known as the set-point, I_s. This is achieved via a feedback loop which retracts and extends the tip in response to being above or below I_s. Both the tip position d and the tunnelling current I_t are recorded during this mode of operation, with the recorded current being akin to the differential of the path the tip travels, examples of these are presented in figure 4.11. The error signal in constant I_s mode is $I_t - I_s$ and so if the surface is approaching the tip then I_t increases beyond I_s with a magnitude proportional to the rate of change of tip–surface separation, i.e
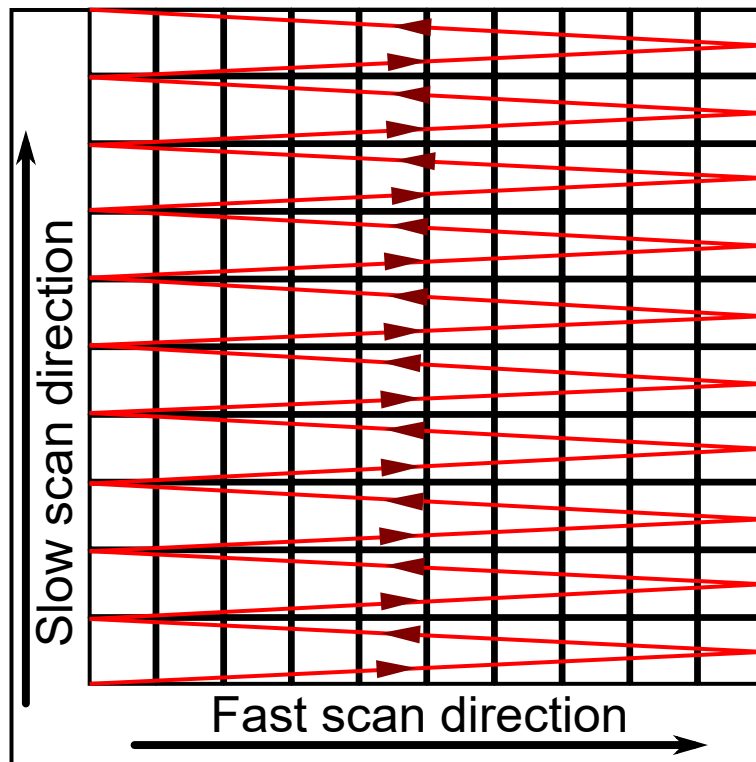
Figure 4.10: The rastering motion of the tip in conventional operation. An approximation of the tip path is shown in red, the tip scans backward and forward collecting a separate channel in each direction as it passes through each pixel of the grid. This method of operation introduces a fast and slow scan direction, with that latter being more susceptible to thermal drift.
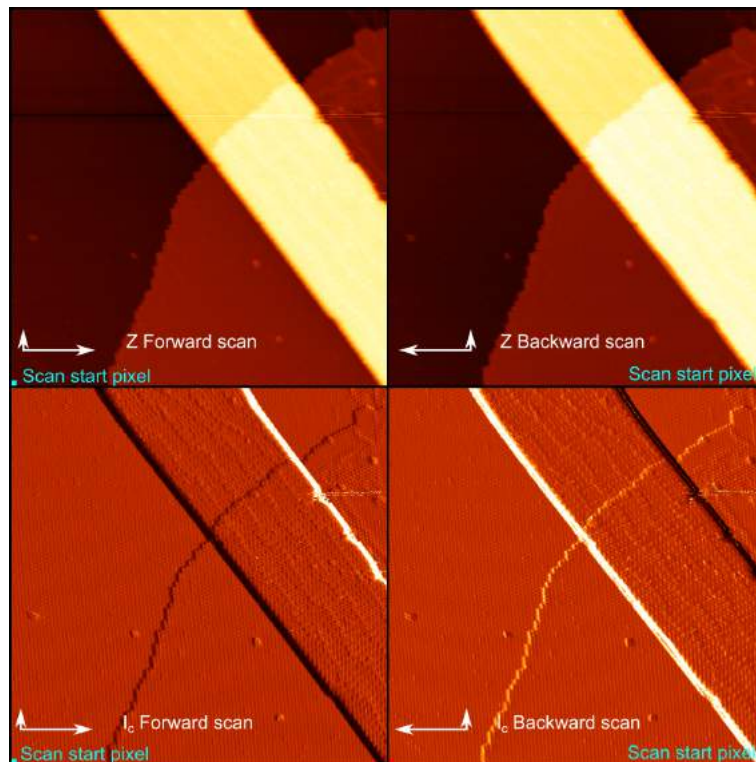
Figure 4.11: The I_t and Z channel data for a single image for both forward and backward scans is presented. The scanning directions are marked on each. Forward and backwards refers to the motion of the fast scan axes which corresponds to the large arrow. a) the forward Z scan. b) the backward z scan. c) the forward I_t channel. d) the backward I_t channel.
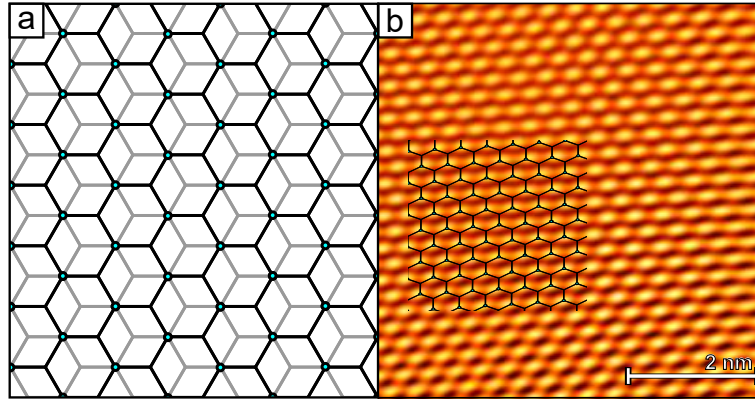
Figure 4.12: A small section of the HOPG surface, a sites will appear higher than b sites due to the greater electron availability arising from the underlayer dislocation

$I_s \propto \frac{\delta d}{\delta t}$. This assumes a constant density of states across the surface. Considering both forward and backward scans of an image, as presented in figure 4.11, can be important as tip asymmetry can result in different appearances of surface structures.

4.5.2 STM limits and convolution

In this section we discuss some of the limits of STM as a technique and some obstacles that must be considered. The nature of I_t, the recorded "topography", is a convolution of the physical geometry and the near surface chemistry and bond structure [3] due to the influence these have on the local density of states. This is demonstrated in figure 4.12(a) and (b) where alternating sites in the HOPG lattice appear brighter and darker due to the underlayer dislocation.

The image obtained via STM is not dependent on the surface geometry alone, the tip ideally a single point, in reality has a geometry of its own that impacts the scan. The resolving limit is dependent on the curvature of the tip in the most simplest of cases. Any asperities on the surface smaller than the tip will in effect map the tip topography centred on their location. This can result in a potato-print motif repeated across the surface image. An example of a double tip interaction at a step edge is presented in figure 4.13(a).

Adsorbate or impurity atoms or molecules may be picked up by the tip as it travels over the surface; this may have the effect of either improving the scan or worsening it. If the scan suffers from a multiple or asymmetric tip, or contamination by impurities, nano-structuring of the tip using high voltage pulses (15 nA, 10 V) is known to often improve the sharpness. Investigating molecular systems creates its own set of challenges, particularly in the case of physisorbed molecules. Tip–molecule interactions can result in molecules adsorbing to the tip. Increasing d and reducing I_t reduces the probability of this in most cases. This can be achieved simultaneously by reducing I_s. An adsorbed molecule can actually improve the apparent resolution of an STM image. This can create misleading features due to motion of the molecule and the convolution of its own LDOS to the image. An example of this is provided in figure 4.13(b). Attempting to condition the tip via voltage pulses can be detrimental on loosely bound molecule systems, often making a situation worse by adsorbing many more molecules. In these instances it can be beneficial to apply high voltage pulses in a clean portion of, or entirely different sample.
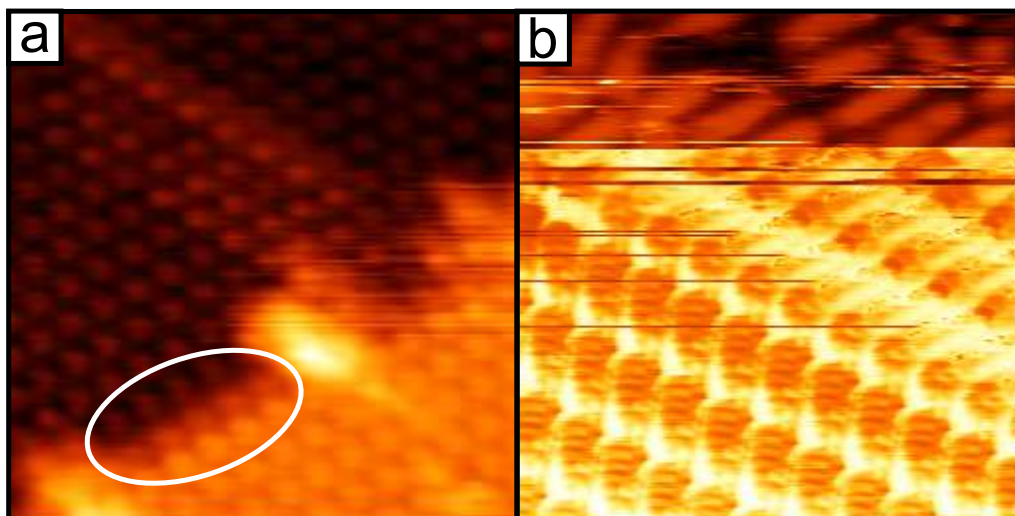
Figure 4.13: a) A second diminished step edge is evident as a double tip approaches a C_{60}/Cu(111) terrace. b) The diffuse molecules at the top of the image appear to have complex features in the latter half following the adsorption of a molecule to the tip through convolution of the adsorbed molecules LDOS with that of the substrate molecules.

4.6 Density functional theory

No work performed as part of this thesis involved carrying out Density functional theory (DFT) calculations, but the results of models and calculations performed by collaborators have been incorporated in the analysis of some systems and so an overview is provided. DFT is a quantum mechanical modelling system practical to studying atomic and molecular systems. Takao Tsuneda writes: "*The basic concept of DFT is to make it possible to perform high-speed calculations of many-electron systems by representing the potential as the functional, not of the orbitals but of the electron density*" [107]. Electron interactions define the structure and behaviour of matter across molecules, surfaces and the bulk. To describe a system of interacting electrons DFT considers only the 3 dimensional (spatially x,y,z) property: electron density [108]. This avoids having to consider the wavefunction of the system which is 3N dimensional and dependent on the co–ordinates of the electrons in the system. From knowledge of the electron density distribution alone and by using certain

approximations it is possible to determine the ground state of a system and its total energy [109]. The energy is therefore a function of the density function i.e a density functional [110]. Whilst DFT allows us to avoid the exponential scaling of possible configurations that comes with modeling the interactions of N overlapping electron wave functions, it still scales linearly with the number of particles. Systems with large unit cells or many atoms can still be prohibitive to study through DFT.

5

Coronene on Ag(100)

5.1 Abstract

We present new information on the coronene (Cn)/Ag(100) system, providing LEED data collected at 90 K and RT (room temperature) along side RT STM. We determine the Cn monolayers relationship with the substrate via LEED and find two Cn structures exist at 90K, a primary commensurate structure SS A, the same as that previously reported at RT, and a less favourable, looser packed commensurate structure rotated 45° to it, SS B. We see that both SS A and SS B are present at 90 K and RT and exist as monolayer domains.

5.2 Introduction

5.2.1 Coronene

Coronene (Cn) shown in figure 5.1, is a polycyclic aromatic hydrocarbon (PAH) [111]. Cn, like many other PAHs can be considered a small hydrogenated graphene platelet. Depositing coronene molecules at temperatures sufficient to facilitate dehydrogenation on close packed, reactive surfaces such as Cu, Rh and Pt, has been
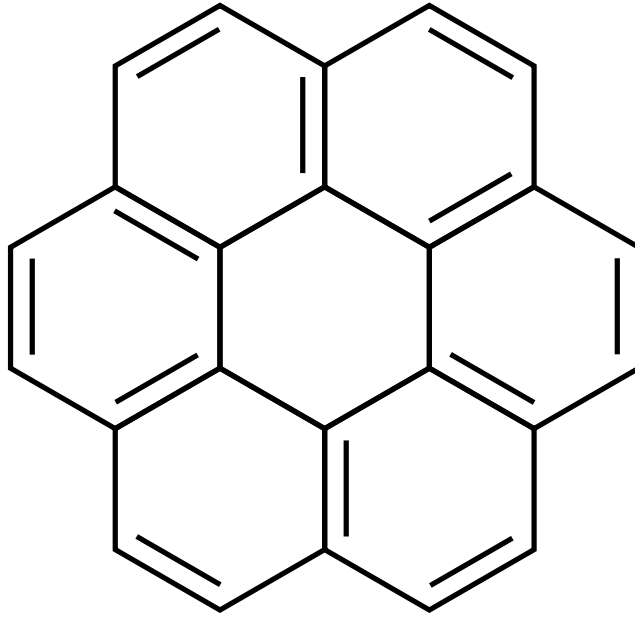
Figure 5.1: Schematic illustration of coronene.

shown to be an effective technique for low-defect graphene growth [112, 113]. One barrier to this approach is the high temperatures required to induce dehydrogenation. Studies have found Cn/Cu(111) to be one of the lowest temperature systems for which graphene has been synthesised using this approach but still requires a temperature in excess of 550° [113]. Cn atop relatively inert substrate such as Au and Ag [75] exhibiting a repulsive molecule–molecule interaction which means it forms islands and closed packing only under high coverages. This conforms to the 2D gas behaviour described in section 3.2.5. Cn is an interesting material for the purposes of studying molecular ordering as its lattice parameters can be tailored directly through surface coverage [75, 13]. Control of this is a powerful tool as the lattice dictates the adsorption site of a molecule which can greatly alter its electronic properties. A dramatic case illustrating this, for a similarly aromatic molecule, is the adsorption dependent conformation changes seen with Br_4TPP / Cu(111) that in turn lead to large changes in the DOS spectrum [114].

5.2.2 Coronene/Ag(110)

Cn was first seen to form two superstructures on the Ag(110) surface in the work of C. Seidel *et. al* [75]. In this work they characterise the Cn superstructure and its dependence on surface coverage using LEED. For low, sub-monolayer Cn coverage a diffuse ring appears in the pattern relating to the 2D gas type behaviour discussed in section 3.2.5. The ring feature is a product of the Cn domain alignment being independent of the crystallographic axes of the substrate at lower coverage. As a result of this, the domains of Cn form independent to the NN (nearest neighbour) axes of substrate. This rotational disorder between domains manifests as rings, as opposed to discrete spots corresponding to consistent NN directions, in the LEED pattern. As the molecular density increases the average spacing reduces and the molecules are constrained, reducing freedom for variation in the intermolecular separation. This produces a clearer ring about the halo in the LEED pattern [75]. As the surface tends towards a full monolayer, the tight Cn packing suppresses the 2D gas behaviour and the substrates influence upon the overlayer ordering is apparent with the ring giving way to discrete spots corresponding to 3 different superstructures at the surface [75]. Two 3–fold domains are present for structure 1; a single domain direction exists for Structure 2, which is overall tighter packed and aligned with the (100) direction. Structure 2 has two different forms, lying commensurate and coincident with the substrate via the following relationships:

$$S2_{commensurate} = \begin{bmatrix} 4 & 0 \\ 2 & 3 \end{bmatrix} \text{ and } S2_{coincident} = \begin{bmatrix} 4 & 0 \\ 2 & 2.5 \end{bmatrix}$$

The coincident structure arises from tighter compression as coverage tends towards 1 ML [75].

A subsequent study through LEED, STM and DFT calculations [13] showed that the population ratios of S1 and S2 coronene ordering depend on the temperature of
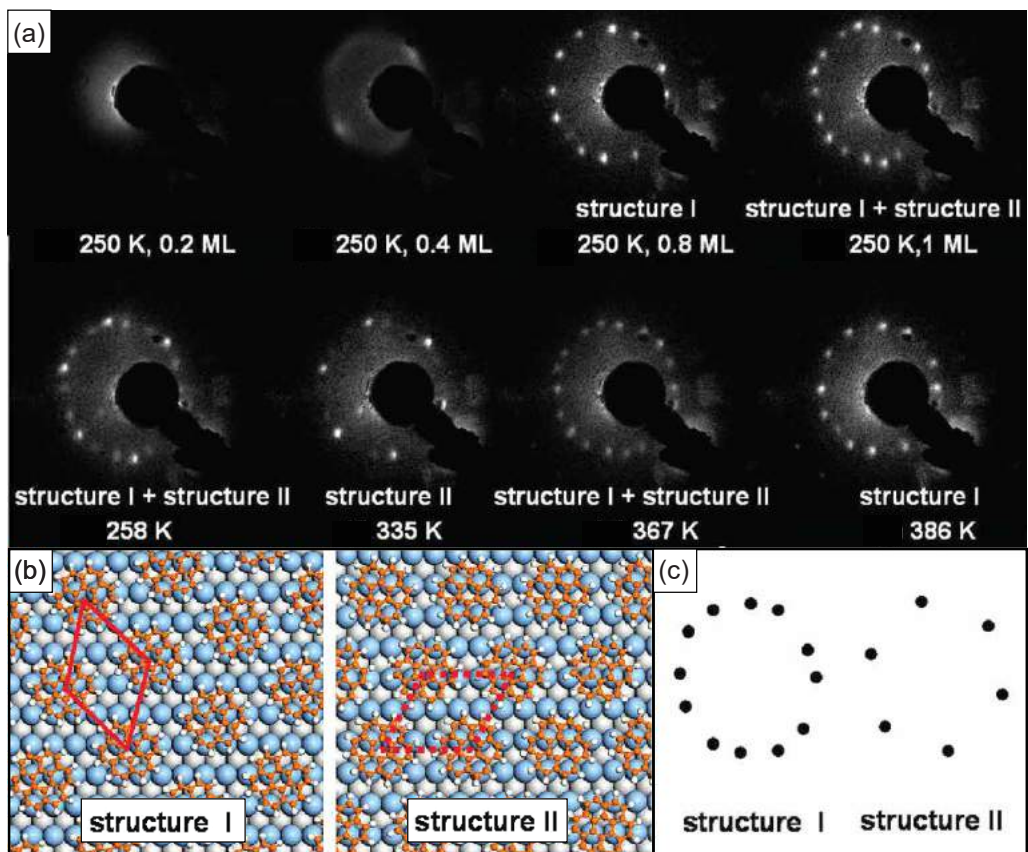
Figure 5.2: a) LEED patterns of the Cn/Ag(110) system as a function of coverage and temperature identifying the presence of two overlayer structures. b) schematic model of S1 and S2. c) LEED patterns relating to S1 and S2. All images are adapted from [13].

the surface. By tailoring these it is possible to exclude one or the other as in figure 5.2(a). This latter study does not identify the coverage dependent S1 subforms reported by Seidel *et. al* however. Overall it appears the S1 structure, the sparser of the two, is most favourable at low temperature and coverage but both systems exist at the surface at 1 ML and room temperature. Annealing prompts a transition to S2 at 335 K and further annealing to around 367 K reverses this as coronene desorption reduces coverage and coronene–coronene repulsion begins to facilitate the coexistence of S1 and S2 once more.

5.2.3 Coronene/Ag(100)

A study has been published looking at the Cn/Ag(100) system using density functional theory (DFT), Low temperature (LT) STM and room temperature (RT) LEED [14]. This combination of techniques and temperatures complements the data obtained for our system, which is STM at RT and LEED at 90 K. In this the Cn/Ag(100) system was looked at varying coverage, between 0.6 and 1 ML. Another experimental difference is their deposition method. Specifically they calculated the deposition time for a monolayer of Cn based on a constant Cn flux from their source. We made the assumption that the system self–passivates at ML coverage. This assumption was informed by observations across several depositions and characterisation attempts. Using the same deposition parameters we observed a complete layer each time with no direct evidence through STM of partial monolayer or multilayer formation. Some variance in the deposition rate would be expected and so this result suggests an external factor is enforcing a full layer i.e. that the monolayer prevents further Cn adsorption at low deposition rates at RT. Prolonged LEED at higher beam energies appeared to desorb Cn, indicating it is weakly adsorbed to the surface. Further discussion on the Cn coverage for our data is provided in section 5.4.4. It is possible to grow crystalline Cn atop metal crystals [115], but

there are no studies directly addressing coverages between ML and bulk studies of Cn atop single metal crystals. One study that is relevant is the work of Huempfner *et al.* [14] where they suggest it is possible to deposit additional Cn beyond the ML on Ag(111). They report dosing an Ag(111) surface with a 1.5 ML equivalent of Cn and observing reduced sharpness of LEED spots indicative of disordered adsorption.

After heating this system Huempfner *et al.* [14] report that the quality of Cn ordering at the surface increases as indicated by sharper LEED spots. They conclude that a partially adsorbed second layer either desorbs or forms molecular clusters. The disordered second layer Clustering would increase the apparent order by occluding less of the ordered monolayer. Further heating reduces the order of the Cn indicating the beginning of monolayer desorption.

The reported LEED patterns have been calibrated to remove the effects of spherical aberration and other screen deformations [14]. This has been achieved by acquiring the well understood and densely populated LEED pattern for the Si(111) 7×7 reconstruction and mapping the distortion required to remove deviations from the known LEED pattern. At RT Huempfner *et al.* [14] observe coronene lattice parameters of (11.92 ± 0.05)nm and (12.29 ± 0.03)nm. This expressed in terms of the primitive basis is:

$$\begin{bmatrix} 4.00 \pm 0.02 & 1.00 \pm 0.02 \\ -3.01 \pm 0.01 & 3.01 \pm 0.01 \end{bmatrix}$$

This ordering applies to 1 ML of Cn at the surface, at 0.6 ML discrete spots turn to diffuse rings corresponding to 2D gas type behaviour. These have a reduced radius corresponding to a lattice parameter of roughly 1.58 nm figure 5.3(b). Cooling the 0.6 ML system to 1.1 K they see in the STM image of figure 5.3(a) that the reduced thermal energy makes it possible for low coverages to form stable ordering with respect to the substrate [14].
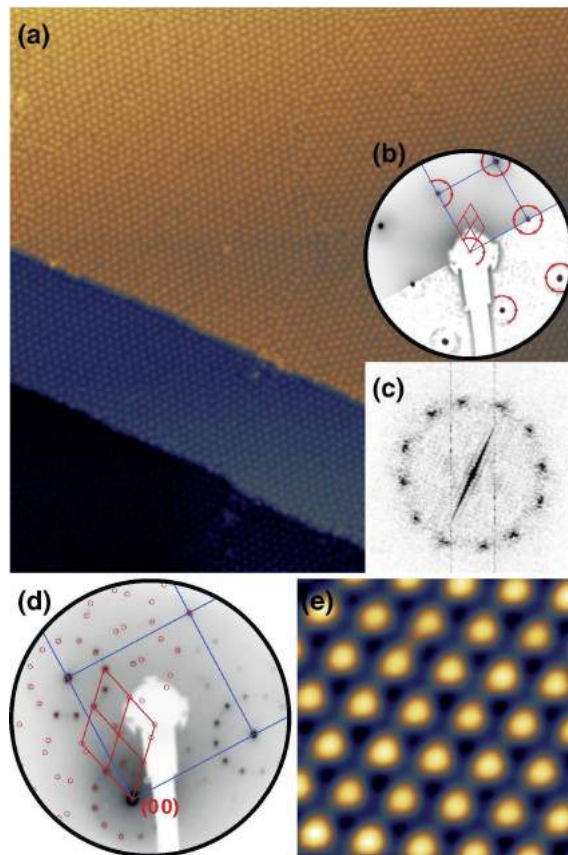
Figure 5.3: Figure and data reproduced from Huempfener *et al.* [14]. (a-c) are for 0.6 ML Cn, (d,e) are 1 ML (a) 1.1 K STM (100 × 100 nm², $V = 1.5$ V, $I = 50$ pA) (b) LEED pattern at 300 K, electron energy = 140.3 eV. (c) FFT of (a) showing domain alignment clearly. (d) LEED at 300 K, electron energy = 56.5 eV. (e) 1.1 K STM (6.3 × 6.3 nm², $V = 1.0$ V, $I = 60$ pA)

Reference	LEED		STM	
	1 ML	0.6 ML	1 ML	0.6 ML
This work	90 K, RT	—	RT	—
T. Huempfner [14]	RT	RT	1.1 K	1.1 K

Table 5.1: Summary of data presented in this work and that of Huempfner *et al.* [14] to illustrate their complementary nature.

5.3   Experimental procedure

The Ag(100) surface was prepared via cycles of Ar$^+$ sputtering at 0.5 keV with an ion flux of 10 μA cm^{-2} for 15 min followed by annealing to 670 K for 30 min, measured using a Minolta LAND pyrometer with emissivity set to 0.1. Deposition of coronene onto the Ag(100) surface carried out via evaporation under UHV at 463 K using a Dodecon organic molecular beam epitaxy (OMBE) source for 5 minutes. All experiments were conducted under the same deposition times. The surface was studied using LEED, collected using an OCI microLEED flat-screen optic and recorded via a CCD. Patterns were taken between 10 eV and 136 eV. STM was performed using an Omicron RT-STM1 equipped with the MATRIX control system.

5.4   Results

Significant work on the Cn/Ag(100) system as been previously reported by Huempfner *et al.* [14], using similar techniques to our work, but under different temperatures and coverages. In table 5.1 we present a summary of our work and that presented by Huempfner *et al.* [14] for reference.

5.4.1   LEED data correction

The flat screen LEED optic used for data collection introduces spherical aberration to the observed LEED pattern; substrate spots that should lie along straight lines
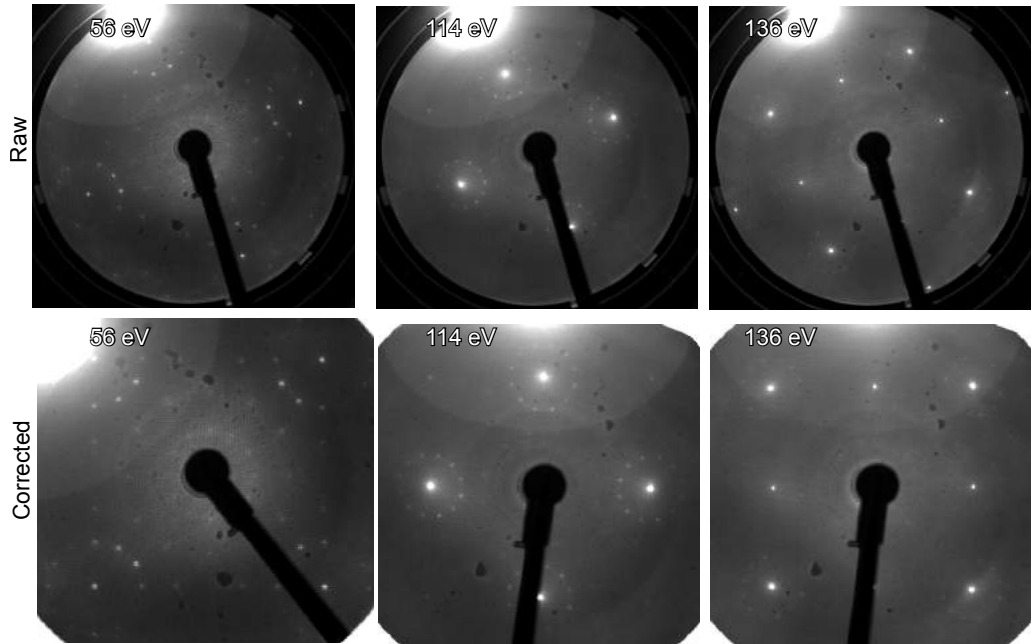
Figure 5.4: Low energy electron diffraction patterns taken of the Cn/Ag(100) surface at 90 K following a 5 minute deposition of coronene at a range of energies. Raw patterns are provided above and those manipulated in an attempt to correct for spherical aberration of the LEED pattern are provided below at 56 eV 114 eV and 136 eV

tended to bow about the centre of the optic. To correct for this, each LEED pattern was corrected about the optic centre, using a pincushion filter. The pincushion filter reduces the size of features towards the centre of the image, defined in our images as the centre of the LEED optic, using a quadratic function. This function was manually set with reference to the Ag(100) spots at several energies so that they appeared square. The best fitting function across these energies was then applied to all images. The results of this correction are shown with before and after examples in figure 5.4.

Additional non–spherical distortions of the pattern are present that this process cannot account for and so the process was carried out across several energies and features to determine the most appropriate correction factor before being applied uniformly to each image. From our data set it is not practical to determine a full correction for localised distortions however a recent system has been described that
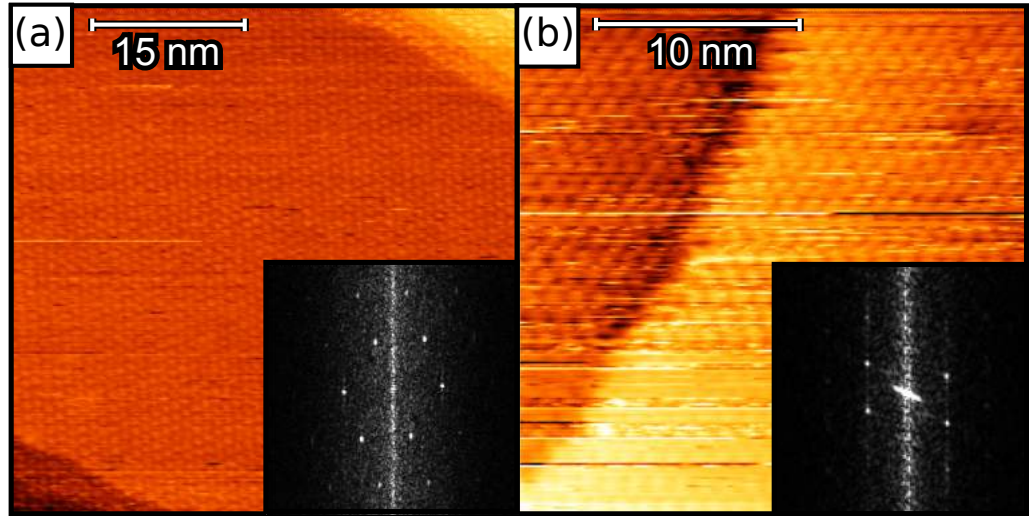
Figure 5.5: RT STM of Cn/Ag(100). Image A and B illustrate two different domains present for the same deposition and show large domains that continue across step edges. 2D FFT's are provided as inserts which more clearly demonstrate their domain directions are rotated approximately 90° to one another.

achieves this through observation of a dense LEED pattern from a known surface [116] as mentioned above.

5.4.2 Determining the Cn/Ag(100) relationship

LEED patterns of the system at room temperature show spots consistent with two 3–fold domains aligned approximately 15° off axis to the substrate axis as illustrated in figure 5.6(a). This is confirmed through STM of the surface showing hexagonal domains aligned perpendicularly to one another as shown in figure 5.5 through leveled z data and 2D FFTs.

We also see diminished spots midway between each of the principal bright spots as circled in figure 5.6(a). These relate to a superstructure (SS) aligned 45° from the domains of the dominant SS spots. The bright and diminished SS are henceforth referred to as SS A and SS B respectively.

Multiple measurements are taken for equivalent spot separations, for both the

substrate and Cn overlayer, to minimise the impact of aberrations in the LEED optics. These values are averaged and from this we obtain the Cn lattice parameter of (1.16 ± 0.15)nm. This is done by comparing the Cn spot separations with the substrate spot separations known to correspond to the real space Ag atomic separation of 0.289 nm. This is done using the real/reciprocal space relations defined in the introductory chapters. By averaging the overlayer spot separations to minimise the impact of screen distortion the assumption is made that the overlayer only has a *single* lattice parameter. This is incorrect however as the nearest neighbour axis of the Cn overlayer aligns with the crystallographic axis of the substrate. This substrate influenced ordering suggests that the structure of the Cn overlayer is quantised to the square lattice of the surface which necessitates two different lattice parameters for a hexagonal overlayer. This behaviour is in contrast to the 2D gas behaviour observed at lower coverages that is incommensurate and orders independently of the substrates influence [14]. Using this temporary, *single* lattice parameter derived from the LEED observations it is possible to map the adsorption pattern to the Ag(100) surface to determine the most probable structure. Again, the Cn domain alignment being restricted to the symmetry of the substrate means adsorption must be coincident or commensurate. The 3–fold symmetry of the SS A overlayer is incompatible with the substrate and so for commensurate adsorption the Cn superstructure must adopt a quasi-hexagonal arrangement with two different lattice parameters. This is illustrated in figure 5.7(a) where a regular hexagonal array is constructed from equivalent lattice parameters measured for SS A. This structure cannot conform to equivalent adsorption sites to the surface but with a small relaxation of the lattice parameters considered, the overlayer can adopt a commensurate relationship with the substrate. With this in mind, relaxing the proposed hexagon model shown in figure 5.7(b) and centring the Cn lattice points so they sit atop equivalent sites of the Ag(100) lattice produces a superstructure described by the following lattice
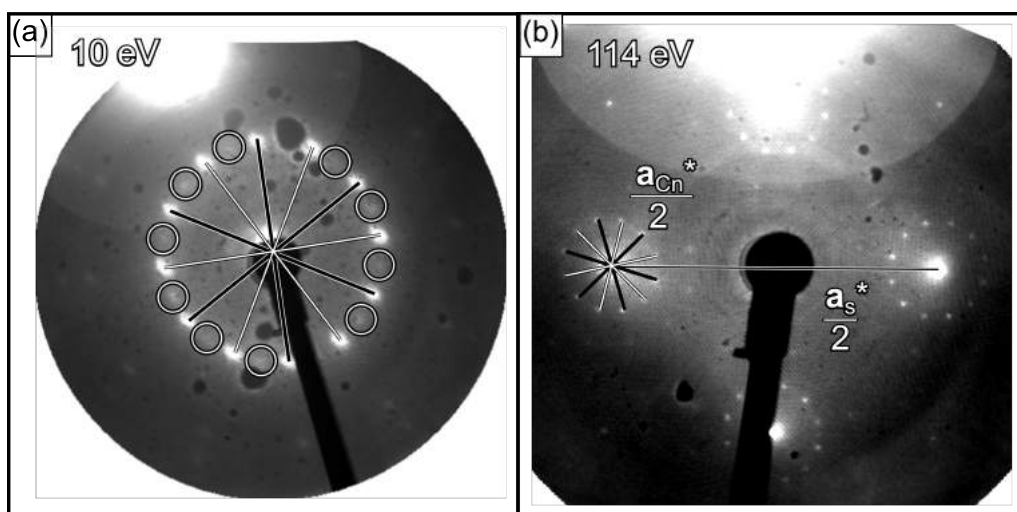
Figure 5.6: (a) LEED pattern at 10 eV with Cn domains marked. LEED patterns at low energies show additional systematic distortion being at the limits of the LEED optic focus and so we refrain from quantifying aspects of the structures shown. The two domains relating to SS A are marked with white and black lines. The diminished spots of the SS B domains are circled. (b) LEED taken at 114 eV of the Cn/Ag(100) system with the reciprocal lattice vectors of Cn SS A and the Ag(100) surface marked.
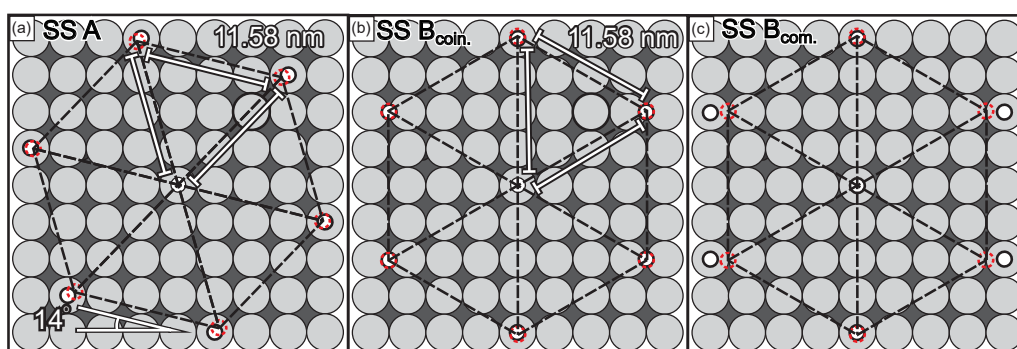
Figure 5.7: The Cn lattice parameters, obtained from the 90 K LEED data, of 11.58 nm are overlayed as black lines, with red circles denoting the predicted adsorption centres of Cn molecules on the surface. The white circles denote the centres once adjusted so that the adsorption sites share a coincident or commensurate relationship to the substrate. This is done for a) SS A, b) rotated 45° for SS B$_{coin.}$ c) rotated 45° and further expanded to the nearest commensurate structure for SS B$_{com.}$.

parameters:

$$\text{SS A} = \begin{bmatrix} -4 & 1 \\ 3 & 3 \end{bmatrix}$$

showing that at 90 K the primary Cn stucture, SS A is the same as reported by Huempfner *et al.* [14] at room temperature. A schematic of the system is shown in figure 5.8(a).

As mentioned previously, the 10 eV pattern (figure 5.6(a)) also shows two diminished 3 fold patterns oriented at 45° to the primary domain spots noted as SS B. The spots of SS B being diminished suggest it is the energetically less favourable domain at the surface. The spots relating to SS B are also present in the LEED patterns of Huempfner *et al.* reproduced in figure 5.9. This demonstrates that a second Cn phase comprises some proportion of the surface population at both RT and 90 K [14].

LEED optic distortion is worst at low energies and so we are limited to reliably measuring lattice parameters at high energies. Due to the dim nature of the secondary domain spots seen at 10 eV, the spots are undetectable at the higher energies required to independently measure the lattice parameter of the spots relating to SS B. No significant difference in the spot separations at 10 eV is observed between SS A and SS B and so we assume a comparable lattice parameter initially. To determine the structure of SS B we rotate the hexagonal lattice constructed from the averaged parameter of SS A as in Figure 5.7(a), 45°. This is shown in 5.7(b) using dashed lines to denote the proposed structure, and it is apparent that the result is not commensurate with the substrate lattice. A small relaxation of the lattice parameters to center the Cn sites (shown in red) atop the nearest high symmetry sites results in a coincident system, here to referred to as SS B$_{coin.}$ with the lattice parameters:
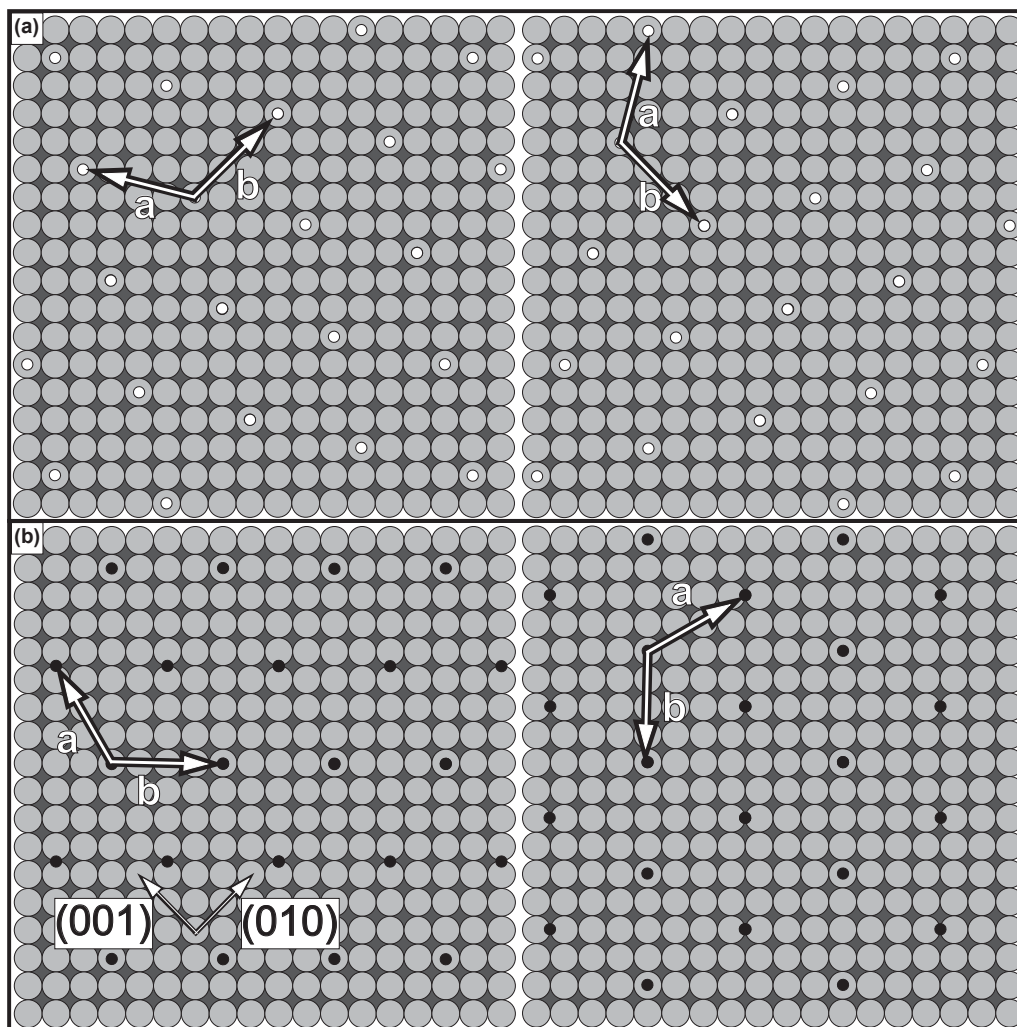
Figure 5.8: Figure (a) and (b) are schematics of the Ag(100) surface with the Cn ML lattice overlaid. Figure (a) has one domain of the dominant superstructure, SS A, marked in white and figure (b) has the minor super-structure, SS B, marked in black. Each SS has its equivalent, 90° rotated domain shown to the right of it, afforded by the substrate symmetry.
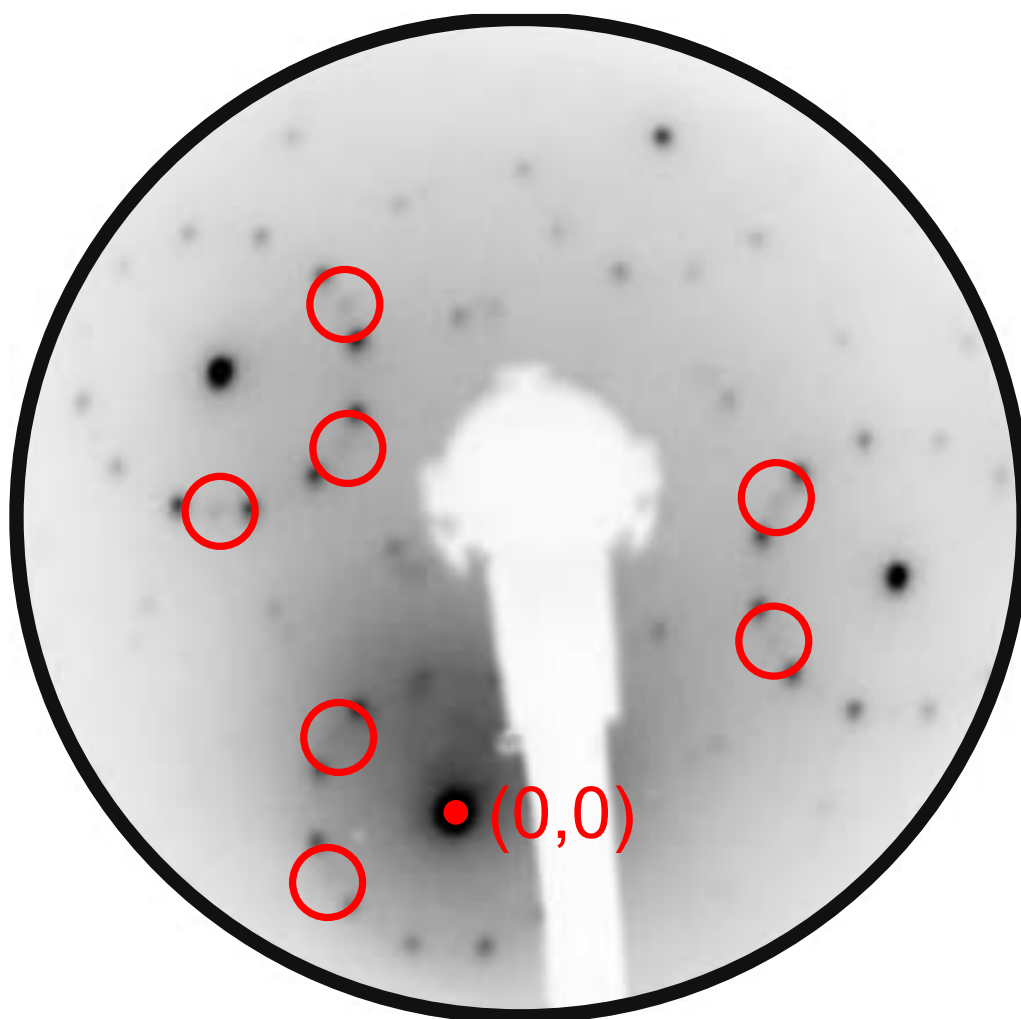
Figure 5.9: Image of RT LEED data at 56.5 eV of Cn/Ag(100) at RT altered and reproduced from [14]. Though not addressed by Huempfner *et al.* we can see some diffuse domain spots 45° out of phase to the primary domains evident. Prominent examples have been circled in red.
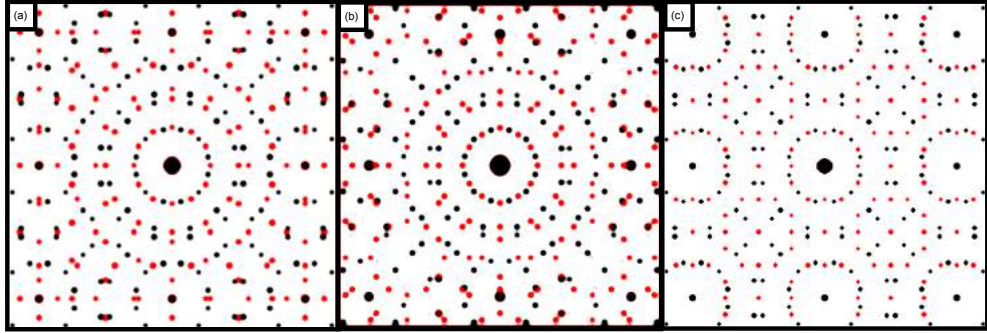
Figure 5.10: Predicted pattern using the determined superstructure vectors, generated using LEEDpat. (a) SS A in black and SS $B_{coin.}$ in red (b) SS A in black and SS A rotated 45° in red. (c) SS A in black and SS $B_{com.}$ in red.

$$\text{SS B}_{coin.} = \begin{bmatrix} -2 & 3.5 \\ 4 & 0 \end{bmatrix}$$

For this structure each Cn location alternates between a bridge site and atop atoms on the model Ag surface and results in a 7% greater density of coronene as seen from Table 5.2. Bridge and atop sites are chosen arbitrarily in this example to illustrate the spatial relationship of the real, unknown, adsorption sites. Simulating the reciprocal lattice of SS A and SS $B_{coin.}$ using LEEDpat [117] and superimposing these we obtain a model of the ideal LEED pattern as shown in figure 5.10(a). To better illustrate the presence of two unique structures, SS A is duplicated and rotated 45° in figure 5.10(b) and poorly replicates observed features in the LEED data.

Comparing simulated patterns to higher energy LEED patterns of the system is difficult due to the diminished SS B spot intensities. However at some energies at high contrast we can observe some inconsistencies between the SS $B_{coin.}$ model, its pattern in figure 5.10(a) and the LEED data. An example of an inconsistency is presented in figure 5.11, where the highlighted spot is not present in the simulated pattern for SS $B_{coin.}$. This rules SS $B_{coin.}$ out as a solution for the SS B structure. Through trial and error it is found that expanding the Cn lattice to the
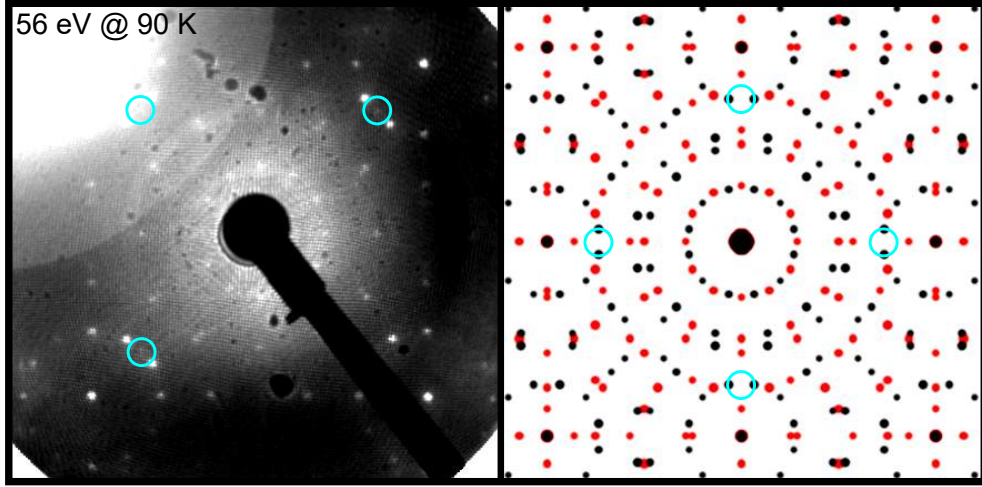
Figure 5.11: The diffraction spot highlighted by a blue ring in the LEED data is not explained by the predicted LEED pattern for SS B$_{coin.}$, displayed on the right in red, along side SS A in black.

next commensurate structure with the surface produces a solution that matches the resolvable spots in the data well. This structure, referred to as SS B$_{com.}$, is modeled in Figure 5.7(c) and simulated as a LEED pattern in conjunction with SS A, in Figure 5.10(c). SS B$_{com.}$ takes the form:

$$\text{SS B}_{com.} = \begin{bmatrix} -2 & 4 \\ 4 & 0 \end{bmatrix}$$

and a table comparing the SS A and SS B$_{com.}$ structures is presented in Table 5.2. The simulated pattern for SS B$_{com.}$ conforms well the SS B spots highlighted in the RT data of Huempfner *et al.* reproduced in Figure 5.9. The same spots identified in Figure 5.11 to rule out SS B$_{coin.}$ are evident in Huempfners *et al.* RT LEED data suggesting this is the same structure.

	LEED	superstructure A	superstructure B
a	11.58 nm	11.91 nm	11.56 nm
b	—	12.26 nm	12.92 nm
Surface density	—	0.791 Cn/nm^2	0.771 Cn/nm^2

Table 5.2: Lattice parameter summary of SS A and the SS B$_{com.}$ structures observed at 90 K

5.4.3   Room temperature LEED

The room temperature LEED data set is confounded with focusing issues meaning spots of the SS A and SS B structures appear more diffuse at higher energies and strange artefacts are seen at lower energies (see figure 5.13(c)). Despite this we see brighter spots at 25 eV corresponding to SS B when compared to the low temperature data. These seem to suggest a temperature dependency in the superstructure population ratios. We see SS B spots more readily at higher energies for the RT data set centred about the substrate spots, visible in 5.13(a). As at LT, the spots we see at RT also match poorly with the SSB$_{coin.}$ model but relate well to those of $SSB_{com.}$.

The simulated LEED pattern of SS B$_{com.}$ is consistent with the RT LEED results shown in figure 5.10(c) and figure 5.13(a) respectively. This is demonstrated in Figure 5.12 with SS B$_{com.}$ and SS A partially superimposed on to the data. It appears that SS A and SS B$_{com.}$ domains exist at both 90 K and RT. SS B$_{com.}$ is less dense than SS A and the spots appear brighter in the RT LEED than at 90 K suggesting this looser packing becomes more favourable at higher temperatures.

As said previously the room temperature LEED data of this system is of worse quality both in terms of ordering and in terms of apparent optic focusing issues. We see offset, duplicated features as seen in figure 5.13 that seem unlikely to result from faceting or some other real defect at the surface. Despite this some comparisons can be made between this and our 90 k data. We see long range order is noticeably reduced as expected but still present. Despite the focusing issues, some attempt can
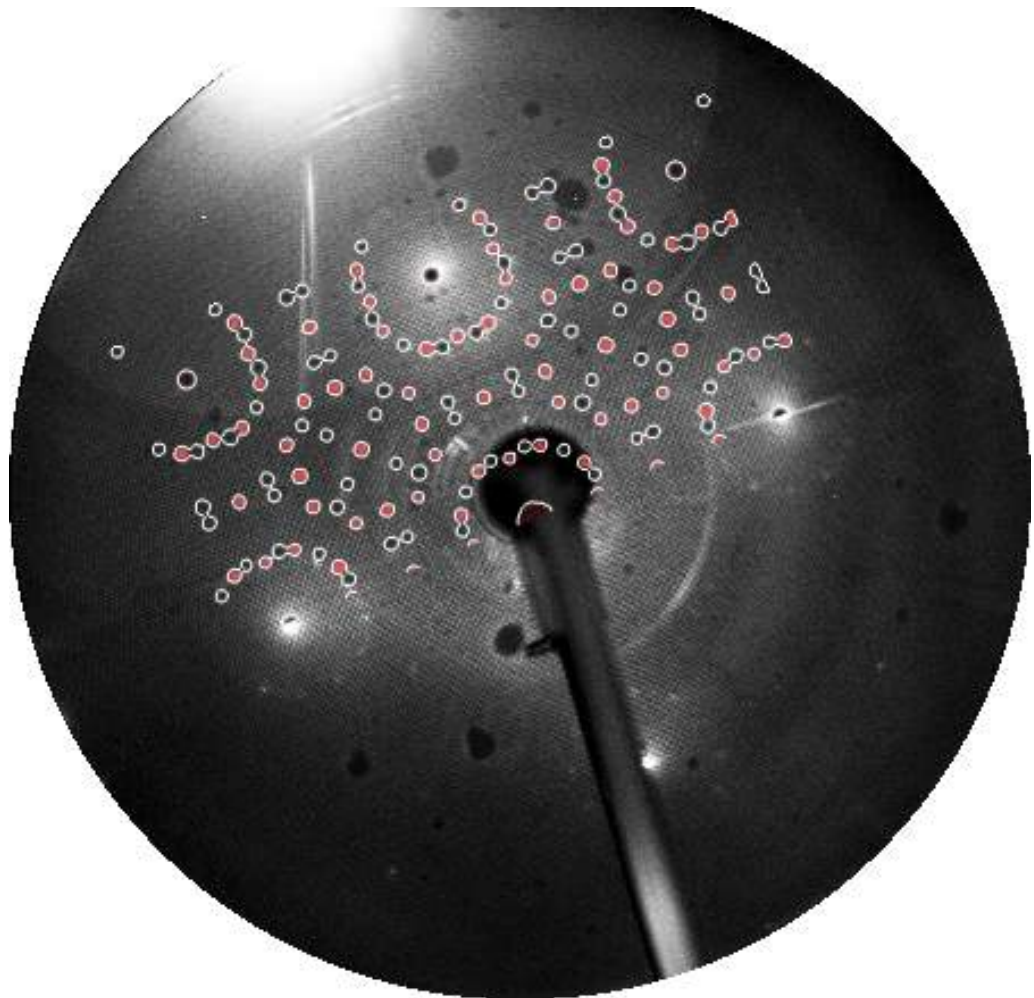
Figure 5.12: RT 112 eV LEED of Cn/Ag(100). The simulated LEED pattern relating to the SS B$_{com.}$ superstructure superimposed in red and SS A in black.
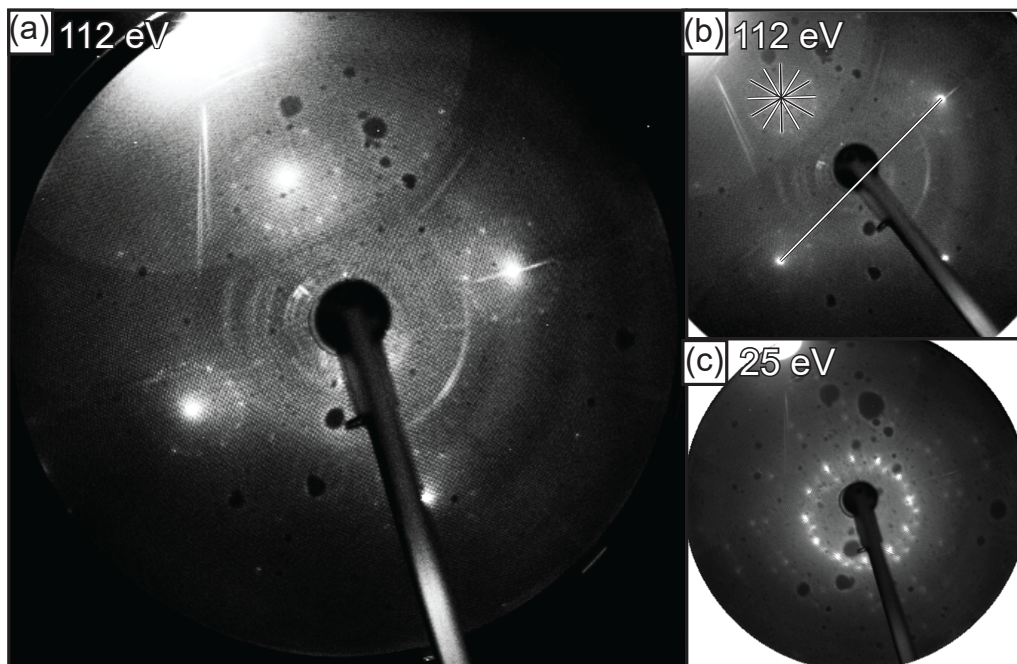
Figure 5.13: Low energy electron diffraction taken of the Cn/Ag(100) surface at RT taken at marked electron energies. a) 112 eV b) as (a) but with the Cn lattice vectors used to generate lattice parameters marked as carried out for the system at 90 K. c) Low energy pattern illustrating distortion and artefacts present at these energies.

be made in determining the lattice parameters for SS A from the 112 eV pattern in figure 5.13(b). The value obtained by ratio of the observed Ag(100) SS A structure are $a = 12.34\pm 0.27$ nm and $b = 12.86\pm 0.20$ nm. The errors on both parameters are calculated as the standard deviation of the 3 values taken for each vector of the two domains. These relate poorly to the known SS A structure of Cn/Ag(100) reported by Huempfner *et al.*. This failing is in part why we characterise the LEED using simulated patterns to replicate features as opposed to taking direct measurements.

We see no systematic patterning or change in appearance of Cn molecules in the RT STM data presented in figure 5.14, as might be expected of molecules adsorbed at different sites. This might be explained a weak interaction between the Cn molecules and the surface or by commensurate adsorption.

In the STM data presented in figure 5.5 we see evidence and confirm the presence
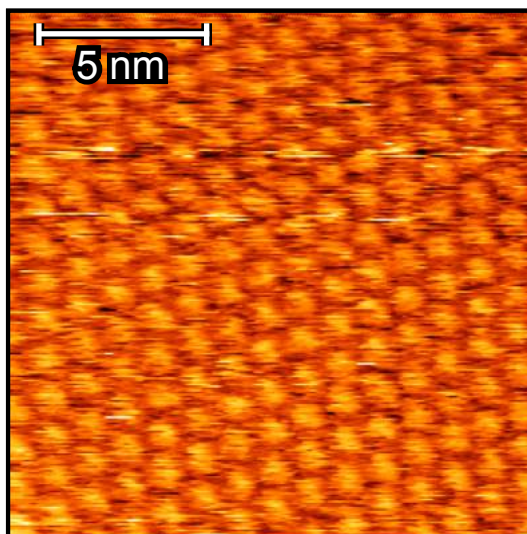
Figure 5.14: Close up of the Cn monolayer at room temperature with no evidence of molecular tilt or significantly different adsorption behaviour

of both primary domains at the surface of the sample in large domains. In the LT results of Huempfner *et al.* [14] clear domain boundaries are shown through STM but there is no well resolved instance of this in our study. The region between domains being consistently noisy and producing unstable images, presumably arising from molecule–tip interactions. This would coincide with the explanation that these regions are much less stable at room temperature, potentially with some degree of molecular diffusion occurring at these boundaries. It is not possible to discern between SS A or SS B domains in the STM data except by alignment in relation to the substrate. Whilst scanning we observe only two clear instances of differing domains as presented in figure 5.5. We expect four domains to exist at the surface and these should be identifiable by their nearest neighbour direction alignment in relation to the substrate but differentiating between SS A and SS B$_{com.}$ domains would still be difficult due to the effects of thermal drift experienced during STM. SS B$_{com.}$ lies along one crystallographic axis of the Ag(100) surface, and SS A is only 14° off axis, a small difference that can be obscured through drift induced image skewing.

5.4.4 Monolayer or multilayer Cn/Ag(100)

In the section discussing previous work on Cn/Ag(100) we state that little work has been done to characterise multilayer growth of Cn on similar systems, only Huempfner *et al.* present some work [14] which suggests it can happen atop Ag(111) as a disordered partial bilayer. The structure of Cn on Ag(111) is comparable to Ag(100) and so it must be considered that Cn adsorption beyond the monolayer might also be possible on Ag(100). For molecules to be reliably observed by the techniques of LEED or STM when adsorbing as a partial layer, they must either form an island or otherwise adsorb fixed in place. During our STM investigation we do not observe step heights indicative of multilayers or islanding atop the monolayer but this does not preclude their existence. We also do not see examples of singular, stable molecules adsorbed atop the ML at RT in STM.

LEED is only sensitive to surface structures however it is possible that diminished secondary structures observed in the LEED pattern pertain to an underlayer in the case of bilayer or multilayer Cn. This would however be at odds with the presence of both structures, SS A and SS $B_{com.}$, that we see in the work of Huempfner *et al.* [14] at ML coverage. Additionally the arrangement of these structures in separate layers would create an incommensurate relationship. This is incompatible with the observation that both systems are templated by the symmetry of the substrate.

As a result of this we can state that the most likely solution is that a single layer of ordered Cn has adsorbed and any subsequent molecules either desorb or are adsorbed atop this layer exist in a state of diffusion, unresolvable by STM and not contributing to the LEED pattern. If multiple layers are adsorbed, either as complete layers or as islands, then they must share the structure of the monolayer. By identifying the presence of SS $B_{com.}$ in the data of Huempfner *et al.* [14], who only dose the surface to the equivalent of a monolayer, we must conclude that both SS A and SS $B_{com.}$ exist in the monolayer and that neither is a structure restricted

to subsequent layers.

5.5 Conclusions

We identify the presence of two competing commensurate structures of Cn atop the Ag(100) surface, present at ML coverage at both RT and 90 K. The closer packed of the two structures, SS A is most dominant but SS B$_{com.}$ appears to have a greater presence at higher temperatures. This behaviour is similar to that observed on the Ag(110) surface, reported by Seidel *et al.* [75] where temperature and coverage influence the population ratios of two competing phases. We determine the same structure for the primary phase, SS A at 90 K as Huempfner *et al.* do for the system at RT. We see the SS B$_{com.}$ structure at RT in our LEED data and in that of unaddressed diffraction spots in the work of T Huempfner *et al.* [14]. These LEED spots are consistent with the LEED patterns generated from our proposed super structure in figure 5.10(c). We see much greater intensity in SS B$_{com.}$ LEED spots at RT compared to 90 K, perhaps indicative of different population ratio of SS A and SS B$_{com.}$ domains.

6

Dibromobianthryl on Ag(100)

This paper is presented as published in the journal of chemical physics [118], an errata is presented at the end.

6.1 Abstract

The interaction between dibromobianthryl (DBBA) and the Ag(100) surface is studied using scanning tunnelling microscopy and density functional theory. DBBA is prochiral on adsorption and forms racemic domains with molecular rows aligned with the substrate nearest-neighbor [011] and [0$\bar{1}$1] directions. Deposition at elevated temperature leads to the formation of disordered meandering graphene nanowires of constant width.

6.2 Introduction

This work is published in the Journal of Chemical Physics [118].

The study of the interactions of molecules and molecular layers with surfaces has long been of interest to both fundamental and applied science. In addition to their desirable and, more importantly, customisable, electronic properties, molecules

experience a range of intermolecular interactions leading to great complexity and variety in the 2- or 3-dimensional crystals that can be grown.

Recently, the rise of graphene has led to a renewed interest in depositing molecules at surfaces as a chemical feedstock for surface-mediated growth. This approach has much more promise industrially for the production of large single-layer sheets than the exfoliation of graphite [119].

A great part of the appeal of graphene is due to its potential for patterning. While continuous pristine graphene acts as an excellent conductor, electrons are confined by defects or by edges, leading to the opening of a semiconducting gap in the electronic density of states. These properties can in principle be used in digital electronic circuits formed by simply punching a particular shape out of a graphene sheet [120].

A commonly targeted shape for graphene development is the nano-ribbon (GNR), a high-aspect-ratio structure a few nanometers wide and many tens or hundreds of nanometers long. A *top-down* approach to constructing particular architectures from graphene consists of patterning using a probe or by etching or milling, but this approach fails to give the atomic precision necessary for control over GNR edge states [121]. An alternative *bottom-up* route is to use molecular precursors and polymerise them into extended graphene structures.

The formation of particular structures requires precise arrangements of precursor molecules and predictable decomposition pathways. The first requirement may be met via molecular self assembly and the second via use of the Ullmann reaction, in which some extremities of the precursor that are terminated with halogen atoms rather than hydrogen atoms lose their terminal atoms at a lower temperature than others. First the structure of interest is formed via molecular self-assembly and then it is 'cured' by heating to remove halogens. A final step is heating to a higher temperature to perform cyclodehydrogenation of the structure to form continuous
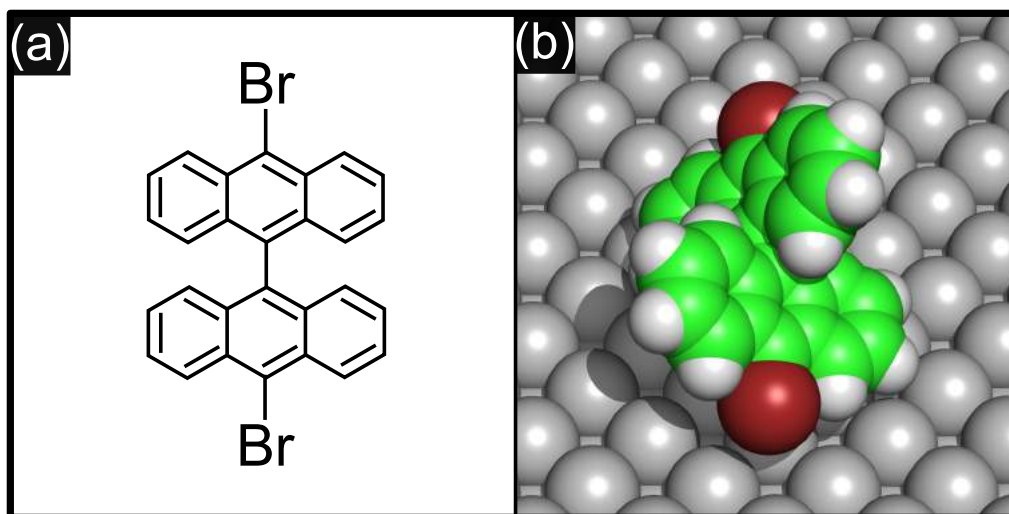
Figure 6.1: (a): dibromobianthryl (DBBA), (b) one optimal configuration via DFT of isolated DBBA atop Ag(100).

graphene domains.

Dibromobianthryl, (DBBA, also referred to as polyanthrylene in a polymerised state) shown in figure 6.1(a), is composed of two anthracene molecules symmetrically joined in the direction across their width and, in the same direction, terminated with Br atoms [122]. One optimal configuration of DBBA atop Ag(100), found via density functional theory (DFT), is shown in figure 6.1(b). This is further discussed in section 6.6.

The progression of DBBA to GNRs has been described at length [9, 123, 124, 33, 15, 125]. The use of DBBA has apparently been motivated by a wish to use the advantageous Ullmann dissociation reaction to polymerise DBBA in an ordered, Br-end to Br-end, fashion [9]. Following polymerization, the temperature is raised further and cyclodehydrogenation occurs, with the result that the DBBA chains flatten into GNRs as C-C bonds form between the angled moieties. This happens as described for Ag(111) and Au(111) substrates, but, following some controversy, it has recently become unambiguously clear that the molecules line up *side-by-side* on a Cu(111) substrate, following which polymerisation into chiral GNRs occurs [125],

meaning that Ullmann dissociation is not crucial for this process. This has been further supported by the successful growth of identical chiral GNRs using bianthryl precursors *without* terminal Br atoms, reported in the same study.

Using Ag(111) as a substrate, Cai *et al.* outlined a route to GNR formation from DBBA [9]. More recent work [33] identifies a different process to that for adsorption on Cu(111), with the initial debromination and cyclodehydrogenation leading to an intermediate stage of flattened graphene platelets on Ag(111) that can then be polymerised into GNRs through continued annealing. This behavior is markedly different from the Ullmann reaction based scheme described by Cai *et al.* [9].

"One study reports the adsorption of DBBA atop Cu(110). The Cu(110) surface structure enforces a molecular film superstructure that precludes polymerisation before or during cyclodehydrogenation, leading to the formation of individual platelets of graphene the size of the precursor molecules [126]. For both Cu surfaces, Br completely dissociates at 240 K but stays at the Cu surface. For Cu(110) dissociated Br atoms appear to play a role in the inhibition of graphene formation as they form an ordered network between dehydrogenated bianthryls [126]. For Au(111) Br dissociation starts at 360 K and is complete at 410 K. Desorption of Br starts with dissociation but some Br remains at the Au(111) surface up to complete desorption at 470 K [15].

No work concerning growth of GNRs has been carried out on transition metal (100) surfaces. We concentrate on this subject here, as the growth of graphene on substrates with non-hexagonal symmetry must place strain on the lattice, which may influence ribbon growth through deformation similar to that produced at conventional domain boundaries [127, 128]. Such nanostructures have been shown to significantly alter the local electronic properties and transport characteristics [129, 130, 31, 127].

Dibromobianthryl itself is prochiral. As a free molecule, it is achiral but association with a surface restricts symmetry operations. Therefore adsorption at a surface leads to geometries which are chirally related. This is different to the helical chirality referred to in the phrase 'chiral GNRs'. The aforementioned phenomenon has no relevance to the formation of chiral GNRs as it is lost in the early dehydrogenation stage of polymerization.

Chiral assemblies and nanostructures in themselves present exciting applications in optoelectronics [5] and manifest most topically in GNR edge structures, achieved through both unzipping of carbon nanotubes [131] and in staggered or systematically offset molecular assembly [132].

6.3   Experimental procedure

Deposition of DBBA on to a Ag(100) surface was carried out via evaporation under UHV at 485 K using a Dodecon organic molecular beam epitaxy source. In one experiment, DBBA was deposited to submonolayer coverage on the substrate at room temperature, followed by measurements using scanning tunnelling microscopy (STM). The system was then annealed to 470 K followed by STM. In a separate investigation, DBBA was deposited on the Ag(100) surface maintained at 670 K. The Ag(100) surface was prepared via cycles of Ar^+ sputtering at 0.5 keV with an ion flux of 10 μA cm^{-2} for 15 minutes followed by annealing to 670 K for 30 minutes, measured using a Minolta LAND pyrometer with emissivity set to 0.1. Prior to deposition the DBBA source was outgassed at 490 K. Source–sample separation during deposition was ~10 cm and the deposition duration was 180 s for all experiments. STM was performed on an Omicron RT-STM1 equipped with the MATRIX control system. The scanner was calibrated with a single calibration coefficient measured at 10 nm scan range using the clean Ag(100) surface. The tips used were commercially manufactured W tips.

6.4 Computational details

The static calculations for total energies were performed using the Vienna *ab initio* simulation package (VASP) [133, 134, 135, 135, 136] including the projector augmented wave (PAW) [137] potentials. A kinetic energy cut-off of 400 eV was applied for the plane waves. The exchange and correlation functionals were treated by the generalized-gradient approximation (GGA) of Perdew-Burke-Ernzerhof (PBE) as proposed by Perdew, Burke, and Ernzerhof [138]. The 6×6×1 Monkhorst-Pack mesh [139] was used for k-point sampling. The Ag surface was modelled using the supercell approach, where periodic boundary conditions are applied to the central supercell so that it is reproduced periodically throughout xyz-space. The surface slab was modelled with 5 layers of Ag atoms. A region of approximately 20 Å of vacuum was inserted in the z-direction to prevent interactions occurring between periodic images. The bottommost layer of the surface slab was frozen during the geometry relaxation. For the description of long-range van der Waals (van der Waals) energy the optB86b-van der Waals functional [140] was used.

The lattice constant that DFT gives depends on the functional used. Standard PBE overestimates bulk lattice constants due to the inherent tendency of the local-density approximation (LDA) to distribute charge uniformly which is not the case, especially in metals. The van der Waals density functional (van der Waals-DF) method better predicts the lattice constant through the formulation of the long-range dispersive effects on the correlation part and the optimization of exchange energy, so called the optB86b functional. In our calculation the lattice constant value is 4.10 Å, which is close to the experimental value of 4.07 Å.

6.5 Results and discussion

6.5.1 DBBA adsorption at room temperature

Submonolayer DBBA on the Ag(100) surface at room temperature forms islands composed of ordered molecular domains, shown in figure 6.2. As these appear in two orientations at approximately right angles, we conclude that they are aligned with high-symmetry axes in the Ag(100) surface. These may be either the [010] and [001] crystallographic primary axes or the [011] and [0$\bar{1}$1] nearest-neighbor axes. Any other relationship with surface axes would lead to degenerate ordering and more observed azimuthal domain orientations. We explore this argument in more detail later. Orientation parallel to the nearest-neighbor axes ([011] and [0$\bar{1}$1]) fits better with the atomic resolution data shown in figure 6.2(a).

Significantly different scanning parameters are required to image the molecules and the substrate with atomic resolution, so the two do not coexist in the same frame. This is an oft-encountered issue with determining molecular ordering at surfaces. We therefore present atomic resolution data collected within the same experimental run in the inset to figure 6.2 (a). In figure 6.7 in Supporting Information we present data from a new sample and new orientation, leading to two different sets of primary axes for the two runs and showing the same alignment.

The coexistence of both island orientations in figure 6.2(b) allows the absolute correction of thermal drift. We distort the image to give the image in the lower portion of figure 6.2(b), in which the rows in differing domains are perpendicular to one another with a matching equivalent molecular spacing within each row.

In our dataset, covering approximately 2 microns on 2 different samples, we see only 2 island orientations per sample. Given a single molecule which tends to agglomerate to form islands, adsorption on a four-fold substrate leads to two possibilities: either, the molecule experiences no interaction potential energy surface
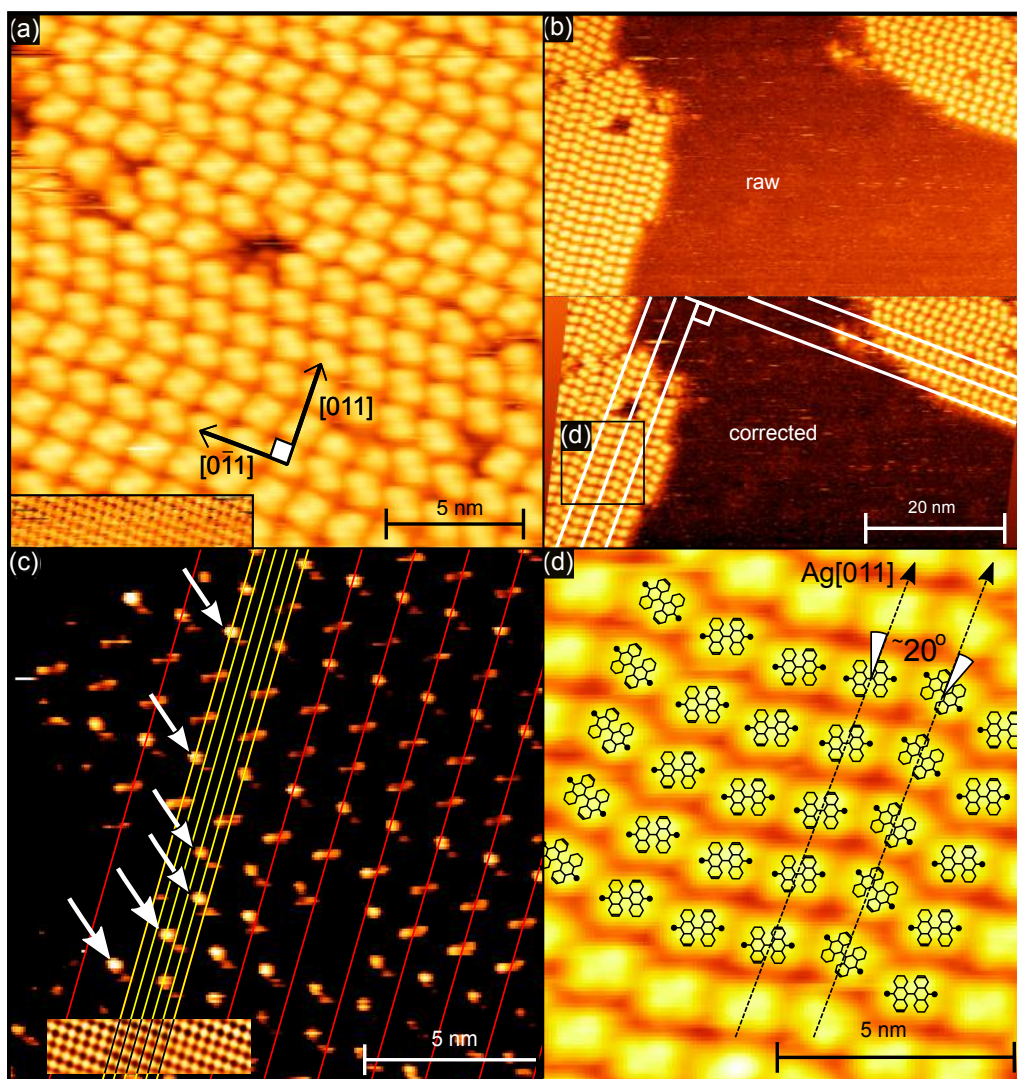
Figure 6.2: (a) Scanning tunnelling topograph of a single racemic domain of DBBA/Ag(100) ($V_B = 2.5$ V, $I_T = 100$ pA) *Inset:* Atomic resolution on the clean Ag(100) surface ($V_B = -1$ V, $I_T = 1.5$ nA), (b) Raw and corrected STM topographs of simultaneous resolution of two racemic domains at right-angles ($V_B = -2.5$ V, $I_T = 100$ pA). The corrections applied are plane-correction and x and y scale and skew factors inferred from the rotated but otherwise equivalent domains. The data for panel (d) is indicated. (c) Contrast enhanced STM topograph. Red lines indicate intra-row molecular separation. Yellow lines indicate surface atomic separation for p(5×5) superstructure. White arrows indicate molecules of the same chirality. In this image, tip LDOS asymmetry leads to a difference in contrast for the two chiralities. *Inset* Fourier filtered image of the Ag(100) surface plotted at the same scale as the image. (d) The proposed approximate orientations for the DBBA molecules superimposed on the detail indicated in (b).
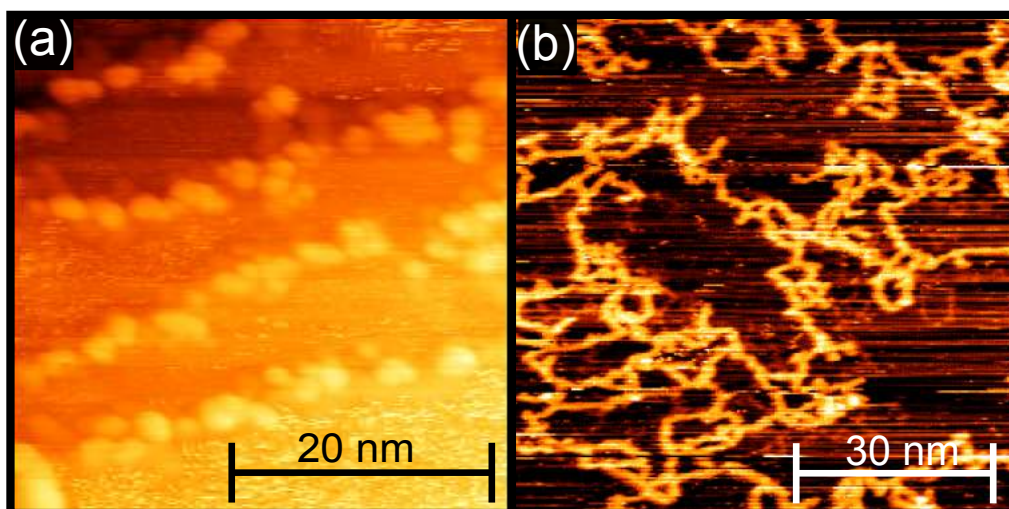
Figure 6.3: (a) Scanning tunnelling topograph taken after annealing to 470 K ($V_B = -3.5$ V, $I_T = 50$ pA). (b) Disordered graphene nanoribbons formed during deposition of DBBA on Ag(100) heated to 670 K ($V_B = -2.5$ V, $I_T = 100$ pA).

corrugation and forms azimuthally disordered islands, or it does experience corruga-tion thereof, hence forming azimuthally ordered islands. If the molecule is perfectly 'square' it is likely that it will form islands in a single orientation. If the molecule is 2-fold, such as DBBA, the minimum number of island orientations is 2, with the 2-fold axis coincident along either one (nearest-neighbor (NN), [011], [0$\bar{1}$1]) or the other ($\sqrt{2}$·NN, [010], [001]) group of substrate high symmetry axes. More than 2 arrangements are possible: any deviation from alignment along a high symmetry axis must then have the high-symmetry axis as a degenerate mirror axis, as these adsorption situations are necessarily energetically equivalent. The 2 orientations we see must therefore be symmetrically equivalent with the only difference being alignment along one or the other substrate high symmetry direction. Therefore, the angle between the islands must be 90° and the intermolecular separation in the rows must be equal.

From the corrected data we determine the overlayer superstructure. First, we note that the unit cell is square. This is clear from the drift-corrected data: the

inter-row separation of one domain determines the intra-row separation of the right-angled domain, and vice versa. The staggering between domains must be quantized by the Ag(100) atomic separation, which we find to be one-fifth of the molecular unit cell, shown in figure 6.2(c). We ensure that only molecules of the same chirality are considered by choosing an STM image in which asymmetry in the tip local density of states (LDOS) leads to a different appearance for different DBBA chiralities. This leads to the conclusion that the DBBA structure is described primarily by a $p(5 \times 5)$ arrangement.

Applying this description to corrected data of a single domain, at a shorter length scale, gives a clearer picture for determining molecular alignment with respect to the substrate as shown in figure 6.2(d). The central axes of the molecules seem to lie at approximately 20° to the domain axes (and therefore the substrate NN axes).

There are 2 types of molecular row in the domains which appear to be oriented differently to each other. The two remaining degrees of freedom available to a DBBA molecule of fixed location and molecular plane are azimuthal orientation and chirality. For a (100) surface, the azimuthal orientation is quantized to $(90 \pm \theta)°$, where θ is some degenerate domain angle. As argued above, the 2 domains observed in our data dictate that $\theta = 0°$. Chirality is expressed upon adsorption as either top left corner up or top left corner down, which is sufficient to determine the positions of the other three corners of the molecule.

We find that within a given domain, the freedom expressed is chirality; i.e., different molecules within a given domain have mirror symmetry about the substrate NN axes. DBBA is prochiral and 2-fold rotationally symmetrical about the center azimuth, so the two different chiralities are completely superimposable except due to the constraint by a surface. Therefore the interactions each chirality has with the surface are completely symmetrically equivalent and identical in every way except that they are not superposable.

As the chirality of each row is random, each domain island is approximately racemic. This contrasts with the situation where prochiral molecules adopt an inherently racemic structure with a unit cell including one of each enantiomer, as observed for e.g. dicarboxystilbene on Cu(110) [141].For the opposite domain, the mirror symmetry of inequivalent molecules is maintained and the molecules are at right-angles to those in the first domain.

As mentioned earlier, the chirality referred to here is unrelated to the edge chirality of GNRs grown on Cu(111). It is due to the prochirality of DBBA in the shape of the relative rotation of the anthryl moieties and is manifested when adsorbed on a surface.

In studies using Cu(110) and (111), Br dissociates from the molecules well below room temperature. However, these atoms do not desorb completely until 620 K [15], and remain as distinct spherical features that stay at the periphery of assemblies of bianthryls, polyanthryls or GNRs [126] – that is, Br atoms are visible as spherical features throughout several stages in the formation of GNRs. The spherical features also seem to appear in STM data from DBBA/Ag(111) after heating to 450 K, but an explanation thereof is not given in the article [33]. We do not see these features at any point, indicating that the Br is still attached to the DBBA molecules at room temperature. Following annealing to 470 K, Br has desorbed completely from Ag(100), as detected via x-ray photoelectron spectroscopy data (shown in Supplementary information figure 6.6)

The observation of just four situations for molecules, in keeping with the 4-fold symmetry of the surface and the prochirality of the molecule indicates that the two rotations and chiral conformations are geometrically identical in terms of their relationship with the surface. Rotational symmetry breaking is limited to the scale of the maximum domain size, which, while larger than any island we observe, is still on the sub-micron scale, as determined by the domain separation. In addition it

only runs along rows; as mentioned above, each row has a random chirality.

Following dehalogenation of the DBBA by raising the temperature to 470 K, ordered molecular material is not observed via STM. We observe disordered clumps at step edges surrounded by noise, as in figure 6.3(a). Cyclodehydrogenation of dehalogenated DBBA (that occurs prior to polymerization) has been observed on Ag(111) at temperatures of 450 K [33]. Hence, it seem likely that the disordered material we find at step edges is agglomerations of these nanoplatelets.

DBBA adsorption at elevated temperature

For adsorption of DBBA on Ag(100) maintained at 670 K, we observe disordered linear features, as reproduced in figure 6.3(b). These indicate that polymerisation does occur under these adsorption conditions. However, in contrast to the behavior for the Ag(111) surface, sustained linear growth appears less favored on the (100) surface as seen in figure 6.3(b). We do not observe the 'zig-zag' pattern associated with polymerised DBBA. The linear features are essentially flat. This is expected if the DBBA dehydrogenates to form nanoplatelets prior to polymerisation. The width of GNRs seen in our data of ~1 nm seems consistent with single DBBA chains of 7 carbon rows. GNRs with greater widths are evident but appear sporadically, with a tendency to sit at chain convergence points (figure 6.3(b)). GNRs wider than 1 nm never extend beyond 10 nm in length for the low coverage observed. In addition to this we also see brighter regions present in the GNRs. These are prevalent mostly at wider regions and junctions within the GNR. This appearance may arise from lattice deformations at GNR junctions leading to altered topography or LDOS. The same has been observed at GNR terminations on Ag(111) and Au(111) [142].

The lack of extended 1-dimensional growth points to the existence of more coupling arrangements than the end-to-end Ullmann reaction. In fact, it may be that the Ullmann reaction is not important in this system, as has been shown for DBBA

adsorption atop Cu(111) [125].

6.6 DFT

This section is included for completeness. DFT work was performed by Matti Lahti at Lappeenranta University of Technology [118].

First, we use DFT to find the adsorption site for a single molecule, shown in figures 6.1(b) and 6.4(a). Coordinates for the relaxed model are given in the Supplementary info. We find that many azimuthally related sites exist with approximately the same adsorption energy. The main feature of the adsorption is that sites are preferred which reduce the minimum C-Ag(100) distance. This appears to principally support adsorption even if only one C atom can get closer than others. In general, adsorption energies are low, in the region of 1.7 – 1.8 eV per molecule. We attribute this to the crossed three-dimensional shape of the molecule preventing a close association between surface electrons and the π systems of the anthryl groups. Bader analysis shows that there is no charge transfer from the substrate to the DBBA.

The bonding of the DBBA molecule (shown in figure 6.4) is far from simple regardless of the apparent contact between the molecule and substrate. Different energy ranges for bonding can be identified: the red region represents Br atom bonding, the green region C atom bonding and in the purple region bonding is seen for both Br and C.

DFT finds that adsorption is preferred (-0.3 eV/molecule) with one C end and so one Br atom closer to the surface than the other. This is not detectable in STM topographs. The magnitude of the tilt is such that it ought to be visible, so we conclude that at room temperature, the molecules are able to oscillate between degenerate tilted states. On Ag(111), the tilt seems to be visible (in SI of reference [33]). The closer surface Ag packing suggests a tighter DBBA packing that may lock in the tilt on the (111) surface.
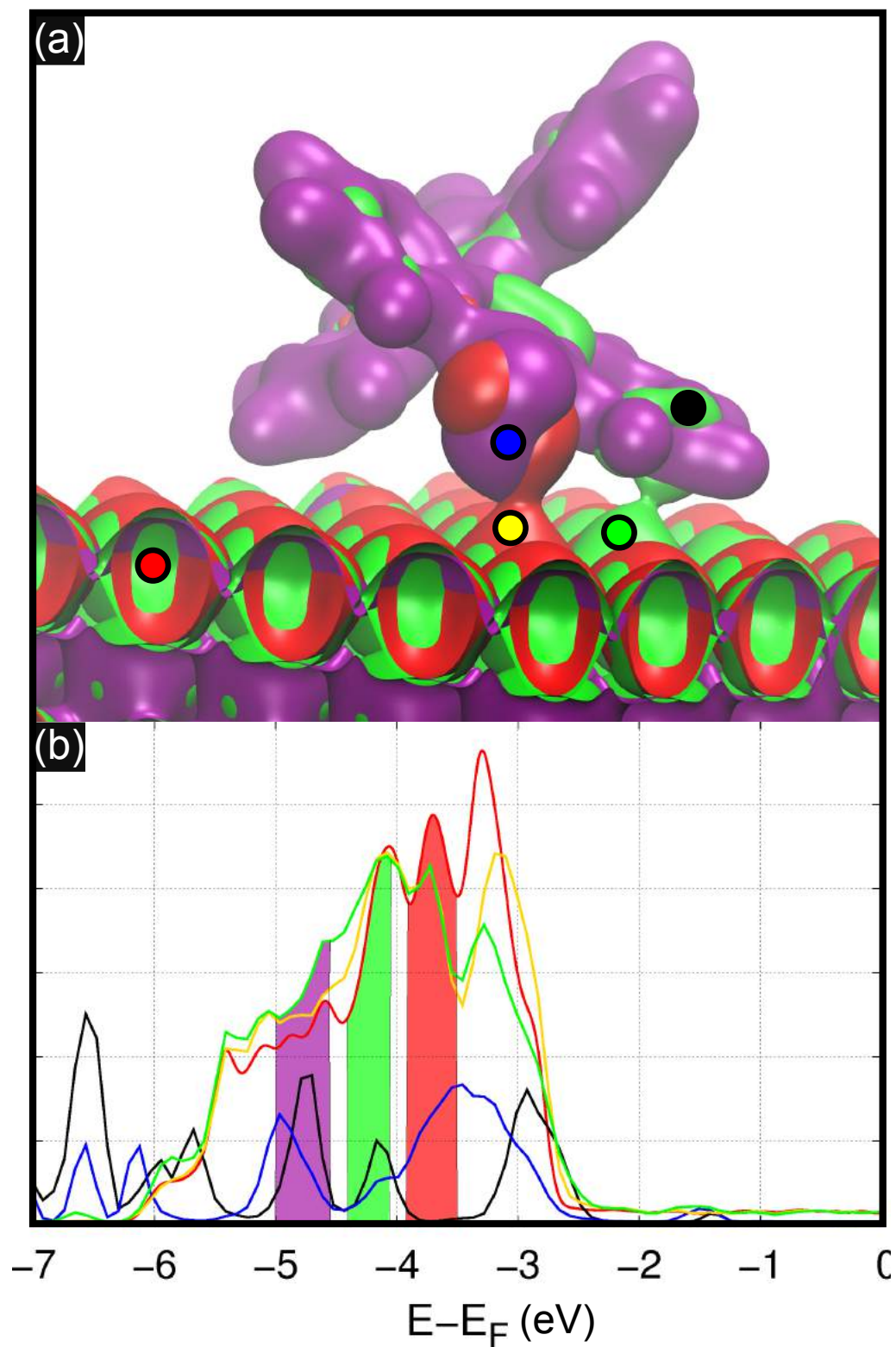
Figure 6.4: (a) Partial charge density map of a DBBA molecule on Ag(100). The energy ranges of the colored zones are indicated in the density of states curves shown in (b). The curves are for the atoms indicated with the dots shown on the map.
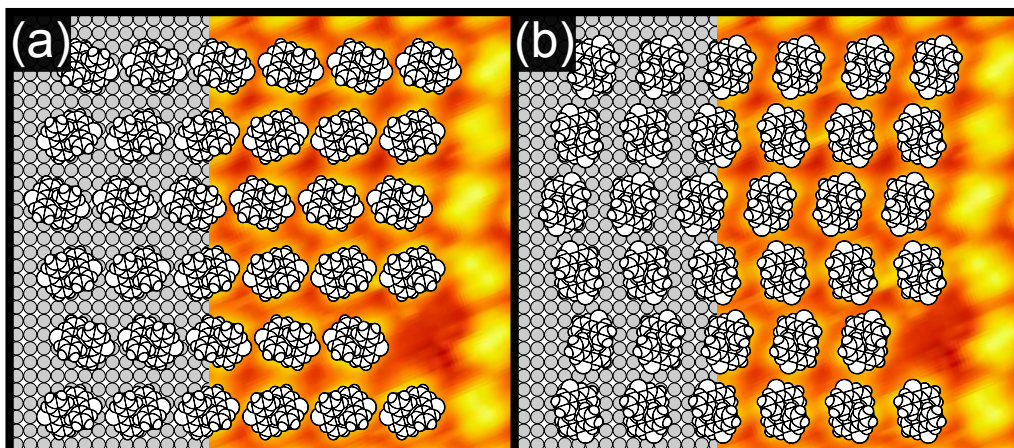
Figure 6.5: The two options for azimuthal orientation in the p(5 × 5) super-structure, depending on the intermolecular interaction. (a) oriented with Br–Br axes at ±20° to the molecular row axis. (b) oriented with Br–Br axes perpendicular to lines at ±20° to the molecular row axis. The figure is to scale with the portions of STM topography shown. Further discussion in text.

DFT does not show spontaneous debromination. In fact, when dissociated Br and debrominated DBBA are coadsorbed, they reattach during the simulation. Thus debromination requires some external energy. This is in keeping with our results that do not show evidence of debromination at room temperature.

6.6.1 Azimuthal orientation of individual molecules

There has been some controversy regarding the formation of purely armchair versus partially chiral GNRs from DBBA on Cu(111) [15, 125]. This originated in differing interpretations of the relative orientation of DBBA molecules in the rows of molecules that form as precursors to GNRs. The options for relative orientations are shown in figure 6.5.

The driving force behind one orientation is interaction between Br atoms on adjacent molecules. For the other it is interaction between H atoms. The former leads to achiral GNRs and the latter to chiral GNRs. Although for Cu(111) it was unambiguously shown that the second arrangement is in fact the correct one – and

additionally, Br plays no role in the polymerization process – the first arrangement has been indirectly observed on Ag(111) [33] and Au(111) [9] as the GNRs formed are achiral.

DFT shows negligible preference for any particular azimuthal orientation at 0 K. We find that there is very little effect on the adsorption energy when azimuthally rotating the molecule in the unit cell of a domain ($\sim$0.1 eV). This indicates that the orientation preference originates in intermolecular interactions rather than influence from the substrate. The size of the unit cell does affect the energy of adsorption; the best unit cell by DFT is p(4×4). As we observe p(5×5) superstructure via STM, we are led to the conclusion that room temperature thermal excitations are allowing the molecule to move between all the available local minima in the adsorption potential energy surface, which increases their apparent size, forcing the p(5 × 5) structure and also forcing intermolecular interactions that stabilise one orientation for all molecules in a row. When the molecules are in a p(5 × 5) structure (or larger), we find no orientation-dependent intermolecular interaction strong enough to affect the adsorption energy to within 3 significant figures.

As shown in figures 6.2(d) and 6.5, the topography of DBBA molecules from STM is measured as square, with diagonally opposite corners bright (or dark). This is a difficult shape to unambiguously assign an orientation to. The most likely options, considering the scanning tunnelling topographs, are shown in figure 6.5. Panel (b) has similar orientation to that found for Cu(111). The molecular NN is 1.4(4) nm, which is consistent with the molecular domains measured atop Cu(111) and Cu(110), though comparisons are limited as debromination is spontaneous at RT on these substrates.

The best adsorption site by DFT is not symmetrical. As argued above, since we only observe 4 kinds of molecules in this film, the molecules must have thermal motion and have time-averaged occupation of all the sites with adsorption energies

below their thermal energy. This would increase their interaction range slightly and also give them the symmetry observed.

However these observations cannot help in unambiguously determining the azimuthal orientation of the molecules within the p(4 × 4) superstructure. By inspection, it would appear that the STM images most closely match that shown in figure 6.5(b), which would mirror the interaction found on Cu(111) [125].

6.7   Conclusions

We have deposited dibromobianthryl onto the Ag(100) surface at room temperature. We find that the DBBA molecule shape leads to prochiral adsorption. The molecules agglomerate into domain islands composed of rows of end to end molecules. Although the domains have a predominantly square p(5×5) superstructure, adjacent rows are sometimes staggered with registration quantized to the Ag NN distance. Rather than the azimuthal rotation defining different rows within a domain, we find instead mirror-flipped molecules defining different rows within domains that are on average racemic.

Following the four-fold symmetry of the substrate, racemic right-angle rotated domains also exist, which again consist of randomly staggered rows related by chiral, rather than azimuthal, symmetry.

Moderate heating causes the loss of Br from the molecules and surface. The molecules polymerise into clumps and randomly decorate the step edges.

We have also deposited DBBA directly on a Ag(100) surface maintained at high temperature. The molecules polymerise into chains that are short and meandering, indicating that it is unlikely that end-to-end Ullmann coupling is the sole polymerisation mechanism.

DFT analysis indicates that C dominates the molecule-surface interaction and that spontaneous dehalogenation requires some external energy on Ag(100). There

is very poor selectivity of adsorption site at 0 K and at the separation found experimentally (p(5×5)) there is no intermolecular interaction expected.

Despite this, experimental findings indicate large, well-ordered islands with few degrees of freedom, so we conclude that at room temperature, the molecules oscillate between several closely spaced local potential energy minima, increasing their interaction range and forcing the more open p(5×5) structure. The lattice parameter of this structure is 14.4 Å.

6.8   Supplementary information

Here we include the coordinates of the relaxed DBBA/Ag(100) unit cell as generated by DFT.

Element	x (Å)	y (Å)	z (Å)
Ag	0.000010	2.903905	2.035167
Ag	2.903914	2.903933	2.035909
Ag	5.807076	2.903933	2.035900
Ag	8.710667	0.000000	2.035900
Ag	11.614495	0.000000	2.035900
Ag	8.710667	2.903905	2.035900
Ag	11.614495	2.903905	2.035900
Ag	1.446484	1.448627	3.794786
Ag	4.355287	1.450334	3.799963
Ag	7.264535	1.451002	3.790632
Ag	1.446456	4.360543	3.788612
Ag	4.354973	4.362027	3.794007
Ag	7.264596	4.363220	3.791374
Ag	10.166028	1.450495	3.788925

Ag	13.062388	1.451826	3.784906
Ag	10.165291	4.362501	3.785076
Ag	13.063339	4.361754	3.785783
Ag	5.824208	14.505841	5.578924
Ag	2.889357	2.917851	5.577136
Ag	5.819411	2.920164	5.569785
Ag	8.723636	14.507847	5.579016
Ag	11.610148	14.515893	5.582484
Ag	8.729895	2.908473	5.572870
Ag	11.615450	2.911495	5.578843
Ag	1.399389	1.467069	7.324959
Ag	4.389816	1.471777	7.318445
Ag	7.289150	1.455725	7.350732
Ag	1.431892	4.378241	7.383348
Ag	4.335608	4.372943	7.369450
Ag	7.284468	4.349575	7.355742
Ag	10.168530	1.452812	7.379756
Ag	13.050032	1.460167	7.370154
Ag	10.169410	4.355405	7.380602
Ag	13.065791	4.364672	7.389526
Ag	14.509014	14.525376	9.111755
Ag	5.828585	0.021148	9.093655
Ag	14.517488	2.892313	9.135559
Ag	2.885365	2.856668	9.073247
Ag	5.816762	2.899689	9.094483
Ag	8.711403	0.002013	9.138617
Ag	11.615152	14.520681	9.140885

Ag	8.712119	2.904402	9.138358
Ag	11.617227	2.907732	9.145603
Ag	0.000010	5.807771	2.034995
Ag	2.903895	5.807771	2.035186
Ag	5.807105	5.807771	2.035167
Ag	0.000010	8.711704	2.035167
Ag	2.903914	8.711704	2.035909
Ag	5.807076	8.711704	2.035900
Ag	8.710667	5.807771	2.035900
Ag	11.614495	5.807771	2.035900
Ag	8.710667	8.711704	2.035900
Ag	11.614495	8.711704	2.035900
Ag	1.447171	7.261768	3.787859
Ag	4.357426	7.262250	3.793656
Ag	7.261417	7.264780	3.793754
Ag	1.445864	10.164183	3.788441
Ag	4.354192	10.163128	3.789904
Ag	7.263794	10.161514	3.783213
Ag	10.165499	7.261017	3.787296
Ag	13.063371	7.261759	3.786084
Ag	10.166953	10.166191	3.785808
Ag	13.064575	10.159119	3.786568
Ag	2.890418	5.818610	5.580771
Ag	5.812108	5.820049	5.590664
Ag	2.892740	8.713157	5.580067
Ag	5.807077	8.720313	5.584038
Ag	8.725389	5.817488	5.583660

Ag	11.616525	5.812651	5.588087
Ag	8.723653	8.724849	5.576964
Ag	11.613866	8.709593	5.581469
Ag	1.439415	7.255971	7.402112
Ag	4.332665	7.268860	7.376539
Ag	7.282758	7.293565	7.360482
Ag	1.441139	10.156860	7.376849
Ag	4.366265	10.159232	7.376517
Ag	7.274332	10.167032	7.385307
Ag	10.166925	7.274189	7.384940
Ag	13.067948	7.263520	7.393750
Ag	10.163130	10.161924	7.393483
Ag	13.048730	10.140931	7.377635
Ag	14.492253	5.814240	9.173859
Ag	2.872460	5.818638	9.165045
Ag	5.858842	5.822400	9.052834
Ag	0.001675	8.726019	9.163697
Ag	2.894387	8.725136	9.149029
Ag	5.807751	8.722155	9.133686
Ag	8.711080	5.813463	9.130062
Ag	11.593166	5.810807	9.144506
Ag	8.709327	8.714720	9.160438
Ag	11.615652	8.709227	9.161607
Ag	0.000010	11.615533	2.034995
Ag	2.903895	11.615533	2.035186
Ag	5.807105	11.615533	2.035167
Ag	0.000010	14.519161	2.035167

Ag	2.903914	14.519161	2.035909
Ag	5.807076	14.519161	2.035900
Ag	8.710667	11.615533	2.035900
Ag	11.614495	11.615533	2.035900
Ag	1.449355	13.062802	3.797417
Ag	4.354263	13.065263	3.797602
Ag	7.263736	13.064580	3.786069
Ag	10.166316	13.061970	3.786829
Ag	13.060502	13.063755	3.786415
Ag	2.901984	11.602297	5.585563
Ag	5.822475	11.605212	5.575883
Ag	2.898137	14.512157	5.592264
Ag	8.716939	11.612098	5.582654
Ag	11.610834	11.609268	5.587506
Ag	1.437819	13.037104	7.370258
Ag	4.371645	13.041767	7.368522
Ag	7.272956	13.053726	7.380945
Ag	10.163205	13.061014	7.388424
Ag	13.051936	13.066831	7.375177
Ag	14.467319	11.593538	9.112335
Ag	2.938778	11.563756	9.134524
Ag	5.834678	11.606617	9.153631
Ag	2.898154	0.065539	8.992571
Ag	8.717488	11.615323	9.162570
Ag	11.614588	11.612186	9.151425
Ag	14.500042	2.921477	5.571766
Ag	14.498746	14.509174	5.574838

Ag	14.516538	8.704420	5.584502
Ag	14.508093	5.818879	5.582576
Ag	14.500893	11.602902	5.581385
C	2.587821	11.281365	11.962830
C	3.605964	10.959048	12.806841
C	4.599811	11.894747	13.024892
C	4.522199	13.089544	12.379484
C	3.481009	13.391807	11.653256
C	2.498201	12.484054	11.441728
C	3.606213	9.799733	13.484612
C	4.510556	9.592530	14.459263
C	5.513081	10.511935	14.689676
C	5.552276	11.609573	13.919934
C	4.445270	8.494024	15.257398
C	6.385987	10.275235	15.702049
C	5.296782	8.310167	16.231860
C	6.276820	9.212058	16.455502
C	2.541503	5.547569	11.688814
C	2.093299	6.715252	12.231332
C	3.013917	7.705961	12.510519
C	4.315494	7.498188	12.161054
C	4.720863	6.340896	11.705991
C	3.829088	5.346129	11.486236
C	0.819713	6.923820	12.576723
C	0.425829	7.973968	13.311990
C	1.380278	8.910919	13.654150
C	2.640475	8.800848	13.193539

C	-0.834909	8.130901	13.790278
C	1.024440	9.920158	14.491233
C	-1.130970	9.113666	14.602048
C	-0.190588	10.012047	14.965890
H	1.829093	10.587572	11.796791
H	1.638771	12.764665	10.920408
H	5.216383	7.471219	16.842134
H	5.279053	13.787372	12.522398
H	3.404554	14.347813	11.236434
H	6.944892	9.064112	17.239358
H	7.134902	10.971188	15.884505
H	3.684995	7.803517	15.089140
H	1.868431	4.765689	11.553455
H	4.163739	4.405113	11.188541
H	-2.096529	9.196099	14.981474
H	5.002651	8.263366	12.321718
H	5.736238	6.175407	11.529018
H	-0.433550	10.774736	15.630718
H	1.751393	10.611392	14.769392
H	-1.561470	7.436452	13.525808
Br	6.922897	12.790852	14.141108
Br	-0.428381	5.699708	12.032102
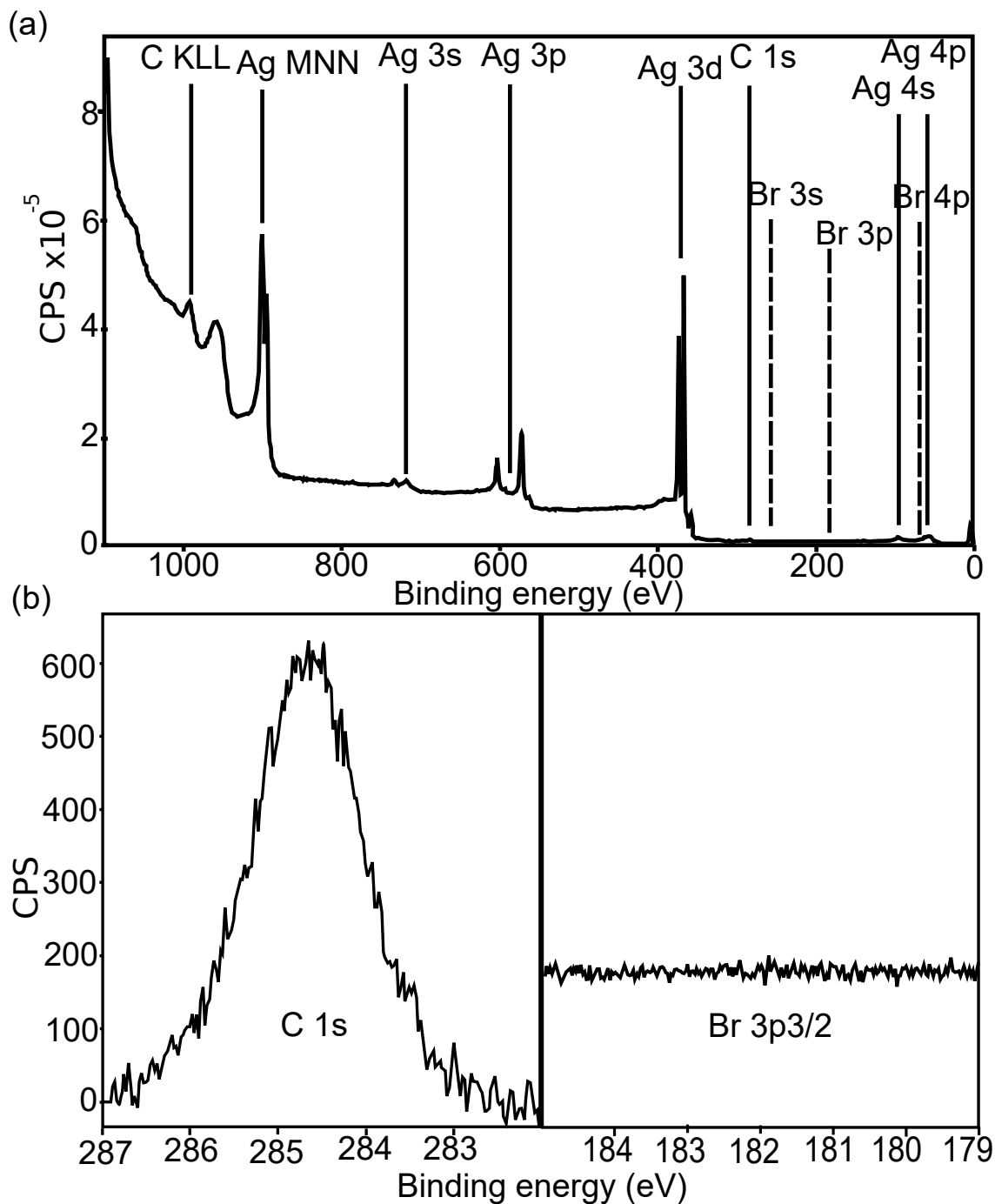
Figure 6.6: X-ray photoelectron spectroscopy collected for DBBA deposited on Ag(100) and then annealed to 470 K, showing the presence of submonolayer C and no detected Br.
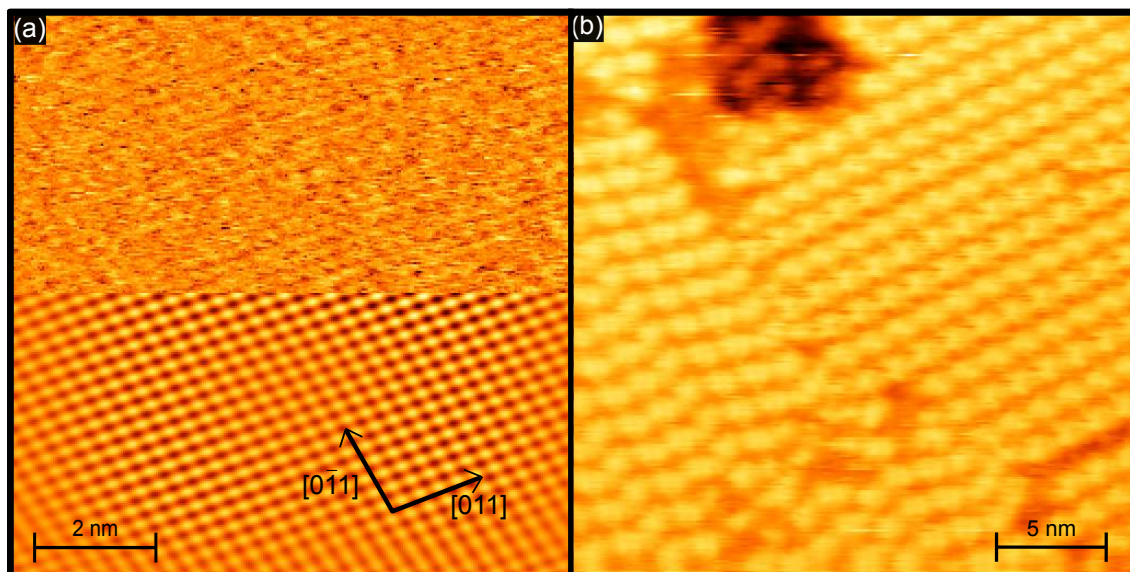
Figure 6.7: Left: atomic resolution data of a Ag(100) sample with a different azimuthal orientation to that in the Article. Half of the image is Fourier filtered to improve clarity. Right: Corresponding domain orientations of DBBA. Thermal drift is slightly different between topographs.

6.9 Errata

Clarification of: *"The scanner was calibrated with a single calibration coefficient measured at 10 nm scan range using the clean Ag(100) surface."* The STM scanner has a calibration coefficient for both the x and y axis (units of $V nm^{-}1$) - in doing our calibration we applied the same correction to both axes without treating them independently. The X and Y piezo response should be the same and thermal drift at RT negates correcting to greater precision.

Addressing: *"How was figure 6.2(b) corrected?"*: Thermal drift introduces skew distortion to the images. It is possible to correct data in images where two domains are present. These domains lie along the crystallographic axis of the substrate and so a skew correction can be applied to to ensure the molecular rows are orientated 90° to each other, as marked in the image.

Addressing: *No description of XPS setup in experimental procedure* X-ray photoelectron spectroscopy was collected on the same UHV system using a hemispherical analyser and an Mg filament ($E_x = 1253.6$ eV). XPS data was only collected following annealing the DBBA/Ag100 system and so no direct comparison can be made to DBBA/ag(100) following deposition.

Correction: *"In figure S2 in Supporting Information figure 6.7"* should read *"in Supporting Information figure 6.7"*

Correction: *"Orientation parallel to the nearest-neighbor axes ([011] and [0$\bar{1}$1]) fits better with the atomic resolution data shown in figure 6.1(a)."* should instead refer to figure 6.2(a). **Addressing:** *What is a situation for a molecule?*

This refers to a molecules relationship to the surface. It could otherwise be described as: we see in the STM images that a single molecule can align itself in one of four directions to the substrate, as opposed to four "situations". Because of the four fold symmetry of the system these situations are geometrically equivalent.

Addressing *"How can you be sure it's cyclodehydrogenation?"* **With respect to:** *the disordered material at step edges following annealing.* We cannot support the argument that cyclodehydrogenation and that the resulting planarisation of DBBA occurs based on our observations alone, following annealing to 470 K. Instead this should be an inference that this might have happened based on the behaviour of DBBA atop Ag(111) where cyclodehydrogenation, but not polymerisation occurs at 450 K [33].

Addressing: *"How can you be sure of planarisation and how can you exclude dehydrogenation at an external peripheral H, followed by polymerisation / c-c bond formation of molecules that might not be fully planar?* **With respect to:** *"The linear features are essentially flat. This is expected if the DBBA dehydrogenates to form nanoplatelets prior to polymerisation."* "Prior to polymerisation" has been

poorly worded and suggests that cyclodehrdogenation must occur prior to polymerisation. This is not the case - on Ag(111) planarised / cyclodehydrogenated DBBA occurs prior to polymerisation [33], whereas on Au(111) [9], Au(110) [15] and Cu(111) [16] DBBA can polymerise and *then* undergo cyclodehydrogenation. Atop a range of surfaces, polymerised DBBA that is not cyclodehydrogenated has a clear "zig-zag" motif evident in STM images even at poor resolution, examples are presented in figure 6.8. We suggest that cyclodehdrogenation has occured because the linear features / ribbons we see appear to be flat lying i.e without this zig-zag motif corresponding to the raised acene edges. We would ideally do additional studies at a range of temperatures to confirm cyclodehdryogenation supported by XPS. C-C bond formation between neighbouring DBBA molecules as a route to polymerisation is possible as has been seen on other surfaces [125]. The branching / networked nature of the polymerised DBBA in our work suggests other processes beyond end to end Ullmann coupling might be occurring.
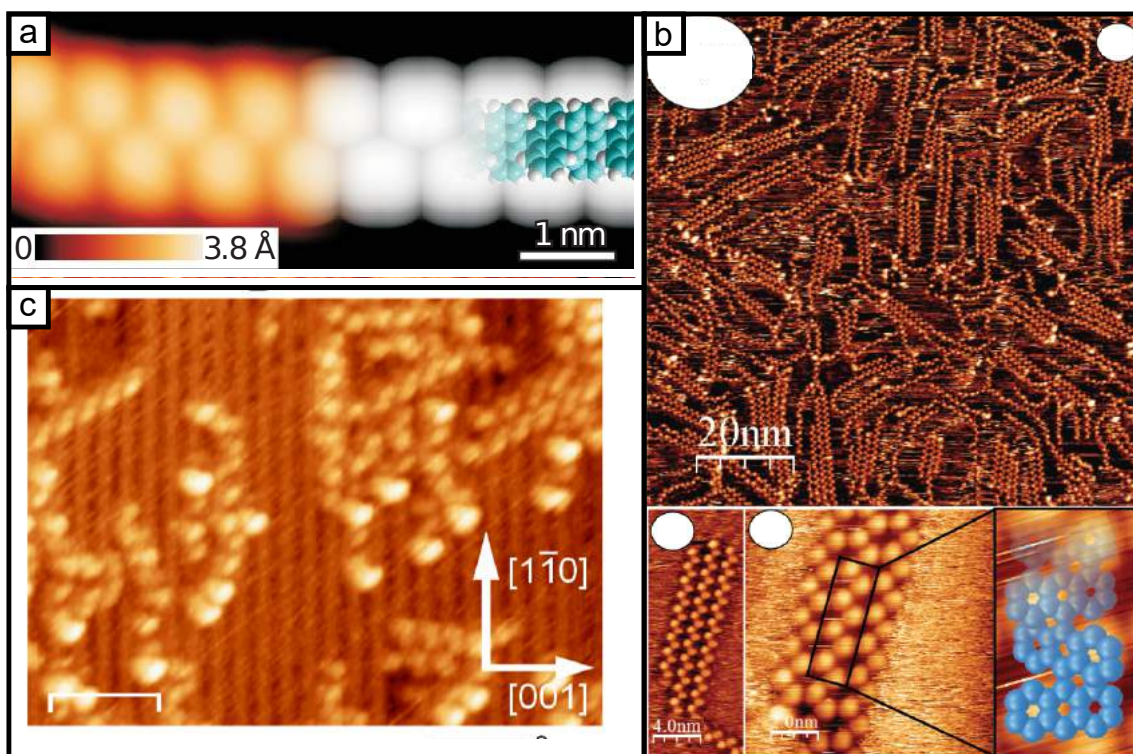
Figure 6.8: a) Polymerised DBBA/Au(111) after annealing to 473 K, adapted from [9]. b) Polymerised DBBA/Cu(111) after annealing to 373 K, adapted from [15]. c) Short chains of polymerised DBBA/Au(110) following annealing to 400 K, adapted from [16].

7

Perfluoropentacene on Cu(111)

7.1 Abstract

Perfluoropentacene (PFP), an n-type organic semiconductor, is deposited at mono-layer and bilayer coverage on Cu(111). Scanning tunneling microscopy at various bias voltages is used to investigate the geometric and electronic structure of the layer. The appearances of the first layer and second layer differ, probably because of perturbation to the first layer electronic structure by the substrate. This has been previously observed for pentacene (Pn), the isostructural p-type organic semi-conductor. The PFP film has a unit cell of (4, -3,3 4) relative to the substrate, which is larger than that of Pn/Cu(111), representing a half-integer increment in each direction.

7.2 Introduction

PFP is a linearly-bonded chain of five benzene rings, terminated with F atoms [87]. Its cousin pentacene (Pn), which is terminated with H atoms, is a p-type organic semiconductor [87, 143, 144] that is used in organic solar cells and other molecular electronics due to its high hole mobility [145], stability during atmospheric operation
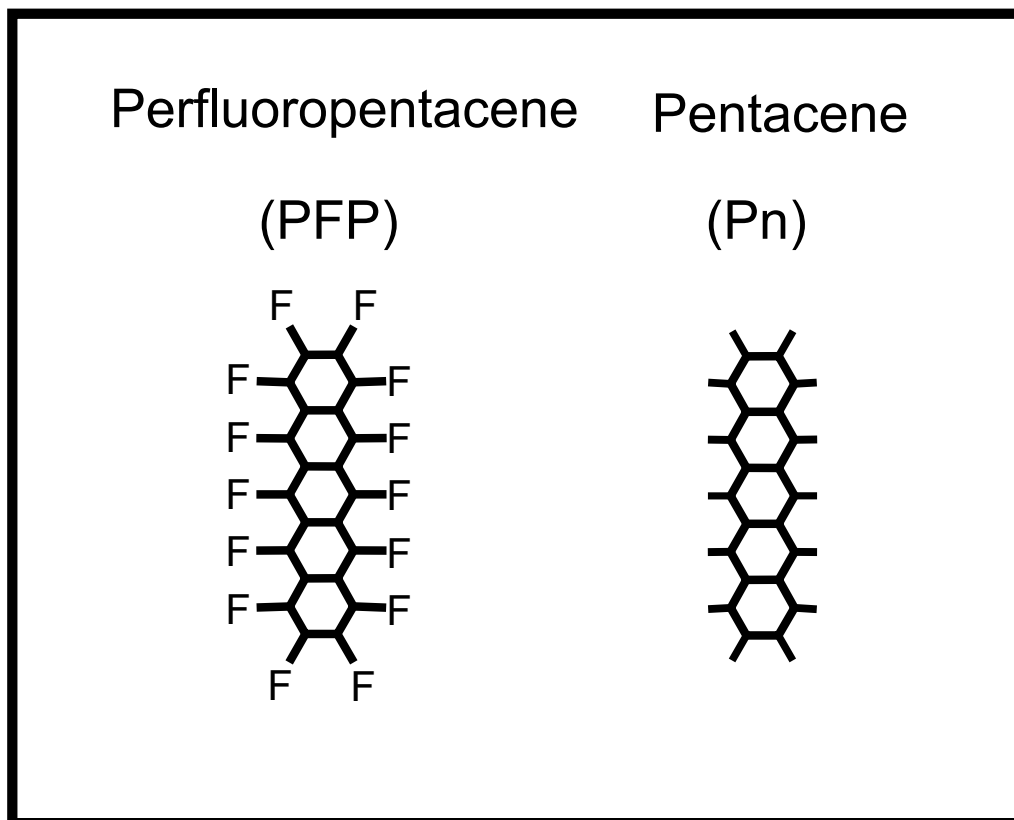
Figure 7.1: Structural illustrations of PFP and Pn, note the slightly larger profile of the former.

[146] and the strength of molecule–molecule interactions which make it suitable for self assembly applications and high quality crystal growth. The structure of both PFP and Pn are presented in figure 7.1.

The electronic structure of organic semiconductors is strongly affected by the ordering of the molecular crystal [147]. The electronic behaviour of organic *devices* is to a large extent governed by, or at least subject to, the quality of the interfaces between organic material and metallic interconnects. Molecular adsorption on ideal metal surfaces provides useful model systems for the study of both of these types of phenomena. For example, Pn, a relatively simple molecule, has complicated behaviour and several different growth modes arising from the competing interactions between neighbouring molecules and the substrate on which they are adsorbed [148, 149]. Organic semiconductors have several benefits compared to inorganic

semiconductors, such as flexibility, transparency and non-toxicity [150]. Exploiting their unique properties such as low film thickness and accompanying short transport distances can yield devices with short response times for high frequency applications [68]. Tuning of the HOMO and LUMO energy levels in organic systems, akin to engineering the valence and conduction bands in traditional semiconducting systems, is key to optimising device efficiency. Halogenation and fluorination in particular have been explored as mechanisms to achieve this [151, 152, 39]. While development of organic electronic and optoelectronics has brought some devices to market (OLED and OFET) efficiency is still a barrier in many applications [65, 150]. The efficiency of a molecular system is dependent on a range of interacting properties such as substrate surface contact resistance, adsorption geometry [153] and the degree of order. Limited quality of ordering is a weakness inherent to molecular electronics over conventional semiconductors [68].

Coinage metals Au, Ag and Cu [49, 154, 155] are of interest, as they are widely used in electronics [19, 156]. Pentacene has the strongest interaction with the Cu(111) surface, followed by Ag(111) and then Au(111) [49]. In the latter cases, the diffusion of sub-monolayer Pn is observed [157]. Atop Cu(111), Pn interacts strongly, with substantial charge transfer leading to large differences in appearance and electronic structure upon adsorption [19]. On weakly interacting surfaces, the inter-molecular interactions usually dominate and result in Pn adopting a standing herringbone structure [148].

In an earlier study by Smerdon *et al.* the electronic behaviour of Pn is demonstrated, Pn forming one-half of a high-performance molecular Schottky diode with C_{60}, doped via its interaction with Cu(111) as the metallic contact [158]. On Cu(111) random tiling, herringbone close packing and further close-packed linear islands stabilized by bilayer (BL) growth have all been observed at different coverages and deposition temperatures [19, 148].

As a result of fluorination, PFP differs in one additional major aspect from Pn: it is an *n*-type semiconductor [87]. Both Pn and PFP adopt herringbone packing in the bulk, albeit with different lattice parameters and angles [87, 19]. In principle, the structural similarity between bulk Pn and bulk PFP suggests the possibility of intermixed molecular crystals, or of effective doping by one with the other. Some studies exist that show apparently effective intermixing, though only for 1:1 mixtures [159] [149]. PFP has also been studied on Au(111), Ag(111) and Cu(111) metals at monolayer, bilayer and multilayer coverages and in general adsorbs more weakly as compared to Pn [157] [160]. It has also been investigated as a monolayer (ML) and BL atop SiO_2 and graphene atop SiO_2 [161], forming a vertical herringbone and a planar structure, respectively. These studies highlight the importance of in depth characterization of the interface structures due to their influence on molecule-molecule interactions and the resultant electronic properties of the system.

The structure of PFP/Cu(111) has been investigated at room temperature and following annealing at both bilayer and monolayer coverage [17, 162]. Glowatzki *et al.* report that up to and including monolayer coverage the PFP adsorbs in a disordered fashion at room temperature and behaves as a 2D liquid, unresolved via STM due to its rapid diffusion across the surface (other than at step edges and defects [17]). The 2D liquid behaviour reported at RT is consistent with the behaviour of Pn on Ag(111) at RT [163] [17].

Variable temperature studies of PFP on Ag(111) have characterized it as a structurally strained system due to the substrate geometry. At RT, PFP forms an ordered layer of unbroken rows of molecules which each exhibit a moiré pattern, repeating every 8 molecules. The moiré pattern shows that in this case each molecule has a slightly different, strained, registry with the substrate.

When cooled to 90 K, PFP/Ag(111) reorders to a layer of slightly lower density, in which there is no moiré pattern but instead a structure in which the row structure

is broken by a dislocation every 6 molecules [164]. This dislocation pattern lifts the strain and places each molecule in the same registry with the substrate.

PFP forms 6 domains on this system at each temperature, with $3\times$ rotational degeneracy due to the substrate symmetry and $2\times$ chiral degeneracy due to the moiré pattern at RT, or alternatively the row staggering at 90 K.

In general, two competing interactions dictate PFP adsorption: the strong attraction of the central acene rings to the substrate and a repulsion between F atoms [165] and the substrate. This phenomenon introduces a bowl-like adsorption conformation with upwardly-curved molecule edges [165, 153, 162] and suggests that the molecule–substrate adsorption distance is increased by the shape of the 2p orbital of terminal F atoms compared to the 1s orbital of terminal H in pentacene [153]. An increased molecule–substrate separation leads to reduced orbital hybridisation and reduced HOMO/LUMO broadening as a result [153].DFT simulations have explored variably fluorinated Pn molecules, in particular F_4Pen, tailoring F presence as a tool to control the electron injection barrier; the addition of fluorine lowers the molecular HOMO energy [166]. Partial fluorination has been shown to improve crystalline ordering and transport efficiencies in pentacene derivatives [152, 39]. PFP has been used in OTFTs with carrier mobilities comparable with Pn OTFTs [166] but, as of writing, p-type OTFTs are outperforming n-type OTFTs in this area [90]. Development of equally efficient n-type OTFTs is necessitated by the use of both in CMOS applications [91], bipolar transistors [157] and complementary or ambipolar circuits [166] which are of particular interest in efficient logic gate design [167]. Ambipolar devices are those capable of both electron and hole transport, effectively a superposition of p and n type devices, which can be facilitated by the presence of both electron donor and acceptor moieties within a molecule or crystal structure [168].

In this work we investigate the monolayer and bilayer structures of PFP on Cu(111) at 50 K. Elucidating the geometry of these systems is an important step

towards understanding the interactions that govern their electronic properties and therefore applications in devices.

7.3 Experimental procedure

All measurements are taken at Argonne national labs, Illinois, using a commercial Omicron variable temperature STM, under ultra-high vacuum conditions (UHV) with a base pressure in the analysis chamber at 5.0×10^{-10} mbar and at 6.0×10^{-9} mbar in the sample preparation chamber. The Cu(111) crystal was prepared through overnight sputtering with Ar^+ ions at 1.5 keV and simultaneous annealing to 900 K. The duration of this was not precisely controlled but lasted at least 8 hours. Following the overnight sputter and anneal the system was then treated with a 30 minute anneal at 900 K prior to work taking place.

PFP was evaporated from a Dodecon four-cell organic molecular-beam epitaxy source at 480 K. Prior to each deposition the source was out-gassed at 450 K. The Cu(111) sample was at RT throughout the deposition process. Deposition was carried out for 10 minutes. This resulted in sub-ML coverage and repetition produced a partial BL. Both of these systems were characterised using STM with a mechanically cut PtIr (90:10) tip.

Scanning tunnelling microscopy is performed in 'constant current' mode. The signal in the I channel is therefore related to the differential of the Z channel, and sometimes provides images with clearer detail. Where these are presented, they are identified as $I_{TC}(x, y)$ images.

7.4 Results

PFP was deposited atop clean Cu(111) to bilayer coverage, as described above, before insertion into the STM and cooling to 50 K. Figure 7.2(a) shows simultaneous

resolution of both BL and ML. In figure 7.2(c) two BL islands are observed, one on each side of a Cu step edge.

Monolayer and bilayer PFP are structurally similar; both have the same 2D lattice parameters. Molecular rows in the BL run along those beneath them in the ML but these are offset by approximately half a molecule so that BL molecules are centered between the molecules in the ML row beneath them. In the $I_{TC}(x, y)$ image in figure 7.2(b), lines are superimposed on molecules in each layer, with the green series over the long axes of BL molecules and the blue series over similar locations in ML molecules. This structure is seen consistently across domains independent of scan direction. This half-molecule offset between the BL and ML molecular rows as also observed for Pn/Cu(111) [19].

7.4.1 ML and BL domains

The behaviour of Pn atop Cu(111) and the similar anisotropic nature of PFP lead us to expect that the PFP molecules adsorb with a long axis coincident with a substrate NN axis. We confirm this independently by comparison between images such as in figure 7.2 and images of C_{60} adsorbed atop the same substrate (see Supporting Information (SI)).

The three fold nature of the substrate means that molecules within a domain are aligned in 1 one of 3 directions, 120° apart, as seen in the angular separation of two domains marked in figure 7.2(b). Interestingly, while the molecular long axes are aligned with substrate axes, the *domain* directions (i.e., the row structures) are not; lines drawn over equivalent sites in molecules in a domain are not parallel with substrate axes. Molecules within a domain instead form staggered arrangements in both (inter-row and intra-row) directions: neighbouring molecules both within and between rows are offset from each other such that equivalent sites in such molecules occupy sites on *adjacent* NN rows of substrate atoms. Although the symmetry

of the domains is dictated by the substrate lattice the angle of the domain rows is a result of the magnitude and direction of the staggering offset. There is no energetic preference for a particular staggering direction, therefore we expect chiral degeneracy is introduced, leading to 6 inequivalent domains at both ML and BL coverage, though we have not observed all of these.

Comparing the appearance of the molecules in figure 7.2(a) with the orbital shapes presented in figure 7.4(a) BL molecules apparently tilt about their long axis, like glowatzki *et al.* report [17], but this apparent tilting is dependent on scan parameters. This is discussed further in the SI of this chapter but the PFP orientation with respect to the surface normal cannot be determined reliably through STM.

Glowatzki *et al.* report diffusion of PFP across the Cu(111) surface at RT for coverage less than a bilayer. Clearly, an ordered bilayer with domain symmetry originating in the substrate requires an ordered monolayer. They suggest the bilayer locks the first layer into registry. Behaviour similar to this for has been previously reported for Pn/Ag(111) at RT [155], and Pn/Cu(111) [19]. At 50 K we directly resolve the ML alongside the BL as in figures 7.2(a) and 7.2(b). Resolution of the monolayer is also possible, independent of the bilayer as presented in the SI. In figure 7.2(b) the structure of both the ML and BL break down towards the Cu step edge. Disordered regions are visible in the monolayer regions, but are not observed in the bilayer.

7.4.2 Determining the BL and ML structure

When scanning at negative bias, occupied states of the PFP molecules are imaged. In Figures 7.2(a) and (b), the well-defined lobes relating to the HOMO structure of isolated PFP are evident in the BL region of the topography. The same is true for the BL data presented in and figure 7.3(a), where a simulated HOMO charge
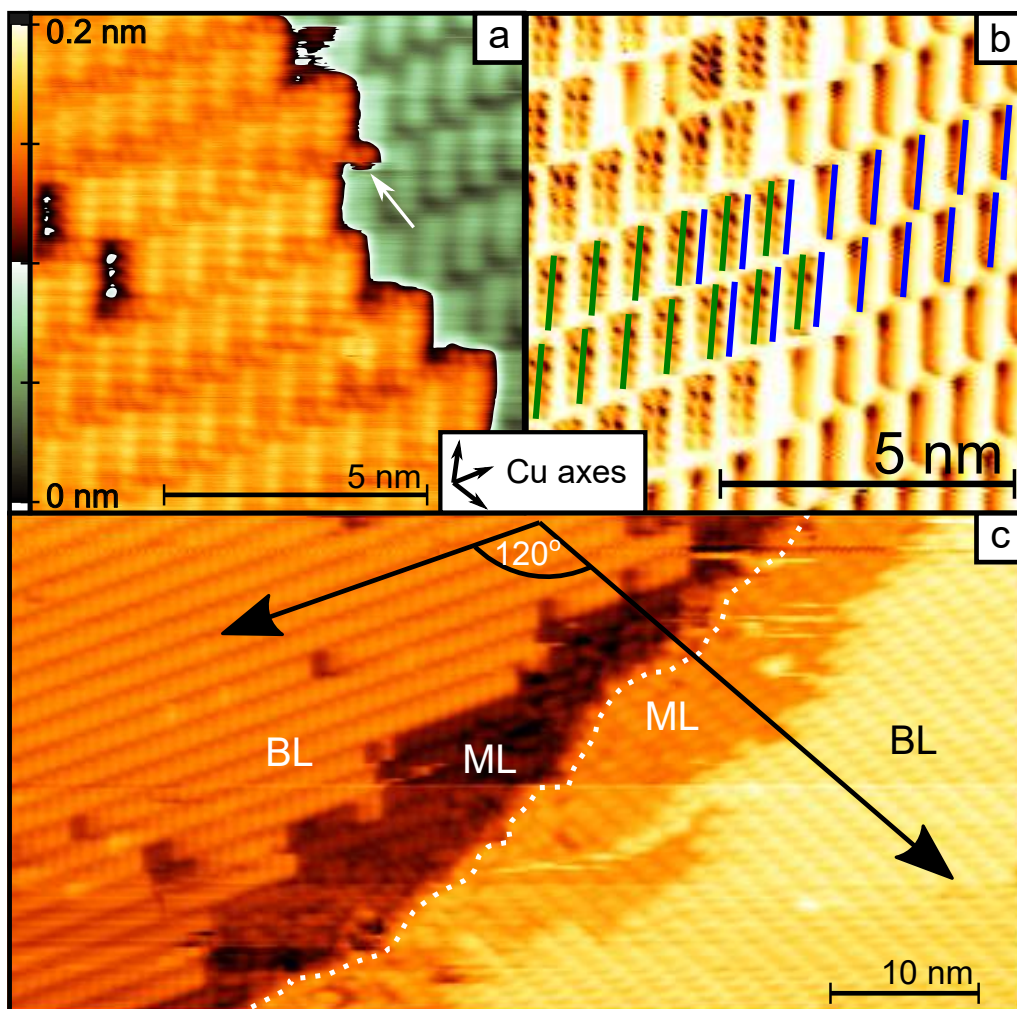
Figure 7.2: a) STM topograph of a PFP bilayer boundary region ($I_T = 100$pA, $V_B = -2.5$ V). The bifurcated lobes of the bilayer molecules are evident on the left hand upper $\frac{1}{3}$ of the image. A tip change occurs $\frac{1}{3}$ of the way down the image, giving the molecules below the change the appearance of a central bright chain in this region as in the results of Glowatzki*et al.* [17]. An arrow indicates a molecule that has apparently changed position during the scan (discussion in text). b) A $I_{TC}(x, y)$ image over a similar BL/ML step. The difference between the orbital shapes is emphasised in this scan. The long axes of the molecules in the BL and ML are marked to illustrate the half-integer unit cell offset between them ($I_T = 100$pA, $V_B = -2.5$V). c) Two domains of the PFP BL separated by a Cu terrace ($I_T = 100$pA, $V_B = -3$V).
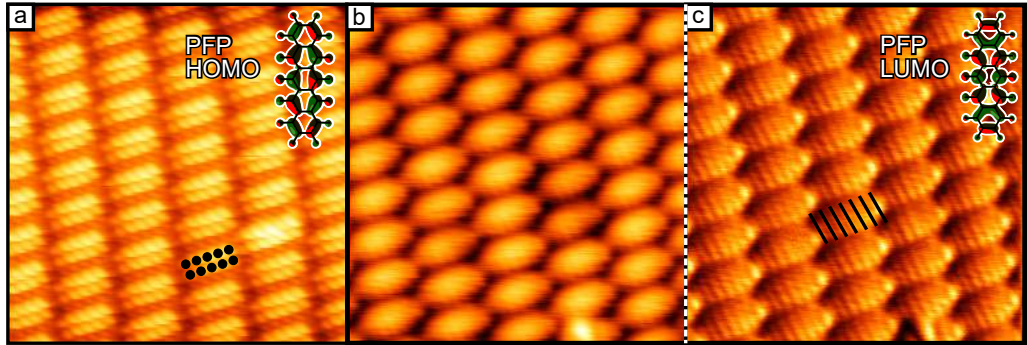
Figure 7.3: a)Molecules within the PFP BL when imaged at negative bias ($I_T = 50\text{pA}, V_B = -1$ V). The molecules have two sets of 5 lobes bifurcated along their long axis, these lobes are marked in black in one instance. The HOMO charge isosurface of an isolated PFP molecule is provided for reference as an insert, adapted and reproduced from [18]. b) Molecules within The PFP BL when imaged at positive bias ($I_T = 50\text{pA}, V_B = 2$ V). c) An $I_{TC}(x, y)$ image corresponding to the topography presented in (b) to better identify lobe features in the molecule ($I_T = 50\text{pA}, V_B = 2$ V). The molecules have 7 lobes across their long axis marked in black. The LUMO charge isosurface of an isolated PFP molecule is provided for reference as an insert, adapted and reproduced from [18].

isosurface, altered and reproduced from [18] has been included for a direct comparison. When tunnelling at positive bias the unoccupied states of the PFP molecules are imaged and in the $I_{TC}(x, y)$ image presented in figure 7.3(c), corresponding to the topography of figure 7.3(b), we see features similar to the LUMO structure of isolated PFP molecules.

In figure 7.2(a) and (b) the ML is seen to consist of featureless 1D rods. This is consistent across scan independent of tunneling parameters. The different appearance of the BL and ML molecules indicates a difference in electronic structure.

Based on similar ML and BL behaviours observed for Pn/Cu(111) by Smerdon *et al.* [19], we suggest that the first layer of PFP molecules likely participates in charge transfer with the substrate in a similar fashion. This behavior arises when the LUMO of the molecular overlayer is broadened through adsorption, including the Fermi energy of the substrate [169, 65]. This results in partial filling of the LUMO and charge transfer between the substrate and the ML, leading to a Fermi

surface in the molecular layer and a degree of metallic conduction [170, 171, 172].

The preferred PFP adsorption site on the surface could not be directly determined through our STM data as we do not have atomic resolution on the clean Cu(111) surface. For Pn/Cu(111), STM measurements in reference to Cu adatoms found that a Pn molecule adsorbs with its central benzene ring over an hcp hollow site [48] with the long axis of the molecule aligning with the NN axes of the substrate. This adsorption pattern is consistent with similar polyaromatic molecules on the close packed surfaces of coinage metals. As previously noted, PFP adsorbs similarly to this with its long axis aligned with the NN axes of the substrate. Koch *et al.* find that PFP distorts upon adsorption of Cu(111) so that the C core of the molecule is closer than the F fringe, the latter bonding distances being elongated [162].

These observations are consistent with the π system of the PFP ML being the dominant component in the molecule–substrate interaction, as was also seen with Pn. From this similarity the assumption follows that PFP and Pn adsorb similarly atop Cu(111): with their benzene rings centred on Cu(111) hcp hollow sites.

Figures 7.4(b) and (f) show molecules imaged at negative bias appearing with 5 wide lobes across their length consistent with the simulated homo structure in figure 7.4(a) .It is difficult to resolve the bifurcation of these lobes in figures 7.4(b) and (f) but it is present having checked the $I_{TC}(x, y)$ channel, as with figure 7.2(a) and (b). The lobes in molecules are seen to line up somewhat across neighbouring molecules. This provides a major constraint in determining the relationship between one molecule and its neighbours within a row. The alignment of orbitals in adjacent molecules indicates inter-molecular alignment of terminal F atoms, which is in contrast to observations of interleaving of F atoms reported for PFP/Ag(111) [164]. From this conclusion, the only structure that produces this F arrangement while avoiding a non-physical molecular separation is the (4 -3,3 4) structure presented

134
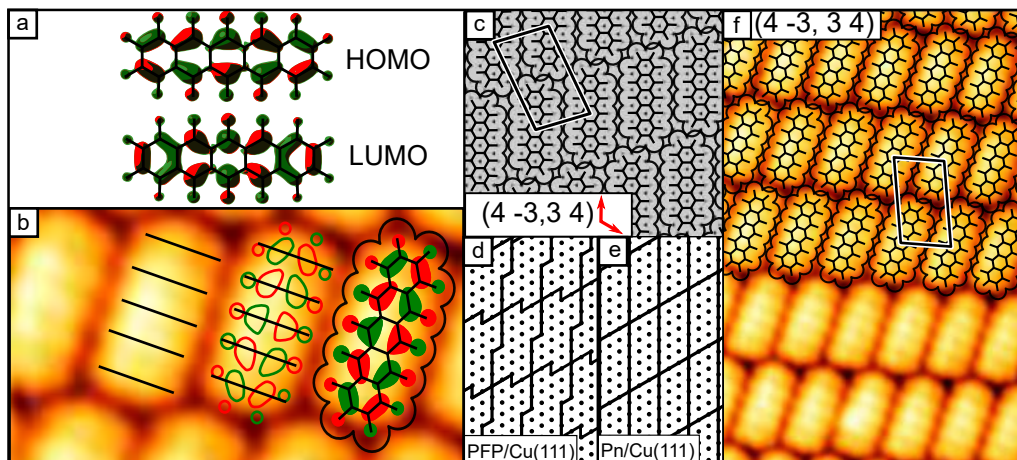
Figure 7.4: a) Charge isosurfaces of PFP HOMO/LUMO states adapted from [18]. b) A structural model of the PFP molecule scaled to the HOMO identified in the data. This is overlain onto an image the bilayer (I_T =50 pA, V_b =-2 V) c) The (4 -3,3 7) structure for the PFP ML and BL as determined from the data presented as a wire model with the van der Waals radii of each molecule. d) The 'staggered' (4 -3,3 7) adsorption motif observed for PFP/Cu(111) vs e) the 'straight' ordering of Pn/Cu(111) [19] f) The PFP model is superimposed atop high resolution data of the BL. (I_T =50 pA, V_b = -2 V)

in figure 7.4(c) and superimposed onto the data in figure 7.4(f). This alignment of F atoms for Cu(111) as opposed to the interleaving observed on Ag(111) is a consequence of the reduced atomic separation on the Cu(111) to Ag(111). Inspection of figure 7.4(c) shows that a PFP arrangement that results in interleaved F atoms would require PFP molecules overlapping or having a large gap between each other in their short axis. The Pn/Cu(111) structure is (3 3,0 6) [19]. This is a closer packed structure, by $\frac{1}{2}$ of a NN in each direction. Each molecule is separated from its neighbours by several Cu NN distances, but the centre of every molecule in a domain is connected to the centres of its neighbours by the same substrate atomic rows. The larger van der Waals radii of the F atoms in PFP force the looser (4 -3,3 4) packing. The half-integer nature of the expansion forces the F atoms into approximate in-phase registry *and also* means that every adjacent molecule is on a different set of substrate rows. This means that there are no straight lines of

system	a (nm)	b (nm)	θ (°)	Area (nm^2)	Density (nm^{-2})
Glowatzki PFP description	1.0	1.75	92	1.75	0.57
Our PFP description	1.04	1.75	99.2	1.81	0.55
Pn	0.77	1.54	60	1.02	0.98

Table 7.1: The unit cells of the PFP/Cu(111) as reported here, in the work of Glowatzki *et al.* [17] and the Pn/Cu(111) system reported by Smerdon *et al.* [19].

molecules. Every line is staggered compared to the substrate, as shown in figure 7.4(c).

Taking the resulting structure of (4 -3,3 4) with respect to the surface NN distance, the equivalent ML and BL lattice parameters are therefore $a = 1.04$ nm, $b = 1.76$ nm, $\theta = 99.2°$, as presented alongside the Pn/Cu(111) in the table above. We do not present associated errors on these values because they are derived from the Cu lattice constant. These measurements show good agreement to those observed by Glowatzki *et al.* [17], who use LEED and STM to measure the structure, reporting the surface mesh of the bilayer as $a = (1.75 \pm 0.05)$ nm, $b = (1.0 \pm 0.1)$ nm, $\theta = (92 \pm 1)°$.

The major difference between our description and this is the angle of the unit cell, likely due in part to the thermal drift that usually confounds STM measurements. The Glowatzki model avoids the approach of making arguments based on the structure of the substrate, instead presenting direct measurements from STM and LEED.

Glowatzki *et al.* propose that the appearance of the BL as seen in their data arises from a tilt about their long axis and suggests an offset staggering between the BL and the ML as the structure facilitating this, similar to the bilayer structure observed on Ag(111) [154] and our earlier study of Pn/Cu(111) [19]. This structure would serve as an intermediary between the herringbone stacking seen in the bulk and in thick multilayers and facilitates maximum contact between the electronegative F atoms of one layer and the π systems of the other.

A tip change occurs $\frac{1}{3}$ of the way into the (downward) scan shown in figure 7.2(a), resulting in the bilayer molecules adopting two different appearances. One is of a flat lying molecule that fits the HOMO model in figure 7.4(a) and the other appearing as the tilted structure of Glowatzki *et al.* at room temperature [17]. The tip change we observe coincides with the disappearance of a partially imaged PFP molecule from the bilayer; it seems reasonable to assume this has been adsorbed to the tip.

The effect of a molecule adsorbed on the tip is difficult to assess due to the unknown geometry of the arrangement [173, 174]. However, in this instance, it produces a scan very similar to that reported for PFP/Cu(111) by Glowatzki *et al.* [17] in their analysis of the 'tilt' of the molecules.

7.5   Conclusions

The PFP monolayer and bilayer structures atop Cu(111) have been elucidated. Monolayer and bilayer PFP adopts a flat lying (4 -3,3 4) structure at 50 K. Based on the difference between simultaneous observations of molecules in the first and second layers, it is clear that the electronic structure is modified, which we propose is due to charge transfer from the metal substrate in a manner similar to Pn on Cu(111) [19]. The BL exhibits clearly resolved orbitals at a range of scanning biases and depending on the tunnelling bias we see features that mimic both the HOMO and LUMO features expected of an isolated molecule, separately. This suggests the semiconducting properties of the BL molecules are unchanged.

The row structure is not aligned along substrate NN rows, as for Pn on Cu(111) [19, 157]. The larger 'footprint' of PFP forces the unit cell to increase in size by $\frac{1}{2}$ a Cu NN distance in each direction. To maintain the same registry between molecules and surface sites, each adjacent row of molecules is displaced by a substrate atomic row in both directions, leading to an overall kinked appearance of the molecular

rows.

Bulk PFP has a larger unit cell than bulk Pn and this difference is exaggerated in the case of flat lying PFP/Cu(111) compared to flat lying Pn/Cu(111) and so as thin films these molecules are less structurally similar. We do not see the same variety of phases as has been observed for Pn/Cu(111) [19] although we have not investigated sub-monolayer coverage in this work. Symmetry arguments indicate that, at least to bilayer coverage, the film forms as one phase with six possible domains, as a result of two-fold mirror symmetry of PFP rows combined with three-fold rotational symmetry of the substrate.

7.6 Supplementary information

7.6.1 The Cu(111) lattice

As stated in section 7.4 and encountered in other works [48], it can be difficult to resolve individual atoms at the Cu(111) surface due the closeness of their packing. Determination of the crystal axes was achieved via adsorption of C_{60} atop Cu(111). By annealing C_{60}/ Cu(111) to 525 K the p(4×4) surface reconstruction is induced [175] as in figure 7.5, from which the Cu(111) lattice axes can by determined by proxy. The C60 NN directions lie parallel to those of the substrate. The Cu sample in our work is a single crystal and maintained in the same orientation through out.

7.6.2 The monolayer

Stable ML formation is seen to occur at 50 K with large domains (figure 7.6(b)). Compared to the BL molecules we see a plain rod appearance at smaller positive biases (figure 7.6(a)) and increased defect densities within the ordered structure. At higher negative biases we see the featureless appearance of ML PFP adopts a lobed motif like the BL.
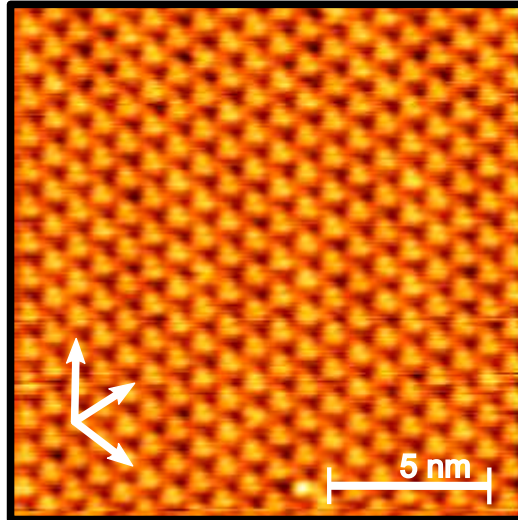
Figure 7.5: $(I_T = 400\text{pA}, V_B = 1.5\text{V})$, $C_{60}/Cu(111)$ with the C_{60} adopts a p(4×4) following annealing. The white vectors denote the C_{60} and $Cu(111)$ lattice axes
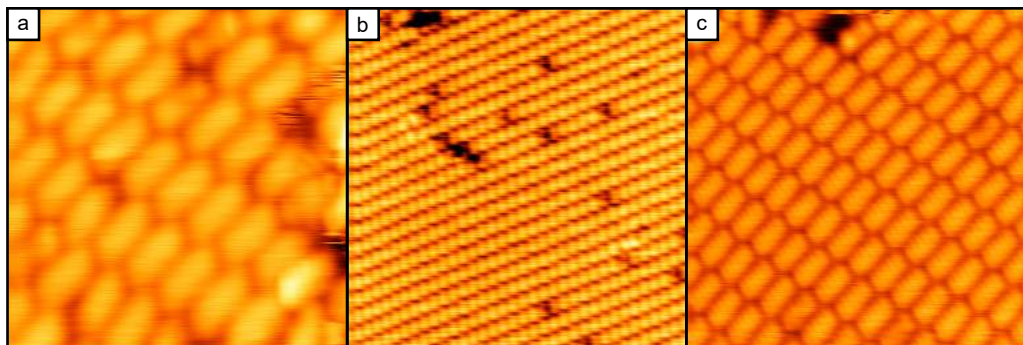
Figure 7.6: a) A close up of the monolayer showing the smooth appearance characterising it $(I_T = 100\text{pA}, V_B = 1.5\text{V})$. b) Large ML domains $(I_T = 200\text{pA}, V_B = -3.0\text{V})$. c) At high negative biases we see the ML adopts a lobed appearance like the BL $(I_T = 200\text{pA}, V_B = -3.0\text{V})$

7.6.3 Tilt and tip interactions

The appearance of PFP molecules in the STM data we present varies, predominantly appearing flat lying but occasionally tilted. This variation we attribute to being a scanning artefact and the following discussion demonstrates why STM is not a suitable technique for determining the molecules orientation with respect to the surface, by appearance alone. Glowatzki *et al.* suggest that PFP is tilted based on the appearance of the molecules during STM and so we also address this result directly with relation to our own data and a simplistic double tip simulation. The STM data of Glowatski *et al.* in figure 7.7(c) appears influenced by the adsorption of a molecule on the tip [17]. We infer this from the differing appearances of the BL in the data we have presented in figure 7.2(a). Close ups of the bilayer before (figure 7.7(a)), and after (figure 7.7(b)) a tip change occurs have been presented for comparison with the simulated structure Glowatzki *et al.* ascribe to a tilted PFP molecule in figure 7.7(d)) [17]. The raw data glowatzki attempts to model with this tilted PFP model (figure 7.7(c) and d respectively), strongly resembles the PFP molecule we have imaged following a tip change in figure 7.7(b). This casts doubts on their assertions that the PFP molecules in the bilayer are tilted, which is based chiefly on the molecules appearance via STM.

In figures 7.7(e-g) we demonstrate how a double tip imaging a simplified structure based on the PFP molecules we see in figure 7.7(a) would result in molecules with features similar to those we see after the tip change in figure 7.7(b) and the stm data of glowatzki *et al.* in figure 7.7(c). Because the tip change between 7.7(a) and (b) coincides with a molecule disappearing from the BL (see figure 7.2(a)) we suggest this PFP molecule adsorbs to the tip to produce this particular double tip motif. An adsorbed PFP molecule being the cause would explain why the same motif occurs by chance in both ours and the Glowatzki *et al.* result.

Multiple competing tunnelling contacts effectively reduce the resistance of the
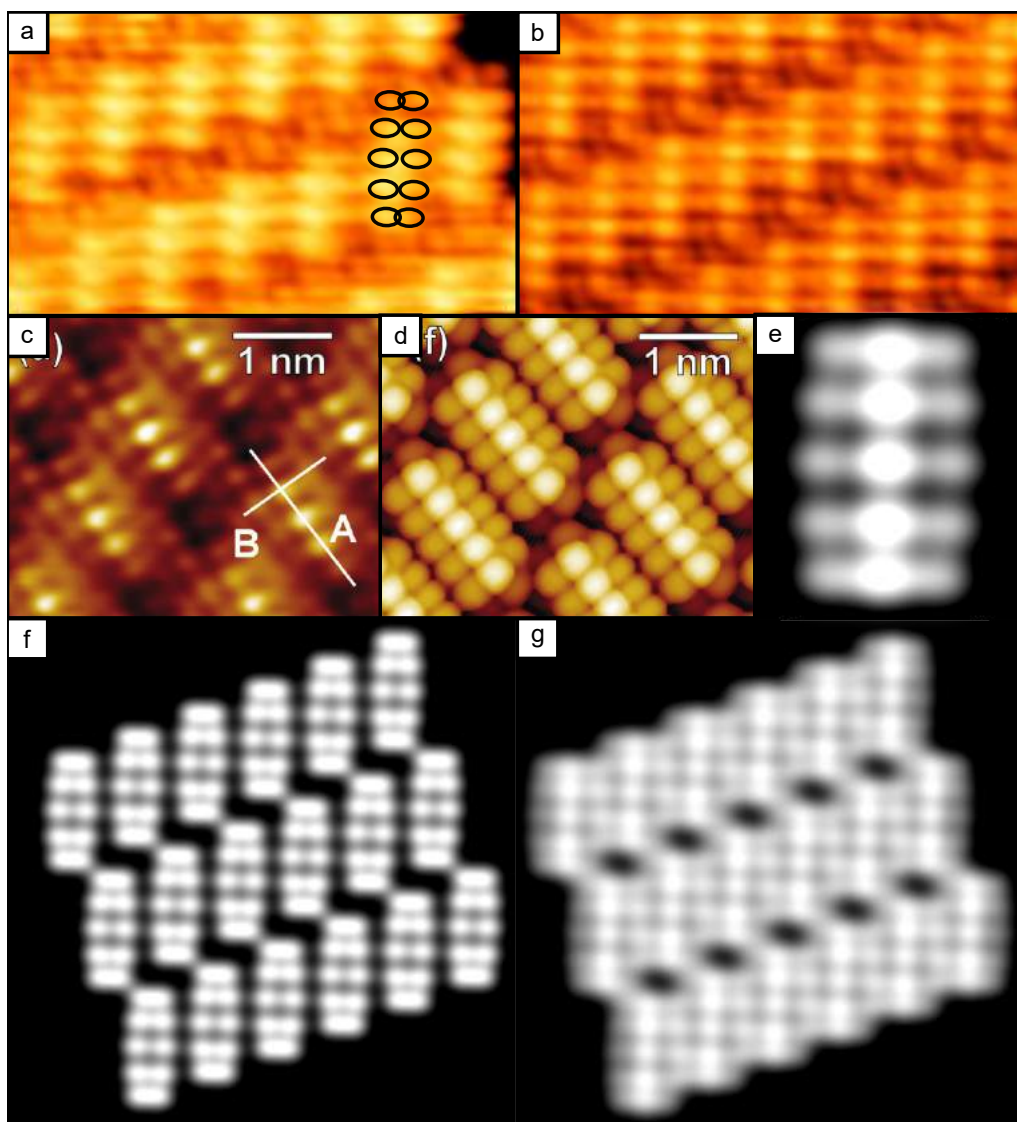
Figure 7.7: (a-b) Magnified regions of our data presented in figure 7.2(a), (c-d) reproductions from Glowatzki *et al.* [17]. (e-g) Images to explain our simplistic double tip simulation. a) PFP reflecting the lobed HOMO structure, black rings Illustate a template structure derived from this b)the same BL region following a tip change c) The Glowatzki *et al.* STM data following correlation averaging [17] d) the titled PFP model proposed by Glowatski to explain the motif seen in (c). e) The molecular motif antici-pated for a double tip separated by the molecules half width perpendicular to its long axis. This is created by the supposition of the motif in (a). f) BL model created from the molecule template of (a) g) The BL model resulting from the double tip superposition.

vacuum gap and the two tunnelling regions create a superposition of the surface features, offset by gap between the double tip. For the purposes of this exercise we consider the case where this offset is the half-width of the molecule. This would be the case in a molecule adsorbed to the tip in such a way as to approach the surface end on. The effect of this supposition on an individual molecule is seen in figure 7.7(e). In this case the three lobed structure resembles that of the tilted molecule conformation proposed by Glowatzki. In figure 7.7(f) the BL is recreated using molecules using the black template drawn over figure 7.7(a). The application of the PFP half-width superposition to this image is seen in figure 7.7(g) which recreates the bright central lobe motif observed in the glowatzki data and model, figures 7.7(e) and (d). This simplistic simulation was carried out by creating image 7.7(f) a model of the system based on the data using the template drawn in 7.7(a). The image in figure 7.7(f) is then duplicated and offset by the tip separation before the pixel values of both images are added together to produce the image in figure 7.7(g). The image in figure 7.7(e) is produced via the same process but for a single molecule template.

Inverting the fast and slow scan directions as In 7.8(e) and 7.8(f) results in a tilting behaviour about the short axis. This tilting is uniform across an individual scan but inverting between forward and backward scans which alternates parallel to the short axis. This tilting motif is a scanning artefact stemming from the staggering of the BL molecules. In figure 7.8(e) the tip travels from left to right, as it leaves one row it enters a depression between rows which has the effect of making the first line across a new molecule in the next row appears lower. The same effect can be seen in figure 7.8(a) and 7.8(c) and figures 7.8(b) and 7.8(d) where the appearance of tilt changes based on the fast scan direction of the image.

Within the marked regions of both 7.8(e) and 7.8(f) we see scarring the same height as the BL, suggesting it is a loosely bound PFP molecule diffusing between
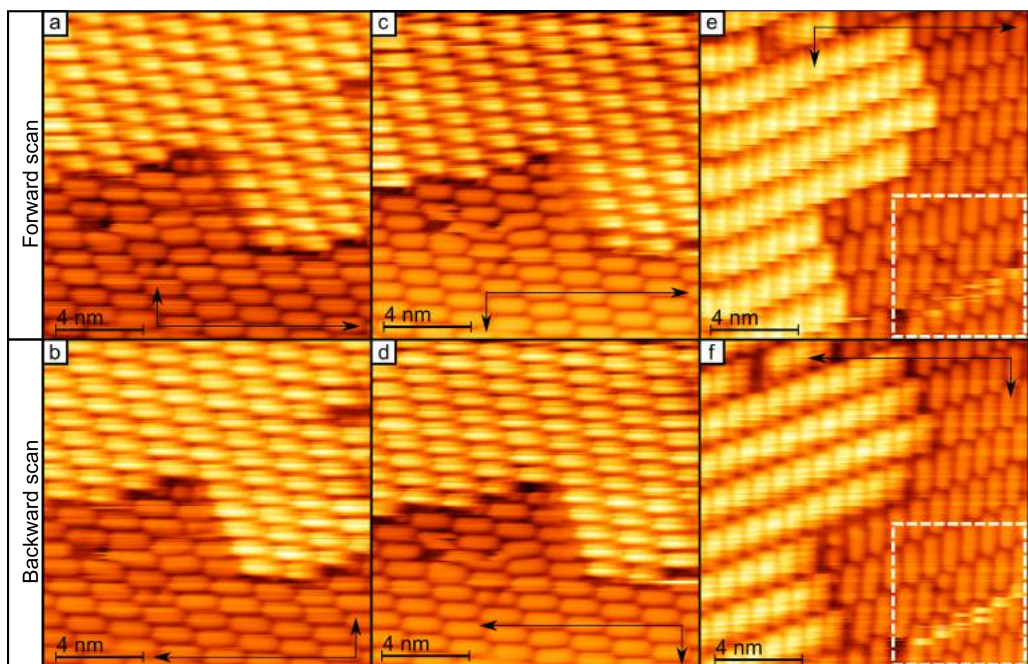
Figure 7.8: The PFP BL and ML resolved simultaneously, the fast and slow scan directions for each image are marked with a long and short arrow respectively. a) Forward up scan, b) backward up scan, c) forward down scan, d) backward down scan, e) forward down scan 90° rotated, f) backward down scan 90° rotated.
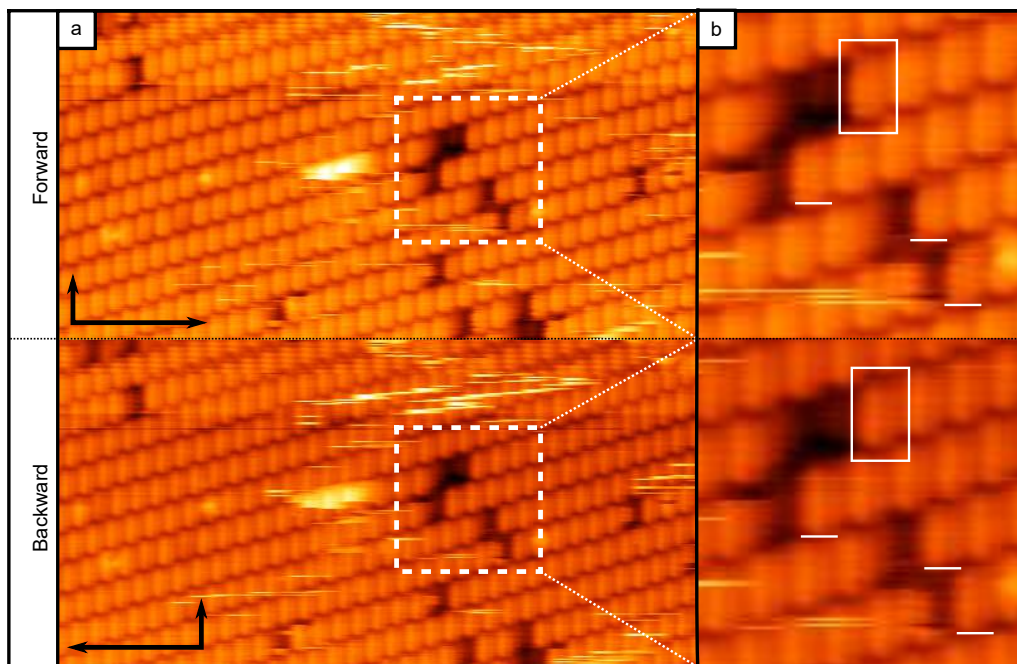
Figure 7.9: A region of the PFP BL($I_T = 100$pA, $V_B = -2.5$V), the fast and slow scan directions for each image are marked with a long and short arrow respectively.a)Consistent BL tilt imaged in both forward and back scans. b) Close up of the defected regions in (a), molecules with a defect neighboring their normally raised edge appear flat flying in the forward scan but tilted in the backward scan.

adsorption sites in response to interacting with the tip. We see that the bands relating to this molecule are centered atop gaps in the monolayer consistent to the out of phase ordering observed for the BL island.

Across all scans taken of this system we see a singular instance of molecules with raised edges that are independent of scan direction. This is presented for reference in figure 7.9.

8

Al$_4$(Cr,Fe)

8.1 Abstract

In this work we prepare the Al$_4$(Cr,Fe)(100) surface to conduct a new real space study in the light of refined structural models. We present the highest resolution STM data to date with accompanying LEED. Our results support the more recent bulk studies and confirm that the symmetry conflicting features, necessitating a larger unit cell in the b parameter, are manifested at the surface termination.

8.2 Introduction

Al$_4$(Cr,Fe) is a decagonal, quasicrystal approximant that possesses a large unit cell [21]. Al$_4$(Cr,Fe)(100) is of interest as a complex metallic alloy, (CMA) as it possesses short range 3 fold symmetry arising from icosahedral clusters which is contrasted against its large, 2 fold unit cell. It has periodic structures at molecular length scales making it suitable for patterning adsorbed molecules structures with greater independence to molecule–molecule interactions. The 3 fold symmetry of atomic clusters at the surface are themselves compatible with the symmetry of PAHs. Truncated

icosahedral clusters of this form have also been effective adsorption sites in patterning molecular quasicrystals using C_{60} [52]. The structure of this CMA (in the orthorhombic phase with composition $Al_{80.6}$ $Cr_{10.7}$ $Fe_{8.7}$) has been studied via x-ray diffraction (XRD) and the findings verified in subsequent surface studies utilising LEED and STM [21]. It should be noted that the ratio between the transition metal (TM) components used in different works varies. From the perspective of atomic sites however Fe and Cr are interchangeable and so variance in the Cr:Fe ratio should not significantly alter the surface structure. The results of the XRD study revealed an orthorombic unit cell with 306 atoms present across 6 layers in the (100) plane [20]. The layers are a mixture of flat lying (f and F) or puckered (p and P) atoms, the puckered layers sites having a small variance in x values. The first three of these layers are mirrored about the central, so that they share inversion symmetry with the last 3. Inverted layers are marked as f' p' and P' as appropriate as seen in figure 8.6(b). Icosahedral and pseudo-icosahedral clusters are present in the system; the later arising from split / partial atomic sites where not all sites can be occupied, common for aluminium / transition metal alloys [20]. The proximity of these clusters introduces some degeneracy in the structure where all sites cannot be occupied simultaneously [20]. STM studies of the (100) surface, presented in figure 8.1, identify the presence of 2 preferred terminations in the (100) plane via the half unit cell terrace heights, as a result of the equivalent but mirrored structure in the layers [22, 21], these are the f and f' layers.

This result arose through identifying Al surface features based on oxidation behaviour and mapping those to structures in the bulk [22]. Since these results, improvements to the structural model have been made, both the original Deng model [20] and the new Bauer-Gaspari [23, 24] model are displayed in figure 8.2. XRD and neutron observations reported by Bauer *et al.* result in symmetry breaking that requires the doubling of the unit cell parameter in the b direction [176, 23].
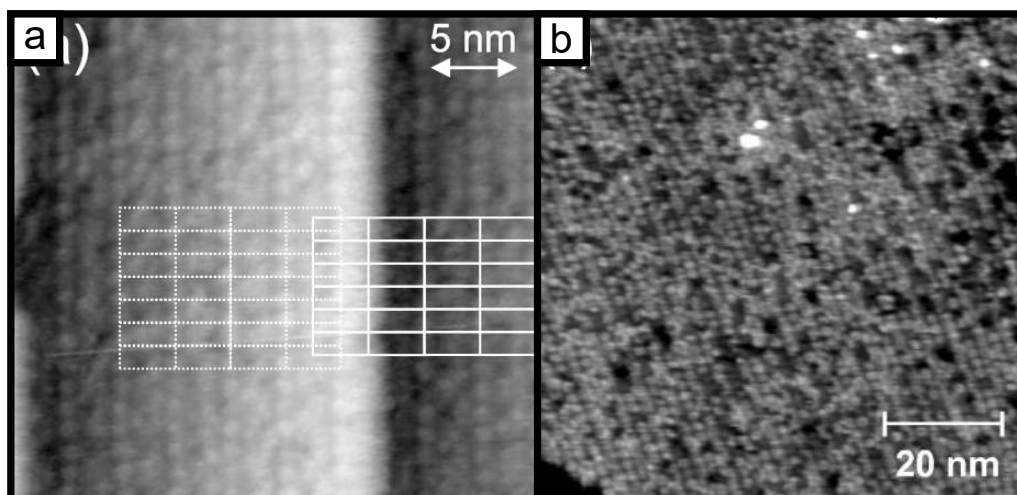
Figure 8.1: a)STM of the prefered termination with the Deng unit cell overlaid [20], reproduced from [21]. b) Oxidation study showing the bright "Al ring" features at the surface, reproduced from [22].
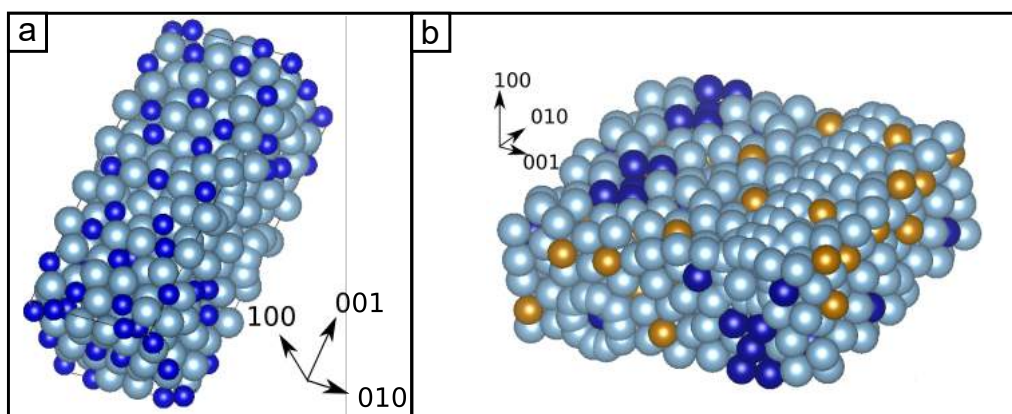
Figure 8.2: a) The Deng model of the $Al_4(Cr,Fe)$ unit cell [20]. b) The improved Bauer-Gaspari $Al_4(Cr,Fe)$ unit cell description [23, 24].

Subsequent work by Gaspari *et al.* confirms this result through high-angle annular dark-field scanning transmission electron microscopy (HAADF) which precisely resolves the TM locations and chemistry [24]. Additional changes from this HAADF study are the determination of the occupancy ratios of the TM sites [23, 24].

8.3   Experimental procedure

STM suitable topography on the (100) surface was obtained as follows: the sample underwent mechanical polishing using 6 μm, 1 μm and 0.25 μm diamond paste prior to cleaning and insertion into the vacuum chamber. Further surface preparation took the form of 45 minutes of Ar ion sputtering at 500 eV followed by 5 hours annealing to 650°C. This was repeated to a total of 40 hours annealing. From the prepared surface a discrete LEED pattern was obtained indicating a high degree of order, after which scanning tunnelling microscopy was performed.

8.4   Results

8.4.1   LEED of Al$_4$(Cr,Fe)(100)

Low energy electron diffraction of the system is used to ensure the surface has undergone sufficient annealing. The diffraction pattern in figure 8.3 reveals the characteristic 6 fold symmetry of small surface features. Additionally we can see the overall 2 fold symmetry of the surface as a whole. Marked in yellow on this image is the rectangular unit cell corresponding to the (100) face of the Deng model [20]. The red unit cell noted along side relates to the expanded unit cell reported by Bauer. This result is significant in showing that the expanded unit cell of the bulk structure is evident at the preferred surface termination, having only been observed by techniques that probe the bulk prior to this.
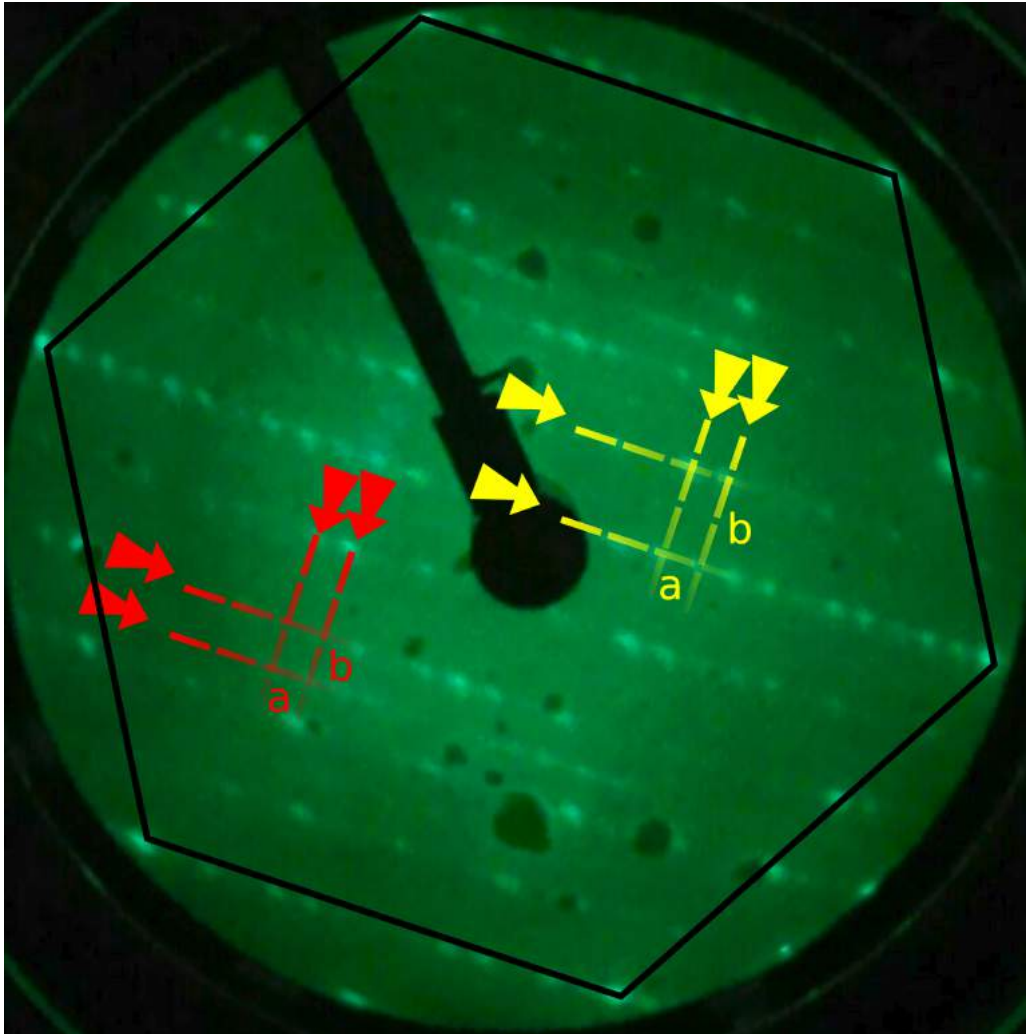
Figure 8.3: 56eV LEED pattern of the $Al_4(Cr,Fe)(100)$ surface. Marked in yellow is the unit cell corresponding to the Deng model [20], the red unit cell corresponds to the expanded model reported by Bauer [23] et. al.
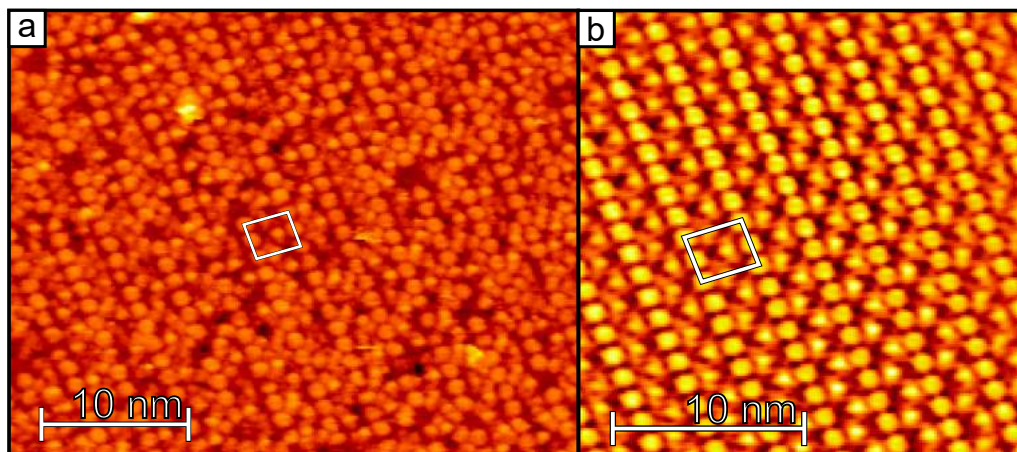
Figure 8.4: High resolution STM of the Al$_4$(Cr,Fe) surface, FFT filtering has been used to manually highlight the bright Al features. The Bauer-Gaspari unit cell model is overlain [24]

8.4.2 High resolution STM of Al$_4$(Cr,Fe)(100)

In this section we present the highest resolution STM data reported for this surface, augmenting that previously reported by Smerdon *et al.* and Parle *et al.* [21, 22] and supporting structural refinements from bulk diffraction measurements. In figure 8.4(a) the surface is shown with the characteristic bright Al chain features previously observed prominently in the work of Parle *et al.* [22]. Similar to this work, we see many vacancies and defects at the surface. This is a difficult problem to overcome during surface preparation. Al as a lighter metal is preferentially removed from the surface during sputter cycles and so is assumed to form the majority of defects observed. Long anneal times are required to repair the surface but also increases the oxidation rate, to which Al is already very susceptible. Using 2D FFT filters we can denoise the data to obtain a clearer image of the periodic features at the surface. This is presented in figure 8.4(b).

In the filtered data surface features are evident that are consistent with the expanded b parameter of the , the unit cell of which is overlaid. These structures mimic the zig-zag occupancy motif reported in the STEM results of Gaspari *et al.* (figure 8.5(a)) and breaks the symmetry of the Deng model used as a reference point
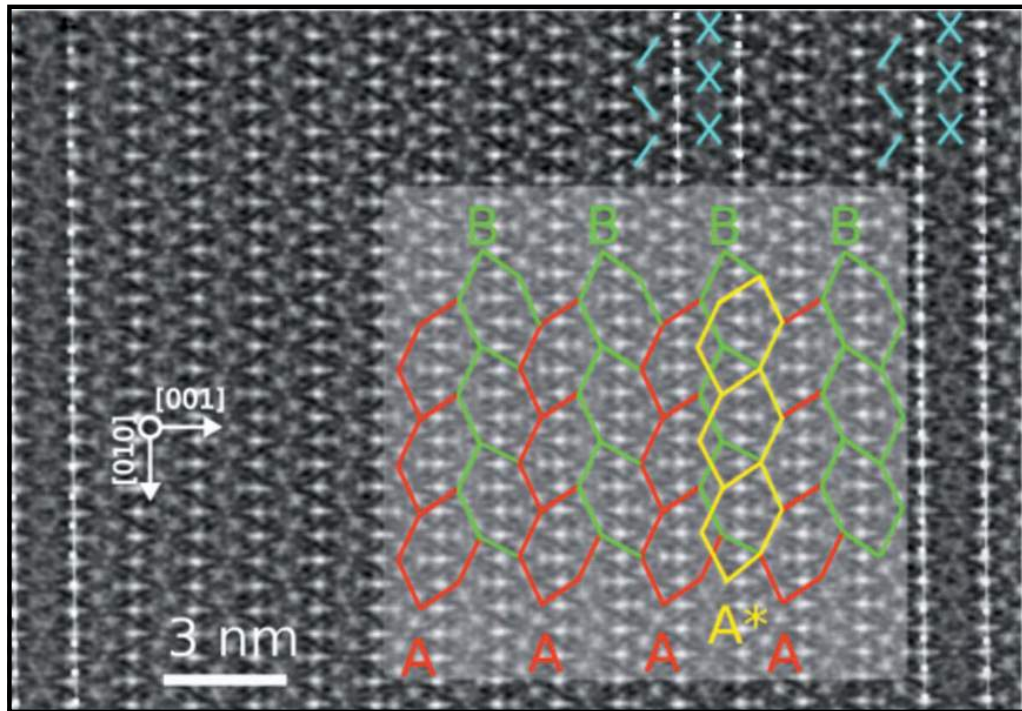
Figure 8.5: a)The noise filtered STEM data presented by gaspari *et al.* illustrating the zig–zag TM motif [24]. The zig–zag structure appears as crosses in some columns relating to the out of phase alignment of unit cells within some layers in the 100 axis.

in previous STM studies of this system.

Identifying surface features

Parle *et al.* [22] define the bright chain features on the $Al_4(Cr,Fe)$ surface as relating to the Al ring features in the f layer of the Deng model, shown in figure 8.2. The high resolution data presented in figure 8.4 and figure 8.6 shows surface features having the appearance of discrete clusters. Across the surface we see occasional vacancies at these Al clusters where the top layer of atoms is missing. In the hollows beneath Al clusters we see either a donut or flower motif as seen in figure 8.6(b). There is no consistent spatial relationship between the occurrences of these different motifs and so they appear to be two different stable expressions of the defect. Surfaces of quasicrystals and their approximants are in general stable truncations of the bulk
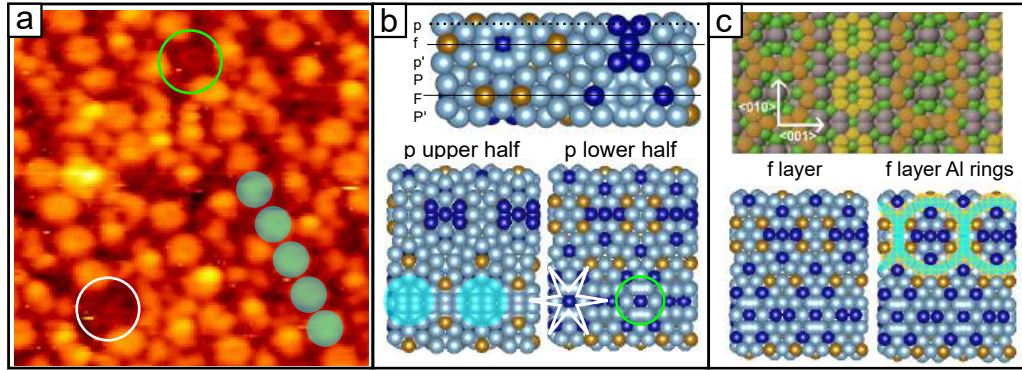
Figure 8.6: a)A close up of surface features and motifs beneath the Al clusters (marked blue) used to identify the termination. The sub surface features evident within AL cluster vacancies are the TM flower and Al donut, marked in white and green respectively. b)The 010 face of the unit cell showing the layer structure. The puckered "p" layer we propose as the preferential termination is marked and a dotted line thesholds atoms within the upper and lower half of the layer. c) The Al rings identified in orange in the Deng model by Parle *et al.* [22] and their position on the F layer of the updated cell.

without significant relaxation or reconstruction [41, 177]. The differing motifs must arise from atomic vacancies only. By inspecting each layer of the Deng model looking for dense Al cluster, sited atop a sublayer that features both a donut and star motif beneath it we find the p layer to be a more plausible surface termination. The puckered p layer forms both components with the Al cluster present in the upper half of the puckered layer and the sublayer flower and donut motifs residing in the lower half as illustrated in figure 8.6(a) and figure 8.6(b).

The flower motif is represented by the TM atoms of the sublayer wheres the donut is the aluminium ring centred within it.

Taking only the atomic sites of the upperlayer of the p layer (for simplicity) and overlaying them on the surface as in figure 8.7(b) we see good correlation between features within the data and the model. Of note is that in contrast to bright regions beneath Al clusters, TM atoms are centred on dark spots. The data is not a true topograph of the surface and is sensitive to the local density of states which will vary with the chemistry and structure of surface features.
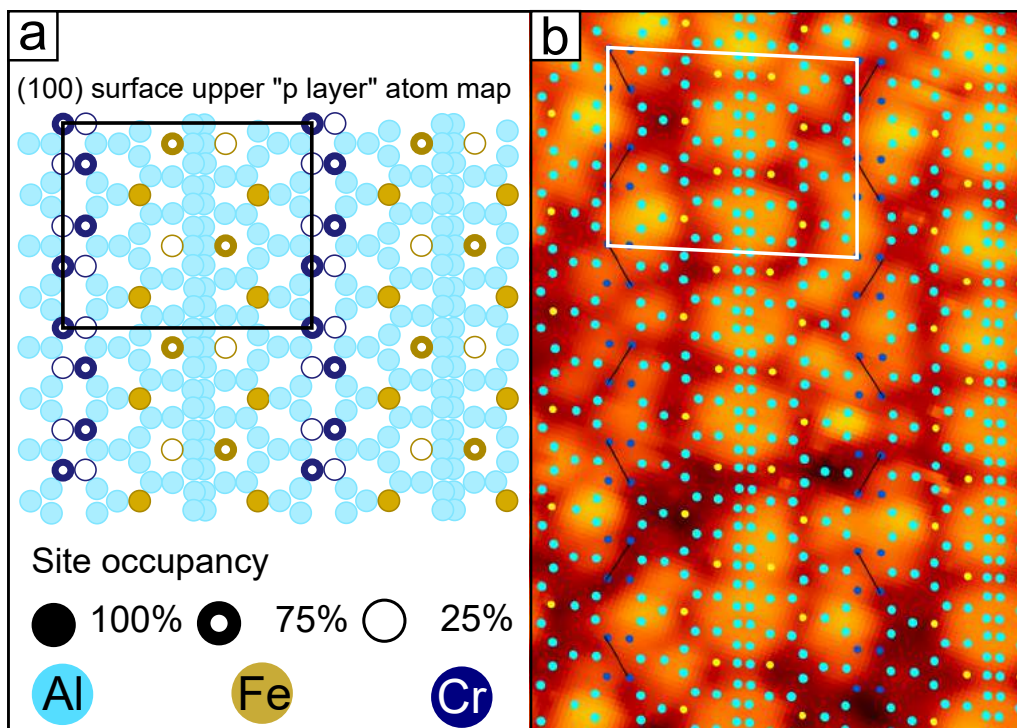
Figure 8.7: a)The p layer occupancies (only the upper half of atoms within this layer are shown for simplicity). b) The partial p layer atomic sites overlaid onto the data. Black lines have been overlaid between Cr atoms sat atop dark spots in the data which mimics the "zig–zag" pattern of the variable occupancies seen in (b).

If we consider the occupancy ratios reported by Gaspari *et al.* [24] for TM atoms as shown in figure 8.7(a), the zig–zag motif of Cr atoms occupancies in the p layer is manifest in the surface data in 8.7(b). The zig–zag Cr structure arising from their occupancy ratios, has been picked out on the surface in figure 8.7(b) by connecting dark (occupied) Cr sites with a black line. Besides TM structures we also see bright spots beneath tri–atomic Al clusters between the Al chains. Al cluster vacancies are common in this region, as a result of Al depletion during sputtering. The location of the tri–atomic Al clusters appears influenced by the TM site occupancy, mimicking the zig–zag motif. This can be seen most clearly in the FFT filtered surface in figure 8.4(b).

Looking across terraces we see the same termination and step edge behaviour that Smerdon *et al.* report, where the a half unit cell step height results in alternating between the p and p' inversion surfaces. The tri–atomic Al cluster and TM site zig–zag motif we have discussed is evident across terraces and we see lateral offsets between these chains as has been reported in the works of Gaspari *et al.* [24]. This is seen in the staggered zig–zags of their STEM results in figure 8.5. The instances of faded and sometimes prominent cross motifs of overlain zig–zags in their data shows coordination of unit cells is weak in the (100) axis of the crystal. At the defected surface we see lateral dislocations of neighbouring zig–zag chains within the same terrace which should otherwise be in phase. In general the zig-zags are seen to be a half unit cell out of of phase at each half-cell terrace step conforming to the alternating p and p' terminations as shown in figure 8.8.

Even with surface defects creating discontinuities in their structure we see zig–zags at the surface remaining consistent over long distances, suggesting a high degree of coordination exists in the (010) axis of the crystal.
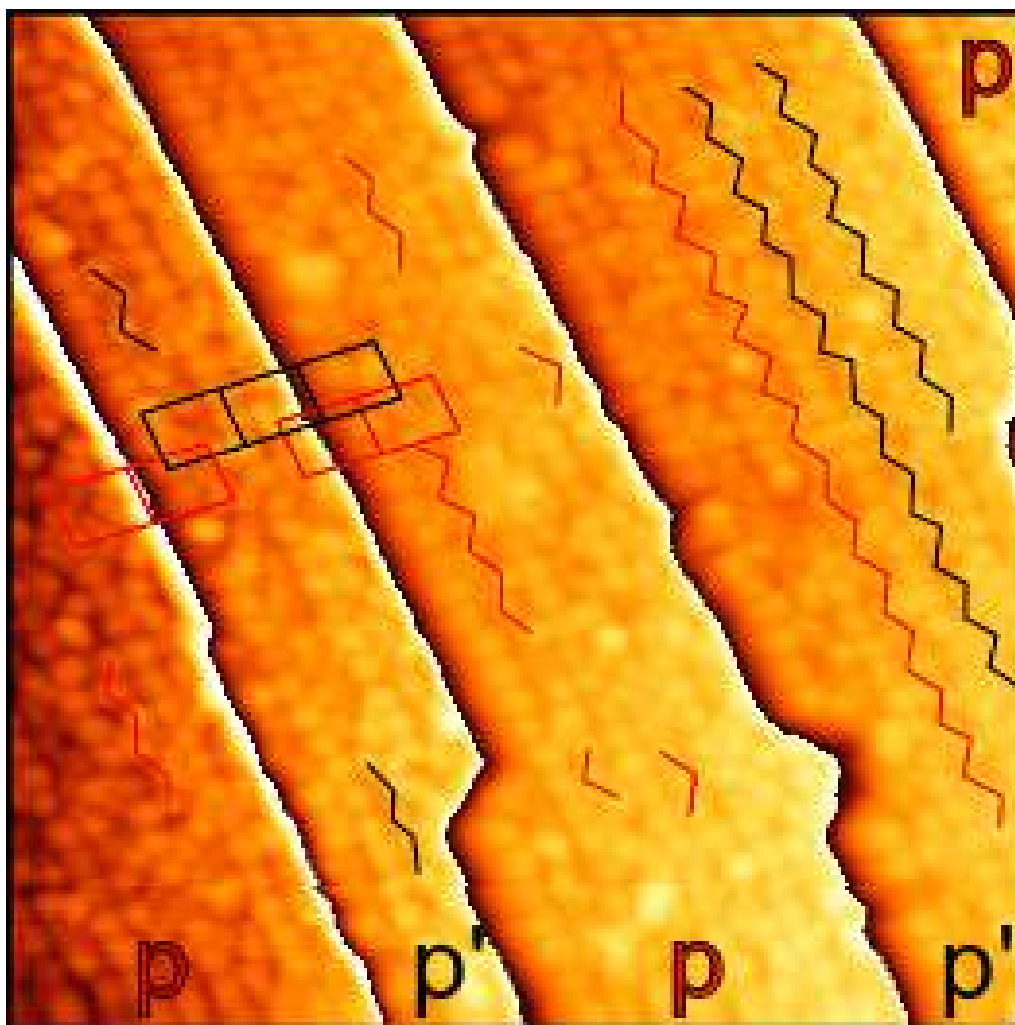
Figure 8.8: Al$_4$(Cr,Fe) terraces. p and p' terraces are marked with partial, colour coded zig–zag motifs relating to the dominant staggering of that terrace.

8.5 Conclusion

Through STM we identify similar zig–zag features seen in the TM sensitive STEM result of Gaspari *et al.* on the Al_4(Cr,Fe) (100) surface. The variable occupancy of TM metals influences the appearance and occupancy of Al clusters on the surface. The suspected partial depletion of Al at the surface in conjunction with the limited occupancy for Al in the model makes the zig-zag pattern of Al clusters seem unlikely to be replicated at a fully populated surface. Instead it is likely an expression of the more favourable sites in the depleted state. This behaviour is of potential interest in templated molecular growth given the reactive nature of Al. Despite the partial depletion of this layer, the Al and TM zigzag motifs are preserved across long distances at the surface. Through inspection of defects and the underlying features in the Al chains across the surface, we relate the surface in our STM data to the updated Bauer-Gaspari model. From this relation we determine that the surface terminates at the puckered p and p' layer which is a departure from the interpretation of Smerdon *et. al.* of the flat f and f' layers. Whilst the flat termination would intuitively seem more favourable energetically. The Al rich nature of the puckered layers is more consistent with the termination behaviour of other Al based CMAs.

9

Further work

"Have you thought of an ending?"

"Yes, several, and all are dark and unpleasant."

"Oh, that won't do! Books ought to have good endings."

– J.R.R. Tolkien, *The Lord of the Rings*

The original motivation to this work was the creation of molecular systems atop symmetry conflicting substrates, with the potential to decompose into graphene with inbuilt ordered defects. The PAH molecules we have considered, are by an extension of this "graphene precursors". Cn has been used to nucleate growth of graphene via thermal decomposition on reactive substrates and DBBA has been extensively used to grow graphene nano-wires on a range of coinage metal surfaces. The work that came closest to this goal was the DBBA study performed on Ag(100) which yielded highly disordered GNRs. Susequently work has been published characterising DBBA derivatives that have successfully produced nano-porous graphene through the interconnection of GNR structures on a range of surfaces including Ag(100) [34]. The following section reiterates the results of each study but in the context of how this advanced us towards this overall goal. Also discussed are the potential avenues for further development.

9.1 Cn/Ag(100)

Cn adsorbs weakly with the substrate and has a low diffusion barrier, exhibiting 2D gas type behaviour. These properties mean that the structure of the Cn monolayer is dependent on Cn coverage and the temperature of ths system. The effect of the Ag(100) symmetry conflict on the structure of the overlayer was very small, the size of the molecules and compressability of the overlayer made *near hexagonal* ordering relatively easy. Domain alignment was the most significant impact of the substrate on the ordering of the overlayer but only at ML coverage. The weak adsorbate-substrate interaction observed for substrates considered in this work makes Cn appear a poor candidate for further study on the impact of surface symmetry and structure in molecular ordering.

9.2 DBBA/Ag(100)

DBBA adsorbs and forms islands on Ag(100) at RT. DBBA is prochiral and domains exhibit enantiomer selectivity within the rows that form. Upon annealing to 470 K we see the DBBA forms disordered clusters at step edges. Only a single anneal temperature was investigated as part of this investigation. Subsequent deposition at 670 K produces disordered GNRs. The parameter space of this system is only sparsely populated. It is possible that lower annealing of the adsorbed system might have demonstrated *in situ* debromination and polymerisation. Similarly having considered only a single anneal temperature means it is impossible to identify the debromination and dehydrogenation temperatures independently.

In our work we see no evidence for debromination of the DBBA that forms islands at RT. The recent works of Moreno *et al.* considering diphenyl-dibromobianthracene, observes debromination and polymerisation occurring at the surface following RT deposition [34]. Some questions left unanswered by our study that could be answered

by characterising the system at an incremental range of temperatures:

- What are the debromination and dehydrogenation temperatures?

- Why does adsorption at 670 K result in GNR formation when lower annealing produces disorder.

An exciting result of the Moreno paper is the production of nano-patterned graphene. They refer to it as nanoporous graphene [178] and this is the first instance that ordered pores have been imparted to the graphene at this scale through "bottom up" synthesis techniques. An emphasis of other systems created in this field is using graphene as a molecular sieve. This work is much more significant as a step to the practical exploitation of the structure dependent electronic properties of graphene. A similarly interesting development highlighted by the bonding between GNRs observed in the Moreno *et al.* work is the growing body of results showing dehydrogenation and bond formation is possible independent of catalysed bonding such as the Ullmann reaction. This has been seen previosuly for DBBA/Cu(111) [125] and mixed systems of where side by side polymerisation of occurs independent of the Br atoms. Other works have shown that a wide range of π functional molecules readily break C–H bonds to form C–Cu–C and C–C bonds on the Cu(110) substrate [179].

With this growing body of evidence the arrangement of DBBA in enantiomer selective staggered rows becomes more interesting. If Br independent dehydrogenation and polymerisation are possible at a lower anneal temperatures then the intra–row staggering observed might result in lattice strain between GNRs joined in the same matter observed for DP-DBBA/Ag(100). Restricting further work to DBBA based systems is needlessly restrictive. With the insight that π functional molecules can polymerise readily, effort can shift from the assembly stage to designing molecules with desirable features, and as self contained devices.

9.3 Al$_4$(Cr,Fe)(100)

A drawback to using fcc single crystals to study symmetry conflicts is that their ordering influence extends only as far as their unit cell unless mediated through an adsorbed larger molecule. CMAS are periodic on the scale of nm and so can directly dictate the symmetry of the overlayer for smaller PAHs. Studying Al$_4$(Cr,Fe)(100) with STM and LEED, both techniques support the most recent expanded structural models. Crucially this work confirms the bulk observed symmetry conflicts are manifest at the surface. Using this new information we also identify the terminating planes of the system, vital for understanding molecular adsorption. A barrier to exploiting this is the high defect rate at the surface observed in our investigation. The preferential depletion of Al atoms from the surface means that neighbouring unit cells are seldom similar. This is a barrier to any study hoping to utilise the extending periodic structure of surface. Prior to adsorption studies, refinement of the surface preparation process to better replenish lost Al would be beneficial.

9.4 PFP/Cu(111)

This chapter represents a departure from other work presented in the thesis. In this we characterised a system through direct observation of molecular orbitals and derived insight into the electronic properties by comparison to similar systems previously reported in the literature. for Pn/Pn/Cu(111) [19] the first Pn layer hybridises with the substrate insulating the bilayer from the effects of the metal creating a Schottky barrier. We see similar behaviour within the PFP bilayer in the appearance of molecules resolved via STM. A natural extension of this work is to directly characterise the PFP/Cu(111) and PFP/PFP/Cu(111) systems through scanning tunnelling spectroscopy to confirm and quantify the rectifying behaviour anticipated for the latter. High rectification ratios have been reported for p-type Schottky diodes

constructed from Pn/C60/Cu(111) [158]. Replication of this work using the n-type PFP merits investigation as does mixed Pn and PFP systems.

List of publications

Dibromobianthryl ordering and polymerization on Ag(100)

S. Smalley, M. Lahti, K. Pussi, V. R. Dhanak, and J. A. Smerdon.

J. Chem. Phys.,146(18):184701, 2017

10

List of presentations

Internal presentations

Molecular Electronics!

JHI CARD talk - 2018

Molecular ordering and self-assembly on the Ag(100) surface.

JHI CARD talk - 2017

Defected graphene through molecular self assembly

JHI CARD talk - 2016

Tailored graphene through molecular self assembly

JHI CARD talk - 2015

Poster presentations

Characterising monolayer and bilayer perfluoropentacene atop Cu(111)

University of birmingham, surface science day 2018

Scanning tunnelling microscopy study of the adsorption and polymerisation of di-bromobianthryl towards graphene nanoribbons on the Ag(100) surface

University of Liverpool, Nano energy July 2016

DBBA adsorption on an aperiodic Cu film atop the five-fold surface of icosahedral AlPdMn

University of Cambridge Summer school 2016

High resolution Scanning Tunnelling Microscopy data of the (100) $Al_4(Cr,Fe)$ surface.

C-MAC days, SIMAP grenoble 2015

Bibliography

[1] Novak, S.; Parker, C.; Becher, D.; Liu, M.; Agostinelli, M.; Chahal, M.; Packan, P.; Nayak, P.; Ramey, S.; Natarajan, S. In *2015 IEEE International Reliability Physics Symposium*, pages 2F.2.1–2F.2.5, 2015.

[2] Oura, K.; Lifshits, V.; Saranin, A.; Zotov, A.; Katayama, M. *Surface science: an introduction;* Springer Science & Business Media, 2013.

[3] Attard, G.; Barnes, C. *Surfaces;* Oxford University Press, 1998.

[4] Martinez, C.; Iverson, B. *Chem. Sci.* **2012**, *3*(7), 2191–2201.

[5] Barlow, S.; Raval, R. *Surf. Sci. Rep.* **2003**, *50*(6), 201–341.

[6] Raval, R. *Chem. Soc. Rev.* **2009**, *38*(3), 707–721.

[7] Grigorescu, A.; Hagen, C. *Nanotechnology* **2009**, *20*(29), 292001.

[8] Cumming, D.; Thoms, S.; Weaver, J.; Beaumont, S. *Microelectron. Eng.* **1996**, *30*(1-4), 423–425.

[9] Cai, J.; Ruffieux, P.; Jaafar, R.; Bieri, M.; Braun, T.; Blankenburg, S.; Muoth, M.; Seitsonen, A.; Saleh, M.; Feng, X.; Müllen, K.; Fasel, R. *Nature* **2010**, *466*(7305), 470–473.

[10] Chen, C. J. *Introduction to scanning tunneling microscopy*, Vol. 4; Oxford University Press on Demand, 1993.

[11] Hamers, R. *Annu. Rev. Phys. Chem.* **1989**, *40*(1), 531–559.

[12] Marshall, M. S.; Castell, M. R. *Chem. Soc. Rev.* **2014**, *43*(7), 2226–2239.

[13] Shi, D.; Ji, W.; Yang, B.; Cun, H.; Du, S.; Chi, L.; Fuchs, H.; Hofer, W. A.; Gao, H.-J. *J. Phys. Chem. C* **2009**, *113*(41), 17643–17647.

[14] Huempfner, T.; Sojka, F.; Forker, R.; Fritz, T. *Surf. Sci.* **2015**, *639*, 80–88.

[15] Simonov, K.; Vinogradov, N.; Vinogradov, A.; Generalov, A.; Zagrebina, E.; Maårtensson, N.; Cafolla, A.; Carpy, T.; Cunniffe, J.; Preobrajenski, A. *J. Phys. Chem. C* **2014**, *118*(23), 12532–12540.

[16] Massimi, L.; Ourdjini, O.; Lafferentz, L.; Koch, M.; Grill, L.; Cavaliere, E.; Gavioli, L.; Cardoso, C.; Prezzi, D.; Molinari, E.; others. *J. Phys. Chem. C* **2015**, *119*(5), 2427–2437.

[17] Glowatzki, H.; Heimel, G.; Vollmer, A.; Wong, S.; Huang, H.; Chen, W.; Wee, A.; Rabe, J.; Koch, N. *J. Phys. Chem. C* **2012**, *116*(14), 7726–7734.

[18] Chen, H.; Chao, I. *Chem. Phys. Lett.* **2005**, *401*(4-6), 539–545.

[19] Smerdon, J. A.; Bode, M.; Guisinger, N.; Guest, J. *Phys. Rev. B: Condens. Matter* **2011**, *84*(16), 165436.

[20] Deng, D.; Mo, Z.; Kuo, K. *J. Phys. Condens. Matter* **2004**, *16*(13), 2283.

[21] Smerdon, J. A.; Parle, J.; McGrath, R.; Bauer, B.; Gille, P. jan **2009**, *224*(1-2), 13–15.

[22] Parle, J.; Beni, A.; Dhanak, V.; Smerdon, J. A.; Schmutz, P.; Wardé, M.; Barthés-Labrousse, M.-G.; Bauer, B.; Gille, P.; Sharma, H.; others. *Appl Surf Sci* **2013**, *283*, 276–282.

[23] Bauer, B.; Pedersen, B.; Frey, F. In *Aperiodic Crystals*; Schmid, S., Withers, R. L., Lifshitz, R., Eds.; Springer Netherlands: Dordrecht, 2013; pages 163–170.

[24] Gaspari, R.; Erni, R.; Arroyo, Y.; Parlinska-Wojtan, M.; Dshemuchadse, J.; Pignedoli, C. A.; Passerone, D.; Schmutz, P.; Beni, A. *J. Appl. Crystallogr.* **2014**, *47*(3), 1026–1031.

[25] Moore, G. *IEEE Solid-State Circuits Society Newsletter* **2006**, *11*(3), 33–35.

[26] Simonite, T. *MIT Technology Review* **2016**.

[27] Waldrop, M. *Nature News* **2016**, *530*(7589), 144.

[28] Novoselov, K.; Geim, A.; Morozov, S. *science* **2004**, *22*, 2–6.

[29] Vozmediano, M. *Phys. Rev. B* **2005**, *72*(15), 1–4.

[30] Han, M. Y.; Özyilmaz, B.; Zhang, Y.; Kim, P. *Phys. Rev. Lett.* **2007**, *98*(20), 206805.

[31] Vancsó, P.; Márk, G.; Lambin, P.; Mayer, A.; Kim, Y.; Hwang, C.; Biró, L. *Carbon* **2013**, *64*, 101–110.

[32] Beiser, A. *Concepts of modern physics;* Tata McGraw-Hill Education, 2003.

[33] Huang, H.; Wei, D.; Sun, J.; Wong, S.; Feng, Y.; Neto, A.; Wee, A. *Sci. Rep.* **2012**, *2*, 983.

[34] Moreno, C.; Panighel, M.; Vilas-Varela, M.; Sauthier, G.; Tenorio, M.; Ceballos, G.; Pena, D.; Mugarza, A. *Chem. Mater.* **2018**, *31*(2), 331–341.

[35] Derenskyi, V.; Gomulya, W.; Talsma, W.; Salazar-Rios, J. M.; Fritsch, M.; Nirmalraj, P.; Riel, H.; Allard, S.; Scherf, U.; Loi, M. A. *Adv. Mater.* **2017**, *29*(23), 1606757.

[36] Sirringhaus, H. *Adv. Mater.* **2014**, *26*(9), 1319–1335.

[37] Tseng, H.-R.; Phan, H.; Luo, C.; Wang, M.; Perez, L. A.; Patel, S. N.; Ying, L.; Kramer, E. J.; Nguyen, T.-Q.; Bazan, G. C.; others. *Adv. Mater.* **2014**, *26*(19), 2993–2998.

[38] Lakshminarayana, A. N.; Ong, A.; Chi, C. *J. Mater. Chem. C* **2018**, *6*(14), 3551–3563.

[39] Kim, C.; Hlaing, H.; Payne, M.; Parkin, S.; Anthony, J.; Kymissis, I. *Chem. Phys. Chem.* **2015**, *16*(6), 1251–1257.

[40] International Union of Crystallography. *Acta Crystallogr. A* **1992**, *48*, 922–946.

[41] Thiel, P. A. *Prog. Surf. Sci.* **2004**, *3*(75), 69–86.

[42] Senechal, M. *Quasicrystals and Geometry;* Cambridge University Press, 1996.

[43] Hofmann, P. *Solid state physics: an introduction;* John Wiley & Sons, 2015.

[44] Kittel, C.; McEuen, P. *Introduction to solid state physics*, Vol. 8; Wiley New York, 1996.

[45] Kettle, S. *Symmetry and structure: readable group theory for chemists;* John Wiley & Sons, 2008.

[46] Wiesendanger, R. *Scanning probe microscopy and spectroscopy: methods and applications;* Cambridge university press, 1994.

[47] Heinz, K. *Rep. Prog. Phys.* **1995**, *58*(6), 637.

[48] Lagoute, J.; Kanisawa, K.; Fölsch, S. *Phys. Rev. B: Condens. Matter* **2004**, *70*(24), 245415.

[49] Lu, M.; Wang, R.; Yang, A.; Duhm, S. *J. Phys.: Condens. Matterr* **2016**, *28*(9), 094005.

[50] Thiel, P. *Annu. Rev. Phys. Chem.* **2008**, *59*, 129–152.

[51] Ledieu, J.; Gaudry, É.; Fournée, V. *Sci. Technol. Adv. Mater* **2014**, *15*(3), 034802.

[52] Smerdon, J. A.; Young, K.; Lowe, M.; Hars, S.; Yadav, T.; Hesp, D.; Dhanak, V.; Tsai, A.; Sharma, H.; McGrath, R. *Nano Lett.* **2014**, *14*(3), 1184–1189.

[53] Fournée, V.; Gaudry, É.; Ledieu, J.; De Weerd, M.; Diehl, R. *J. Phys. Condens. Matter* **2016**, *28*(35), 355001.

[54] Ledieu, J.; Gaudry, É.; Fournée, V.; Smerdon, J. A.; Diehl, R. *Z. Kristallogr. Cryst. Mater.* **2017**, *232*(7-9), 629–645.

[55] Vilan, A.; Aswal, D.; Cahen, D. *Chem. Rev.* **2017**, *117*(5), 4248–4286.

[56] Ibach, H. *Physics of surfaces and interfaces;* 2006.

[57] Everett, D. *Pure Appl. Chem.* **1972**, *31*(4), 577–638.

[58] Winter, M. *Chemical bonding;* Oxford University Press, 2016.

[59] Jeziorowski, H.; Knözinger, H.; Meye, W.; Müller, H. D. *J. Chem. Soc. Faraday Trans.* **1973**, *69*, 1744–1758.

[60] Solymar, L.; Walsh, D.; Syms, R. *Electrical properties of materials;* Oxford university press, 2010.

[61] Batsanov, S.; Batsanov, A. *Introduction to structural chemistry;* Springer Science & Business Media, 2012.

[62] Atkins, P. W.; De Paula, J.; Keeler, J. *Atkins' physical chemistry;* Oxford university press, 2018.

[63] Lukas, S.; Vollmer, S.; Witte, G.; Wöll, C. *J. Chem. Phys.* **2001**, *114*(22), 10123–10130.

[64] Richardson, N. In *Surface and Interface Science;* Wiley-VCH Verlag GmbH Co. KGaA, 2016; pages 629–693.

[65] Otero, R.; de Parga, A.; Gallego, J. *Surf. Sci. Rep.* **2017**, *72*(3), 105–145.

[66] Waldmann, T.; Reichert, R.; Hoster, H. *ChemPhysChem* **2010**, *11*(7), 1513–1517.

[67] Sykes, E. C. H.; Mantooth, B. A.; Han, P.; Donhauser, Z.; Weiss, P. *J. Am. Chem. Soc* **2005**, *127*(19), 7255–7260.

[68] Forrest, S. *Nature* **2004**, *428*(6986), 911.

[69] Chung, D. *J. Mater. Sci.* **2002**, *37*(8), 1475–1489.

[70] Sutton, C.; Risko, C.; Bredas, J.-L. *Chem. Mater.* **2015**, *28*(1), 3–16.

[71] Batra, A.; Kladnik, G.; Vázquez, H.; Meisner, J.; Floreano, L.; Nuckolls, C.; Cvetko, D.; Morgante, A.; Venkataraman, L. *Nat. Commun.* **2012**, *3*, 1086.

[72] Neel, A. J.; Hilton, M. J.; Sigman, M. S.; Toste, F. D. *Nature* **2017**, *543*(7647), 637–646.

[73] Grimme, S. *Angew. Chem. Int. Ed.* **2008**, *47*(18), 3430–3434.

[74] Stranick, S.; Kamna, M.; Weiss, P. *Science* **1994**, pages 99–99.

[75] Seidel, C.; Ellerbrake, R.; Gross, L.; Fuchs, H.; Gu, C.; Karl, N. *Phys. Rev. B* **2001**, *64*(195418), 1–10.

[76] Young, K.; Smerdon, J. A.; Sharma, H.; Lahti, M.; Pussi, K.; McGrath, R. *Phys. Rev. B* **2013**, *87*(8), 085407.

[77] Humblot, V.; Raval, R. *Appl Surf Sci* **2005**, *241*(1-2), 150–156.

[78] Lorenzo, M.; Baddeley, C.; Muryn, C.; Raval, R. *Nature* **2000**, *404*(6776), 376.

[79] Smerdon, J. A.; Rankin, R. B.; Greeley, J. P.; Guisinger, N. P.; Guest, J. R. *ACS nano* **2013**, *7*(4), 3086–3094.

[80] Vidal, F.; Delvigne, E.; Stepanow, S.; LN.; Barth, J.; Kern, K. *J. Am. Chem. Soc.* **2005**, *127*(28), 10101–10106.

[81] Metzger, R. M. *Nanoscale* **2018**, *10*(22), 10316–10332.

[82] Aviram, A.; Ratner, M. *Chem. Phys. Lett.* **1974**, *29*(2), 277–283.

[83] Xiang, D.; Wang, X.; Jia, C.; Lee, T.; Guo, X. *Chem. Rev.* **2016**, *116*(7), 4318–4440.

[84] Tang, M.; Bao, Z. *Chem. Mater* **2010**, *23*(3), 446–455.

[85] Anthony, J.; Facchetti, A.; Heeney, M.; Marder, S.; Zhan, X. *Adv. Mater.* **2010**, *22*(34), 3876–3892.

[86] Joachim, C.; Gimzewski, J.; Aviram, A. *Nature* **2000**, *408*(6812), 541.

[87] Sakamoto, Y.; Suzuki, T.; Kobayashi, M.; Gao, Y.; Fukai, Y.; Inoue, Y.; Sato, F.; Tokito, S. *J. Am. Chem. Soc.* **2004**, *126*(26), 8138–8140.

[88] Sakamoto, Y.; Suzuki, T.; Kobayashi, M.; Gao, Y.; Inoue, Y.; Tokito, S. *Mol. Cryst. Liq. Cryst.* **2006**, *444*(1), 225–232.

[89] Gomes, H. L. *Organic Field-Effect Transistors;* CRC Press: Boca Raton, FL, 2016.

[90] Paterson, A.; Singh, S.; Fallon, K.; Hodsden, T.; Han, Y.; Schroeder, B.; Bronstein, H.; Heeney, M.; McCulloch, Iand Anthopoulos, T. *Adv. Mater.* **2018**, page 1801079.

[91] Kumar, B.; Kaushik, B.; Negi, Y. *Polymer Reviews* **2014**, *54*(1), 33–111.

[92] Morigaki, K.; Ogihara, C. In *Springer Handbook of Electronic and Photonic Materials;* Springer, 2017.

[93] Petty, M. C.; Nagase, T.; Suzuki, H.; Naito, H. In *Springer Handbook of Electronic and Photonic Materials*; Kasap, S., Capper, P., Eds.; Springer International Publishing: Cham, 2017; pages 1–1.

[94] Ikawa, M.; Yamada, T.; Matsui, H.; Minemawari, H.; Tsutsumi, J.; Horii, Y.; Chikamatsu, M.; Azumi, R.; Kumai, R.; Hasegawa, T. *Nat. Commun.* **2012**, *3*, 1176.

[95] Dimitrakopoulos, C. D.; Mascaro, D. J. *IBM J. Res. Dev* **2001**, *45*(1), 11–27.

[96] Bryce, M. R.; Petty, M. C. *Nature* **1995**, *374*(6525), 771.

[97] Abe, M.; Mori, T.; Osaka, I.; Sugimoto, K.; Takimiya, K. *Chem. Mater.* **2015**, *27*(14), 5049–5057.

[98] Minemawari, H.; Yamada, T.; Matsui, H.; Tsutsumi, J.; Haas, S.; Chiba, R.; Kumai, R.; Hasegawa, T. *Nature* **2011**, *475*(7356), 364.

[99] Novoselov, K. S.; Fal, V.; Colombo, L.; Gellert, P.; Schwab, M.; Kim, K.; others. *Nature* **2012**, *490*(7419), 192.

[100] Elliott, S. *The Physics and Chemistry of Solids;* John Wiley & Sons, 1998.

[101] Kolasinski, R. D.; Polk, J. E.; Goebel, D.; Johnson, L. K. *J. Vac. Sci. Technol A* **2007**, *25*(2), 236–245.

[102] Creighton, J.; Ho, P. In *Surface engineering series Volume 2: Chemical Vapor Deposition;* ASM International, 1st ed., 2001; chapter 1, pages 1–10.

[103] Hudson, J. *Surface science: an introduction;* Elsevier, 2013.

[104] Kahn, A. *Materials Horizons* **2016**, *3*(1), 7–10.

[105] Tersoff, J.; Hamann, D. R. *Phys. Rev. B* **1985**, *31*(2), 805.

[106] Wolf, E. *Principles of electron tunneling spectroscopy*, Vol. 152; Oxford University Press, 2012.

[107] Tsuneda, T. *Density functional theory in quantum chemistry;* Springer, 2014.

[108] Cohen, A.; Mori-Sánchez, P.; Yang, W. *Science* **2008**, *321*(5890), 792–794.

[109] Jones, R. *Rev. Mod. Phys.* **2015**, *87*(3), 897.

[110] Fiolhais, C.; Nogueira, F.; Marques, M. *A primer in density functional theory*, Vol. 620; Springer Science & Business Media, 2003.

[111] Schmidt, M.; Masson, A.; Bréchignac, C. *International Journal of Mass Spectrometry* **2006**, *252*(2), 173–179.

[112] Wang, B.; Ma, X.; Caffio, M.; Schaub, R.; Li, W. *Nano Lett.* **2011**, *430*(11), 426–430.

[113] Wan, X.; Chen, K.; Liu, Dand Chen, J.; Miao, Q.; Xu, J. *Chem. Mater* **2012**, *24*(20), 3906–3915.

[114] Jarvis, S.; Taylor, S.; Baran, J.; Thompson, D.; Saywell, A.; Mangham, B.; Champness, N.; Larsson, J.; Moriarty, P. *J. Phys. Chem. C* **2015**, *119*(50), 27982–27994.

[115] Mckinnon, A.; Welland, M.; John, S.; BD, W. *Thin Solid Films* **1995**, *257*(94), 63–67.

[116] Sojka, F.; Meissner, M.; Zwick, C.; Forker, R.; Fritz, T. *Rev. Sci. Instrum.* **2013**, *84*(1), 015111.

[117] Leedpat. Hermann, K.; Van Hove, M. **2014**.

[118] Smalley, S.; Lahti, M.; Pussi, K.; Dhanak, V.; Smerdon, J. A. *J. Chem. Phys.* **2017**, *146*(18), 184701.

[119] Li, X.; Cai, W.; An, J.; Kim, S.; Nah, J.; Yang, D.; Piner, R.; Velamakanni, A.; Jung, I.; Tutuc, E.; Banerjee, S.; Colombo, L.; Ruoff, R. *Science* **2009**, *324*(5932), 1312–1314.

[120] Schwierz, F. *Nat. Nanotechnol.* **2010**, *5*(7), 487–496.

[121] Yazyev, O. *Acc. Chem. Res.* **2013**, *46*(10), 2319–2328.

[122] Sarkar, M.; Samanta, A. *Acta Cryst. E* **2003**, *59*(11), o1764–o1765.

[123] Fan, Q.; Gottfried, J.; Zhu, J. *Acc. Chem. Res.* **2015**, *48*(8), 2484–2494.

[124] Kolmer, M.; Ahmad, Z.; Prauzner-Bechcicki, J.; Piskorz, W.; Zasada, F.; Godlewski, S.; Such, B.; Sojka, Z.; Szymonski, M. *Angew. Chem. Int. Ed.* **2013**, *125*(39), 10490–10493.

[125] Sánchez-Sánchez, C.; Dienel, T.; Deniz, O.; Ruffieux, P.; Berger, R.; Feng, X.; Müllen, K.; Fasel, R. *ACS Nano* **2016**, *10*(8), 8006–8011.

[126] Simonov, K.; Vinogradov, N.; Vinogradov, A.; Generalov, A.; Zagrebina, E.; Svirskiy, G.; Cafolla, A.; Carpy, T.; Cunniffe, J.; Taketsugu, T.; Lyalin, A.; Mårtensson, N.; Preobrajenski, A. *ACS Nano* **2015**, *9*(9), 8997–9011.

[127] Huang, P.; Ruiz-Vargas, C.; van der Zande, A.; Whitney, W.; Levendorf, M.; Kevek, J.; Garg, S.; Alden, J.; Hustedt, C.; Zhu, Y.; Park, J.; McEuen, P.; Muller, D. *Nature* **2011**, *469*(7330), 389–392.

[128] Rasool, HIand Song, E.; Mecklenburg, M.; Regan, B.; Wang, K.; Weiller, B. H.; Gimzewski, J. K. *J. Am. Chem. Soc.* **2011**, *133*(32), 12536–12543.

[129] Tsen, A.; Brown, L.; Levendorf, M.; Ghahari, F.; Huang, P.; Havener, R.; Ruiz-Vargas, C.; Muller, D.; Kim, P.; Park, J. *Science* **2012**, *336*(6085), 1143–1146.

[130] Fei, Z.; Rodin, A.; Gannett, W.; Dai, S.; Regan, W.; Wagner, M.; Liu, M.; McLeod, A.; Dominguez, G.; Thiemens, M.; Neto, A.; Keilmann, F.; Zettl, A.; Hillenbrand, R.; MM, F.; Basov, D. *Nat. Nanotechnol.* **2013**, *8*(11), 821–825.

[131] Batzill, M. *Surf. Sci. Rep.* **2012**, *67*(3), 83–115.

[132] Han, P.; Akagi, K.; Canova, F.; Mutoh, H.; Shiraki, S.; Iwaya, K.; Weiss, P.; Asao, N.; Hitosugi, T. *ACS Nano* **2014**, *8*(9), 9181–9187.

[133] Kresse, G.; Hafner, J. *Phys. Rev. B* **1993**, *47*(1), 558.

[134] Kresse, G.; Hafner, J. *J. Phys.: Condens. Matter* **1994**, *6*(40), 8245.

[135] Kresse, G.; Hafner, J. *Phys. Rev. B* **1994**, *49*(20), 14251.

[136] Kresse, G.; Furthmüller, J. *Comput. Mater. Sci.* **1996**, *6*(1), 15–50.

[137] Blöchl, P. E. *Phys. Rev. B* **1994**, *50*(24), 17953.

[138] Perdew, J.; Burke, K.; Ernzerhof, M. *Phys. Rev. Lett.* **1996**, *77*(18), 3865.

[139] Monkhorst, H.; Pack, J. *Phys. Rev. B* **1976**, *13*(12), 5188.

[140] Klimeš, J.; Bowler, D.; Michaelides, A. *Phys. Rev. B* **2011**, *83*(19), 195131.

[141] Cortés, R.; Mascaraque, A.; Schmidt-Weber, P.; Dil, H.; Kampen, T.; Horn, K. *Nano Lett.* **2008**, *8*(12), 4162–4167.

[142] Carpy, T. *A scanning tunnelling microscopy and spectroscopic study of bromine functionalised molecules on metal surfaces* PhD thesis, Dublin City University, **2015**.

[143] Singh, T.; Meghdadi, F.; Günes, S.; Marjanovic, N.; Horowitz, Gand Lang, P.; Bauer, S.; Sariciftci, N. *Adv. Mater.* **2005**, *17*(19), 2315–2320.

[144] Daraktchiev, M.; von Mühlenen, A.; Nüesch, F.; Schaer, M.; Brinkmann, M.; Bussac, M.; Zuppiroli, L. *New J. Phys.* **2005**, *7*(1), 133.

[145] Klauk, H.; Halik, M.; Zschieschang, U.; Schmid, G.; Radlik, W.; Weber, W. *J. Appl. Phys.* **2002**, *92*(9), 5259–5263.

[146] Yan, H.; Kagata, T.; Okuzaki, H. *Appl. Phys. Lett.* **2009**, *94*(2), 14.

[147] Kolata, K.; Breuer, T.; Witte, G.; Chatterjee, S. *ACS nano* **2014**, *8*(7), 7377–7383.

[148] Kawai, S.; Pawlak, R.; Glatzel, T.; Meyer, E. *Phys. Rev. B: Condens. Matter* **2011**, *84*(8), 085429.

[149] Rinn, A.; Breuer, T.; Wiegand, J.; Beck, M.; bner, J.; j, R. C.; Oestreich, M.; Heimbrodt, W.; Witte, G.; Chatterjee, S. *ACS Appl. Mater. Interfaces* **2017**, *9*(48), 42020–42028.

[150] Schwarze, M.; Tress, W.; Beyer, B.; Gao, F.; Scholz, R.; Poelking, C.; Ortstein, K.; Günther, A.; Kasemann, D.; Andrienko, D.; others. *Science* **2016**, *352*(6292), 1446–1449.

[151] Anger, F.; Ossó, J.; Heinemeyer, U.; Broch, K.; Scholz, R.; Gerlach, A.; Schreiber, F. *J. Chem. Phys* **2012**, *136*(5), 054701.

[152] Shen, B.; Geiger, T.; Einholz, R.; Reicherter, F.; Schundelmeier, S.; Maichle-Mössmer, C.; Speiser, B.; Bettinger, H. *J. Org. Chem.* **2018**, *83*(6), 3149–3158.

[153] Toyoda, K.; Hamada, I.; Yanagisawa, S.; Morikawa, Y. *Org. Electron.* **2011**, *12*(2), 295–299.

[154] Götzen, J.; Schwalb, C.; Schmidt, C.; Mette, G.; Marks, M.; Höfer, U.; Witte, G. *Langmuir* **2010**, *27*(3), 993–999.

[155] Eremtchenko, M.; Temirov, R.; Bauer, D.; Schaefer, J.; Tautz, F. *Phys. Rev. B: Condens. Matter* **2005**, *72*(11), 115430.

[156] Soe, W.; Manzano, C.; De Sarkar, A.; Chandrasekhar, N.; Joachim, C. *Phys. Rev. Lett.* **2009**, *102*(17), 176102.

[157] Lo, Y.; Chang, J.; Hoffmann, G.; Su, W.; Wu, C.; Chang, C. *Jpn. J. Appl. Phys.* **2013**, *52*(10R), 101601.

[158] Smerdon, J. A.; Giebink, N.; Guisinger, N.; Darancet, P.; Guest, J. *Nano Lett.* **2016**, *16*(4), 2603–2607.

[159] Hinderhofer, A.; Frank, C.; Hosokai, T.; Resta, A.; Gerlach, A.; Schreiber, F. *J. Chem. Phys.* **2011**, *134*(10), 104702.

[160] Goiri, E.; Matena, M.; El-Sayed, A.; Lobo-Checa, J.; Borghetti, P.; Rogero, C.; Detlefs, B.; Duvernay, J.; Ortega, J.; De Oteyza, D. *Phys. Rev. Lett.* **2014**, *112*(11), 117602.

[161] Salzmann, I.; Moser, A.; Oehzelt, M.; Breuer, T.; Feng, X.; Juang, Z.; Nabok, D.; Della Valle, R.; Duhm, S.; Heimel, G.; others. *ACS nano* **2012**, *6*(12), 10874–10883.

[162] Koch, N.; Gerlach, A.; Duhm, S.; Glowatzki, H.; Heimel, G.; Vollmer, A.; Sakamoto, Y.; Suzuki, T.; Zegenhagen, J.; Rabe, J.; others. *J. Am. Chem. Soc.* **2008**, *130*(23), 7300–7304.

[163] Dougherty, D.; Jin, W.; Cullen, W.; Reutt-Robey, J.; Robey, S. *J. Phys. Chem. C* **2008**, *112*(51), 20334–20339.

[164] Goiri, E.; García-Lastra, J.; Corso, M.; Adb El-Fattah, Z.; Ortega, J.; de Oteyza, D. *J. Phys. Chem. Lett.* **2012**, *3*(7), 848–852.

[165] Franco-Cañellas, A.; Wang, Q.; Broch, K.; Shen, B.; Gerlach, A.; Bettinger, H.; Duhm, S.; Schreiber, F. *Phys. Rev. Mater.* **2018**, *2*(4), 044002.

[166] Inoue, Y.; Sakamoto, Y.; Suzuki, T.; Kobayashi, M.; Gao, Y.; Tokito, S. *Jpn J. Appl. Phys.* **2005**, *44*(6R), 3663.

[167] Ben Jamaa, M.; Mohanram, K.; De Micheli, G. In *Proceedings of the Conference on Design, Automation and Test in Europe*, pages 622–627. European Design and Automation Association, 2009.

[168] Duan, L.; Qiao, J.; Sun, Y.; Qiu, Y. *Adv. Mater.* **2011**, *23*(9), 1137–1144.

[169] Heimel, G.; Duhm, S.; Salzmann, I.; Gerlach, A.; Strozecka, A.; Niederhausen, J.; Bürker, C.; Hosokai, T.; Fernandez-Torrente, I.; Schulze, G.; others. *Nat. Chem.* **2013**, *5*(3), 187.

[170] Tzeng, C.; Tsuei, K.; Cheng, H.; Chu, R. *J. Phys.: Condens. Matter* **2007**, *19*(17), 176009.

[171] Pai, W.; Jeng, H.; Cheng, C.; Lin, C.; Xiao, X.; Zhao, A.; Zhang, X.; Xu, G.; Shi, X.; Van Hove, M.; others. *Phys. Rev. Lett.* **2010**, *104*(3), 036103.

[172] Wang, L.; Cheng, H. *Phys. Rev. B: Condens. Matter* **2004**, *69*(4), 045404.

[173] Chiutu, C.; Sweetman, A.; Lakin, A.; Stannard, A.; Jarvis, S.; Kantorovich, L.; Dunn, J.; Moriarty, P. *Phys. Rev. Lett.* **2012**, *108*(26), 268302.

[174] Lakin, A.; Chiutu, C.; Sweetman, A.; Moriarty, P.; Dunn, J. *Phys. Rev. B: Condens. Matter* **2013**, *88*(3), 035447.

[175] Pai, W.; Hsu, C.; Lin, M.; Lin, K.; Tang, T. *Phys. Rev. B: Condens. Matter* **2004**, *69*(12), 125405.

[176] Bauer, B.; Pedersen, B.; Gille, P. *Z. Kristallogr.* **2009**, *224*(1-2), 109–111.

[177] McGrath, R.; Leung, L.; Barrett, S.; Ledieu, J. In *Proceedings of the Royal Microscopical Society*, Vol. 40, pages 215–220. London: Royal Microscopical Society,[1966]-c2004., 2005.

[178] Moreno, C.; Vilas-Varela, M.; Kretz, B.; Garcia-Lekue, A.; Costache, M.; Paradinas, M.; Panighel, M.; Ceballos, G.; Valenzuela, S.; Peña, D.; others. *Science* **2018**, *360*(6385), 199–203.

[179] Haq, S.; Hanke, Fand Sharp, J. P. M.; Amabilino, D.; Raval, R. *ACS nano* **2014**, *8*(9), 8856–8870.